Measuring waves in difficult places: New approaches to observing waves in hurricanes and sea ice

Jacob Davis

A dissertation
submitted in partial fulfillment of the
requirements for the degree of

Doctor of Philosophy

University of Washington

2025

Reading Committee:
Jim Thomson, Chair
Isabel Houghton
Madison Smith

Program Authorized to Offer Degree:
Civil & Environmental Engineering

University of Washington

Abstract

Measuring waves in difficult places: New approaches to observing waves in hurricanes and sea ice

Jacob Davis

Chair of the Supervisory Committee:
Jim Thomson
Civil & Environmental Engineering

New approaches are applied to study ocean surface wave dynamics in hurricanes and the coastal Arctic. In hurricanes, arrays of drifting buoys and airborne radar are used to characterize the wind speed dependence and spatial distribution of ocean surface roughness caused by waves. Hurricane-generated waves, and the drag imparted by their roughness, contribute to coastal flooding, cause infrastructure damage, and modify exchanges of momentum and heat between the atmosphere and ocean—important controls on storm intensification offshore. In the coastal Arctic, a novel method called Distributed Acoustic Sensing is combined with machine learning to measure waves from a submarine fiber-optic cable offshore of Oliktok Point, Alaska. This system can be used for the subsequent study of wave-ice interactions and to monitor wave action in regions susceptible to coastal change. Both approaches leverage innovative, low-cost sensing modalities to measure waves in hard-to-reach environments with exceptional spatial resolution. These measurements enhance our ability to understand, monitor, and predict the impacts of the ocean on coastlines.

Drifting buoy observations in hurricanes Ian (2022) and Fiona (2022) are merged with modeled surface wind speeds to determine the evolution of wave slope at high wind speeds. Wave slope is quantified using the mean square slope, which is commonly used as proxy for ocean surface roughness. At low-to-moderate wind speeds (≤ 15 m s^{-1}), slopes increase linearly with wind speed. At higher winds (> 15 m s^{-1}), slopes continue to increase, but at a reduced rate. At extreme winds (> 30 m s^{-1}), slopes asymptote. The mean square slopes are directly related to the wave spectral shapes, which over the resolved frequency range (0.03 to 0.5 Hz) are characterized by an equilibrium tail (f^{-4}) at moderate winds and a saturation tail (f^{-5}) at higher winds. The asymptotic behavior of wave slope as a function of wind speed could contribute to the reduction of surface drag at high wind speeds.

An airborne radar is then combined with the drifting wave buoys to provide a multiscale view of hurricane-generated waves. Wave slopes measured by the radar, which include waves 0.2 m and longer, saturate in a similar manner to the buoy-measured slopes. A method to infer the shape of the spectral tail from 0.5 Hz to 3 Hz using colocated mean square slope observations from each instrument is introduced. The method is able to recover the frequency f^{-5} tail characteristic of the saturation range expected at these frequencies based on theory.

Next, a dense array of buoy observations in Hurricane Idalia (2023) is used to investigate the spatial distribution and dependence of mean square slope on wind, wave, and storm characteristics. Inside Hurricane Idalia, buoy-measured mean square slopes have a secondary dependence on wind-wave alignment: at a given wind speed, slopes are higher where wind and waves are aligned compared to where wind and waves are crossing. At moderate wind speeds, differences in mean square slope between aligned and crossing conditions can vary 15% to 20% relative to their mean. These changes in wave slope may be related to the reported dependence of air-sea drag coefficient on wind-wave alignment.

Lastly, in the coastal Arctic, two new data-driven models for estimating ocean surface waves from distributed acoustic sensing (DAS) submarine cable strain rate are developed using supervised machine learning. The new models are trained on target data from pressure moorings at three sites along 27.1 km of cable and are benchmarked against an empirical transfer function method previously used to estimate waves from DAS. A model which uses convolutional neural networks to transform frequency-wavenumber spectra to pressure spectra outperforms

the benchmark in wave height and period prediction when evaluated on the cable at Oliktok Point. Regression-based machine learning is useful for estimating waves from DAS data when the pressure-strain relationship varies temporally and spatially across different wave conditions.

TABLE OF CONTENTS

LIST OF FIGURES

ACKNOWLEDGMENTS

My advisor, Jim Thomson, has been an outstanding role model both in work and in life. From day one, I have admired his profound integrity and dedication to his craft. Often, I find myself asking, "What would Jim do?" Thank you, Jim, for providing me with endless opportunities to grow as a scientist. I look forward to being your colleague.

Committee members Maddie Smith, Isabel Houghton, Christie Hegermiller, and Andrea Ogston have provided thoughtful feedback and guidance over the past two years. I thank my coauthors for their input and careful review of first drafts, revised drafts, and final submissions. I've had the distinct pleasure of working with Chris Fairall. Among the wealth of knowledge Chris has shared is the timeless reminder of just how far a pencil, paper, and an afternoon can get you.

My doctoral work was generously supported by the National Science Foundation Graduate Research Fellowship Program (Grant No. DGE-2140004) and by the Link Ocean Engineering and Instrumentation Ph.D. Fellowship Program. I thank the Office of Naval Research and the U.S. National Ocean Partnership Program for supporting our work on the NOPP Hurricane Coastal Impacts project (Grant No. N00014-21- 1-2194).

The NHCI project and its members were central to my apprenticeship, and I thank them for demonstrating what an exceptional project looks like. Our success would not have been possible without support from the command and crew of the Naval Research Laboratory's Scientific Deployment Squadron (VXS-1). I'll look back fondly on our long, sweaty plane rides together.

Alex de Klerk, Fiona Drum, Phil Bush, and Brenton Salmi tirelessly engineered, prepared, and tested microSWIFTs. I am grateful to Sofar Ocean for their generous data sharing policy, and for the many Spotters they've let me toss out of aircraft (including those that broke). Distributed Acoustic Sensing data collection was made possible by collaborations with Robert E. Abbott, Christian Stanciu, and Michael G. Baker of Sandia National Laboratories, and with Quintillion.

My research career may never have happened without UMass Amherst professors Stephen Nonnenmann and Krish Thiagarajan Sharman, who each welcomed me into their groups with open arms. Krish taught me the beauty of wave mathematics and fluid mechanics, forever shaping my academic journey. My mentees Luis, Emily, and Miguel have given me the opportunity to pay it forward. They remind me of the sheer joy of curiosity and the excitement of science.

I take great pride in being a member of the UW Environmental Fluid Mechanics family. I've enjoyed our engaging Thursday seminars, followed by sunny cookouts and happy hours. I look forward to presenting as a guest speaker myself someday in the future.

My dear friend and office mate, EJ Rainville, has accompanied me on my Ph.D. journey from the start. His good nature and humor have helped me through the darkest days of Washington winter and the deepest depths of graduate school. I'll cherish our countless hours at the whiteboard, meandering discussions, and trips to conferences abroad (I wonder what excuse we'll find to get us back to France next year?).

To my friends in Seattle, back East, and beyond: I value your friendship beyond measure. Thank you for many years of laughter, good food, and adventure. Anna Doak and the Bass Church family have been an anchor for me throughout graduate school. The times I've spent with them during lessons, group jams, and cabin retreats are among the most meaningful experiences I've had during my lifelong pursuit of music.

I can't thank my family enough for supporting me through countless years of education, even as my pursuit of knowledge has taken me thousands of miles across the country. You've instilled in me qualities of hard work, a "DIY" spirit, and the confidence to take on new challenges—many of the same virtues needed to endure a Ph.D. program and succeed in a career in science. To my partner, Jackie: I'm endlessly grateful for your kind-heartedness and your celebration of even the smallest wins. Thank you for uprooting your life in Cambridge to live here in Seattle with me. We've led such a rich life here, and I'm so excited for the adventures that lie ahead.

Chapter 1

INTRODUCTION

1.1 Overview

Waves drive many important processes at the ocean surface. In hurricanes, waves mediate the exchange of momentum and enthalpy between the atmosphere and ocean, thereby influencing storm intensity. At the poles, waves affect the evolution and movement of sea ice, while also catalyzing coastal change in regions that are highly susceptible to erosion. In both environments, waves introduce complex dynamics and strong spatial gradients. The observations needed to capture these dynamics demand innovative methods and collaborative approaches.

Arrays of low-cost, free-drifting wave buoys and an airborne radar system are used to characterize waves beneath hurricanes. The observations provide insight into the evolution and spatial distribution of ocean surface roughness caused by the waves. In the coastal Arctic, a novel method called Distributed Acoustic Sensing is combined with machine learning to estimate waves from a submarine fiber-optic cable primarily used for telecommunications. The calibrated cable can be used for the subsequent monitoring of coastal wave action and to study interactions between waves and sea ice. One unifying theme is the use of innovative methods to measure ocean waves in challenging environments. Another theme is wave measurement at many locations simultaneously, which improves spatial resolution compared to classic methods which only measure waves at a single position.

1.2 Outline

Chapter 1 provides background on relevant research questions which motivate the study of waves in hurricanes and in the Arctic. New approaches to help tackle these challenges are introduced.

In Chapter 2, drifting wave buoy observations from Hurricanes Ian (2022) and Fiona (2022) are combined with modeled wind speeds to characterize the dependence of wave slope, as quantified by the *mean square slope*, on wind speed up to 54 m s^{-1}. This chapter builds on the pioneering work of Cox and Munk (1954) and efforts that have followed. It is reproduced from:

> Davis, J. R., Thomson, J., Houghton, I. A., Doyle, J. D., Komaromi, W. A., Fairall, C. W., Thompson, E. J., and Moskaitis, J. R. Saturation of Ocean Surface Wave Slopes Observed During Hurricanes. *Geophysical Research Letters*, 50(16), August 2023b. doi: 10.1029/2023GL104139.

In Chapter 3, airborne radar observations in six hurricanes are used to characterize the mean square slope of shorter waves at high wind speeds (waves with wavelengths on the order of tens of centimeters, as compared to waves several meters and longer measured by buoys). Radar data are combined with buoy observations to estimate the shape of the wave spectrum high frequency tail and further corroborate the findings of Chapter 2. This chapter is reproduced from proceedings of the *2024 IEEE/OES Thirteenth Current, Waves and Turbulence Measurement (CWTM)*:

> Davis, J. R., Thomson, J., Butterworth, B. J., Houghton, I. A., Fairall, C., Thompson, E. J., and De Boer, G. Multiscale measurements of hurricane waves using buoys and airborne radar. In *2024 IEEE/OES Thirteenth Current, Waves and Turbulence Measurement (CWTM)*, Wanchese, NC, USA, March 2024a. IEEE. doi: 10.1109/CWTM61020.2024.10526332.

Chapter 4 builds on Chapters 2–3 by investigating the spatial distribution of mean square slope within Hurricane Idalia (2023). Analysis focuses on the dependence of mean square slope on the alignment of the wind and wave directions, or *wind-wave alignment*, which has a distinct spatial pattern within storms. This chapter has been published as:

> Davis, J. R., Thomson, J., Houghton, I. A., Fairall, C. W., Butterworth, B. J., Thompson, E. J., De Boer, G., Doyle, J. D., and Moskaitis, J. R. Ocean Surface Wave Slopes and Wind-Wave Alignment Observed in Hurricane Idalia. *Journal of Geophysical Research: Oceans*, 130(2), February 2025. doi: 10.1029/2024JC021814.

Chapter 5 heads north to explore the application of DAS to a submarine fiber-optic cable that runs offshore of Oliktok Point, Alaska. Supervised machine learning is used to estimate seafloor pressure, and thus wave elevation, from measurements of along-cable strain. This work is in preparation for submission to a journal.

Chapter 6 synthesizes and reflects on the key findings of Chapters 2–5. This chapter closes with suggestions for future research.

1.3 Background and Motivation

Waves in hurricanes

Hurricane-generated waves pose an operational hazard to ships at sea and contribute to infrastructure damage at the coast (Kennedy et al., 2011; Duncan et al., 2021). Wave radiation stress gradients[1] produce wave-driven setup, which contributes to compound flooding during storms (Dietrich et al., 2011). Inside hurricanes, waves control momentum transfer between the atmosphere and ocean (Donelan et al., 2012). The rate of momentum transfer, or *air-sea drag*, is a crucial parameter in the accurate modeling of both hurricane intensity and storm surge (Davis et al., 2008). When steep waves break, they generate sea spray which enhances heat transfer at high wind speeds (Barr et al., 2023).

Despite a reckoning that an accurate understanding and representation of wave-driven dynamics is critical to improving hurricane forecasts (Emanuel, 2003), the mechanics and relative

---

[1] Pressures induced by waves as they run into shore, which can cause water to pile up on land.

importance of these processes remains an open question. For several decades, air-sea interaction researchers have observed a stark change in the relationship between air-sea drag and wind speed both in the field and in the lab (Powell et al., 2003; Donelan, 2004; Curcic and Haus, 2020). Drag increases monotonically with increasing wind speed until about 25–30 m/s, beyond which the functional dependence changes. The cause of this change—foam, sea spray, wave breaking, or all three?—and even the functional dependence on wind speed—saturation or rollover?—continue to be debated. Much of this uncertainty is due to the difficulty of directly observing these processes inside hurricanes.

Chapters 2–4 characterize the ocean surface beneath hurricanes using wave slope. It has long been theorized that wind stress, and thus the drag coefficient, should depend on wave slope (e.g., Plant, 1982; Donelan et al., 2012; Janssen and Bidlot, 2023). But how should wave slope be defined in a broadband ocean? In the slope-based roughness length parameterizations proposed by Taylor and Yelland (2001), and later by Edson et al. (2013) for use in the popular COARE algorithm, wave slope is defined as the ratio of significant wave height to the wavelength at the spectral peak, H_s/L_p. This “bulk” slope definition reduces the wave spectrum into a single representative wave height and wavelength.

An alternative slope definition (the one used here) is the *mean square slope*, a high-order moment of the wave energy density spectrum estimated by integration over many frequencies. While mean square square slope still represents slope as a single value, we hypothesize it is preferred over H_s/L_p for several reasons: 1) it captures a broader portion of the spectrum; 2) it emphasizes the spectral “tail”, which includes the short waves theorized to drive stress; and 3) it is more stable in cases where the wave spectrum has multiple peaks. Interestingly, Taylor and Yelland (2001) cite earlier work by Anctil and Donelan (1996) as motivation for a slope-based roughness length parameterization, but they replace the (root) mean square slope metric used in Ancil and Donelan’s original formulation with H_s/L_p. This choice may have been a practical matter, as both H_s and L_p can be estimated without knowledge of the wave spectrum (e.g., from altimeters, radar, and parametric models). Today, wave spectra are readily available from global wave models and buoys (both large and small), and mean square slope is widely reported from satellites and airborne radar. (Still, care should be taken when calculating mean square slope from frequency spectra, particularly at high wind speeds where surface-relative platform drift can affect estimates (Davis et al., 2025).) Donelan continued to promote mean square slope as an important parameter well into his later work (Donelan et al., 2012; Donelan, 2018). The ideas proposed in Donelan (2018) are a major inspiration for Chapter 2 (Davis et al., 2023b).

To capture the rapid evolution of waves inside hurricanes, field measurements must be targeted, well-placed, and capable of resolving a broad range of scales. Historically, hurricane waves were mainly characterized using aircraft- and satellite-based synthetic aperture radar, SAR (e.g., King and Shemdin, 1978; Gonzalez et al., 1982). These measurements are well-suited for providing synoptic views of wave direction and length, however it is challenging to determine wave height from SAR images (reliable algorithms for estimating bulk parameters, such as significant wave height, have only recently been developed, Romeiser et al., 2015). Altimeters have been used to estimate significant wave heights across storms, though these observations are typically limited to narrow beams below satellite nadir (Tamizi and Young, 2020). Airborne radar altimeters, including the Scanning Radar Altimeter (SRA) and more recently, the Wide Swath Radar Altimeter (WSRA), provide estimates of surface roughness (via mean square slope) and directional wave spectra (Wright et al., 2001; Walsh et al., 2021). These directional spectra are sufficient to estimate significant wave height and peak wave directions, but the SRA and WSRA are unable resolve waves shorter than 50 m (~0.17 Hz) or 80 m (~0.14 Hz), respectively. Data from moored wave buoys, including opportunistic observations from existing networks (e.g., Esquivel-Trava et al., 2015) and observations from strategic deployments (e.g., Collins et al., 2018b), have provided hurricane spectral wave information across a broader range of frequencies (0.05 to 0.5 Hz), but buoys tend to be sparse and storm crossings are infrequent. In recent decades, the proliferation of air-deployable instruments has enabled targeted data collection in hurricanes (e.g., Black et al., 2007). This approach aims to combine the direct measurement capabilities of in situ instruments, such as buoys, with the synoptic nature of radar. For instance, Schönau et al. (2024) use observations from drifting wave buoys deployed in Hurricane Michael (2018) to characterize wave spectra across multiple storm quadrants.

In this work, arrays of low-cost, free-drifting wave buoys are deployed from aircraft ahead of hurricanes to measure waves across the entire storm simultaneously. Buoy data are complimented by the WSRA, which flies aboard the “Hurricane Hunter” P-3s. Together, these instruments provide a spatially-dense, multiscale view of waves in hurricanes, supporting new insight into the evolution of waves at high wind speeds and their spatial heterogeneity within storms. Davis et al. (2023b) and Davis et al. (2024a), reproduced in Chapters 2 and 3, use these observations to characterize how ocean surface roughness created by both large, energetic waves and smaller, steeper waves change with wind speed. Davis et al. (2025), Chapter 4, explores how this roughness varies within a storm.

1.3.1 NOPP Hurricane Coastal Impacts project

Chapters 2–4 rely on data from the NOPP[2] Hurricane Coastal Impacts Project (NHCI) which ran from 2021 to 2025 (Houghton et al., 2025). The NHCI project was a collaborative effort between hurricane forecasters, coastal modelers, and field observationalists with the shared goal of improving predictions of coastal flooding, morphologic change, and infrastructure damage caused by hurricanes. Our team, comprised of researchers from the UW Applied Physics Lab (UW-APL), Sofar Ocean, and NOAA, was tasked with collecting offshore wave observations. Across three hurricane seasons, NOPP teams deployed 105 instruments into six hurricanes (Figure 1.1), totaling over 4,000 wave observations within 500 km of a hurricane center (about the size of a typical hurricane). Three types of drifting wave buoys were deployed: microSWIFTs (UW-APL), Spotters (Sofar Ocean), and Directional Wave Spectra Drifters (Scripps Institution of Oceanography). The engineering and development of microSWIFT software, hydrodynamics, and air-deploy rigging were a central focus of the first two years of my PhD (Thomson et al., 2023).

Buoys were deployed 2–3 days ahead of each storm from an NP-3C aircraft operated by the Naval Research Laboratory’s Scientific Development Squadron (VXS-1). Criteria for deployment included potential for landfall with risk to life and property. In addition to the data archives

---

[2] National Oceanographic Partnership Program

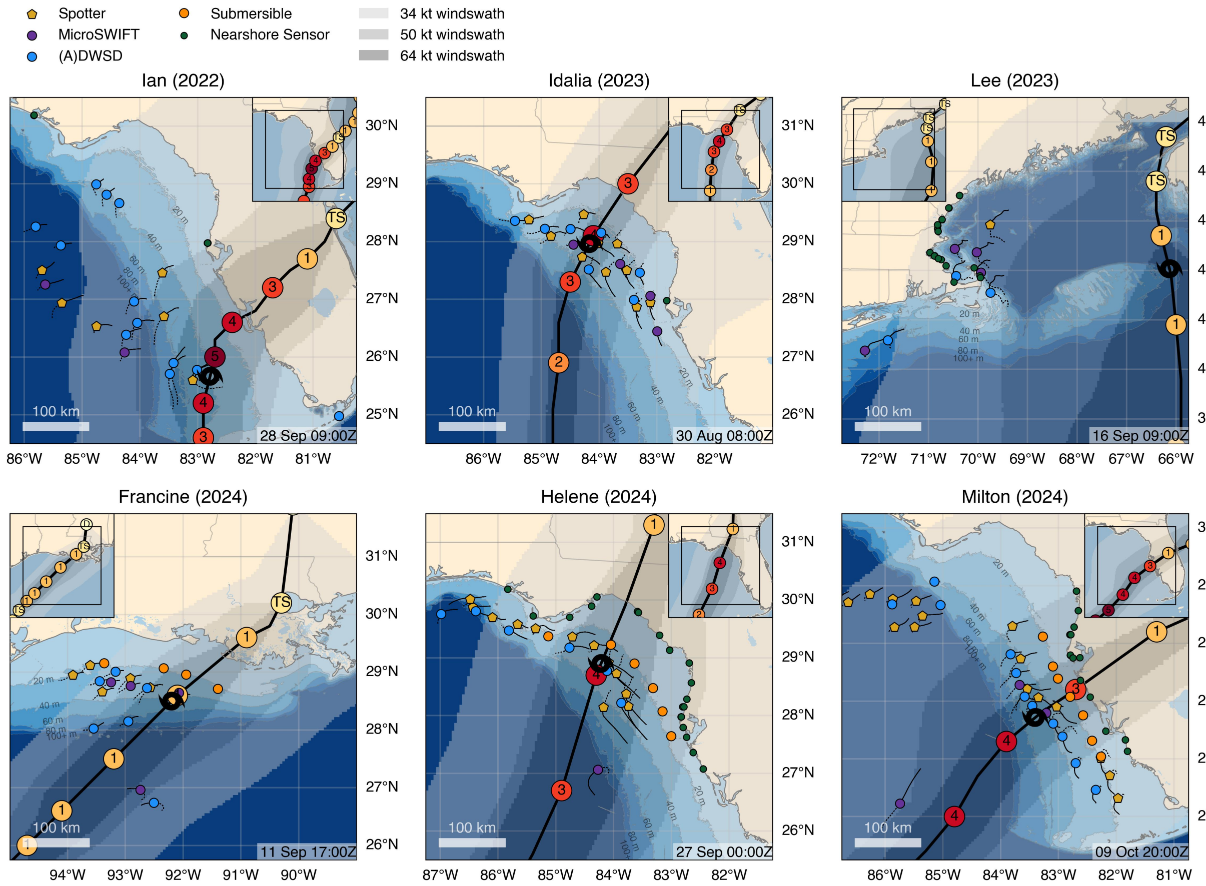

Figure 1.1: Drifting wave buoys deployed in hurricanes Ian (2022), Idalia (2023), Lee (2023), Francine (2024), Helene (2024), and Milton (2024). In each map, the position of the hurricane and drifting wave buoys are shown at the time indicated in the lower right corner. Buoy drift tracks are solid prior to this time, and are dashed after. Hurricane intensity on the Saffir-Simpson Hurricane Wind Scale is indicated along the track, and shaded regions represent the extent of the 34, 50, and 64 knot wind swaths (as reported by NHC). Bathymetry contours are constructed from the GEBCO grid for the respective year.

published with Chapters 2–4, NHCI data from APL-developed microSWIFTs are published as:

> Davis, J., et al. (2025). MicroSWIFT Ocean Surface Wave Data in Hurricane Ian (2022). Designsafe-CI. https://doi.org/10.17603/DS2-C5G3-X778
>
> Davis, J., et al. (2025). MicroSWIFT Ocean Surface Wave Data in Hurricane Idalia (2023). Designsafe-CI. https://doi.org/10.17603/DS2-GB5F-7462

Davis, J., et al. (2025). MicroSWIFT Ocean Surface Wave Data in Hurricane Lee (2023). Designsafe-CI. https://doi.org/10.17603/DS2-CPM6-J967

Davis, J., et al. (2025). MicroSWIFT Ocean Surface Wave Data in Hurricane Francine (2024). Designsafe-CI. https://doi.org/10.17603/DS2-QHT0-9179

Davis, J., et al. (2025). MicroSWIFT Ocean Surface Wave Data in Hurricane Helene (2024). Designsafe-CI. https://doi.org/10.17603/DS2-E3MN-KQ84

Davis, J., et al. (2025). MicroSWIFT Ocean Surface Wave Data in Hurricane Milton (2024). Designsafe-CI. https://doi.org/10.17603/DS2-EP26-EK43

Reports summarizing wave observations collected by microSWIFT, Spotter, and DWSD buoys in each hurricane are published as:

Davis, J. (2025). NHCI Hurricane Ian Buoy Observation Summary. Designsafe-CI. https://doi.org/10.17603/DS2-KSY4-WX93

Davis, J. (2025). NHCI Hurricane Idalia Buoy Observation Summary. Designsafe-CI. https://doi.org/10.17603/DS2-H7HK-GM04

Davis, J. (2025). NHCI Hurricane Lee Buoy Observation Summary. Designsafe-CI. https://doi.org/10.17603/DS2-ZCFR-BN42

Davis, J. (2025). NHCI Hurricane Francine Buoy Observation Summary. Designsafe-CI. https://doi.org/10.17603/DS2-0HVC-RB73

Davis, J. (2025). NHCI Hurricane Helene Buoy Observation Summary. Designsafe-CI. https://doi.org/10.17603/DS2-8RQW-ZF92

Davis, J. (2025). NHCI Hurricane Milton Buoy Observation Summary. Designsafe-CI. https://doi.org/10.17603/DS2-YD5C-TG94

Access to all NHCI-related datasets is documented at:

Moskaitis, J., et al. (2025) NHCI: NOPP Hurricane Coastal Impacts, Designsafe-CI. https://doi.org/10.17603/DS2-Y6NC-P158

Software and data specific to Chapters 2–4 can be found under the “Open Research” headers following each chapter’s Conclusions section.

Efforts to compare observations to model predictions (e.g., WAVEWATCH III) are ongoing. These data (Figure 1.1) likely represent the densest wave observations collected in hurricanes to date. We encourage the community to continue using the NHCI datasets to improve our understanding of hurricane wave dynamics and coastal impacts.

Waves in the Arctic

The wave climate along the Arctic coast is highly variable and seasonably-dependent. The coast is generally protected from waves by landfast ice[3] that forms in the fall during the autumn "freeze-up" and persists through the winter until the spring "break-out" gives way to open water conditions (Mahoney et al., 2014). A typical cross-shore extent of the landfast ice is 20 km, though total ice area has been declining (Yu et al., 2014). Landfast ice is not resolved in the global reanalysis products (e.g., ERA5) used to study longer-term coastal erosion processes, which can lead to substantial bias in wave climate projections (Hošeková et al., 2021). Accurate projections of wave action at the coast are essential, as long-term erosion rates in the Arctic can be on the order of tens of meters per year, with some of the highest rates reported in the Beaufort Sea (Gibbs and Richmond, 2017). During the spring transition period, waves at the coast are limited both by the availability of fetch and attenuation by landfast ice (Thomson and Rogers, 2014). The eventual break out is driven by forcing from a variety of mechanical and thermal sources.

To capture and understand sharp gradients and temporal changes of waves in the coastal Arctic, field measurements must be spatially dense and persistent. Most measurements of waves near the coast, including waves in the presence of landfast ice, are from point measurements such as buoys, on-ice motion sensors, bottom pressure moorings, or tripod-mounted acoustic Doppler current profilers (Sutherland and Rabault, 2016; Hošeková et al., 2020, 2021). Cross-shore gradients can be determined from adjacent point measurements (e.g., Hošeková et al., 2021). Synoptic methods, such as airborne lidar, have also been used to measure waves further offshore in the marginal ice zone (Sutherland et al., 2018). Recently, algorithms for estimating in-ice directional wave spectra from ICESat-2 altimetry have been developed (Hell and Horvat, 2024). While moored point measurements benefit from persistence, their spatial density is limited by

---

[3] Ice attached to, or grounded near, land.

the number of instruments that can be deployed and maintained. Airborne lidar and satellite altimetry achieve high spatial resolution, but their persistence is limited by flight time or by a satellite's revisit period.

Here we combine two emerging technologies in oceanography—distributed acoustic sensing (DAS) and machine learning—to measure waves from a submarine fiber-optic cable off the coast of Alaska's North Slope. Seafloor DAS can transform submarine fiber-optic cables into dense networks of cross-shore sensors, and has previously been used to measure ocean currents (Williams et al., 2022), study wave-ice interactions (Smith et al., 2023), explore nearshore processes (Glover et al., 2024b), detect tsunamis (Xiao et al., 2024), and more. This high spatial resolution makes DAS a valuable tool for studying waves in the coastal Arctic, as it can be used to characterize processes such as wave attenuation and scattering in sea ice. The ability to interrogate a cable for long time periods enables DAS to capture seasonal variations in these processes (e.g, break-out versus freeze-up). When combined with the prevalence of existing submarine fiber-optic cables, typically used for cross-ocean telecommunications, DAS has enormous potential as a persistent ocean observing technology, particularly in data-scarce regions such as the Arctic.

DAS measures along-cable strain, which can be used as a proxy for seafloor pressure induced by ocean surface waves. The difficulty of deriving an analytical transformation from strain amplitude to pressure amplitude has motivated empirical (or semi-empirical) methods (Smith et al., 2023; Meulé et al., 2024). Current approaches, however, do not generalize well to cables and conditions with a nonlinear relationship between pressure and strain. Machine learning-based models provide a path forward for estimating waves from DAS sites with complex pressure-strain relationships (Chapter 5).

1.3.2 Distributed Acoustic Sensing at Oliktok Point, Alaska

Chapter 5 uses DAS data collected on a submarine fiber-optic cable offshore of Oliktok Point in Prudhoe Bay, Alaska. The cable, owned and operated by Quintillion, is primarily used for telecommunications, providing internet and telephone service to Prudhoe bay. The section of cable used in this work crosses the continental shelf of the Beaufort Sea along the 150th meridian

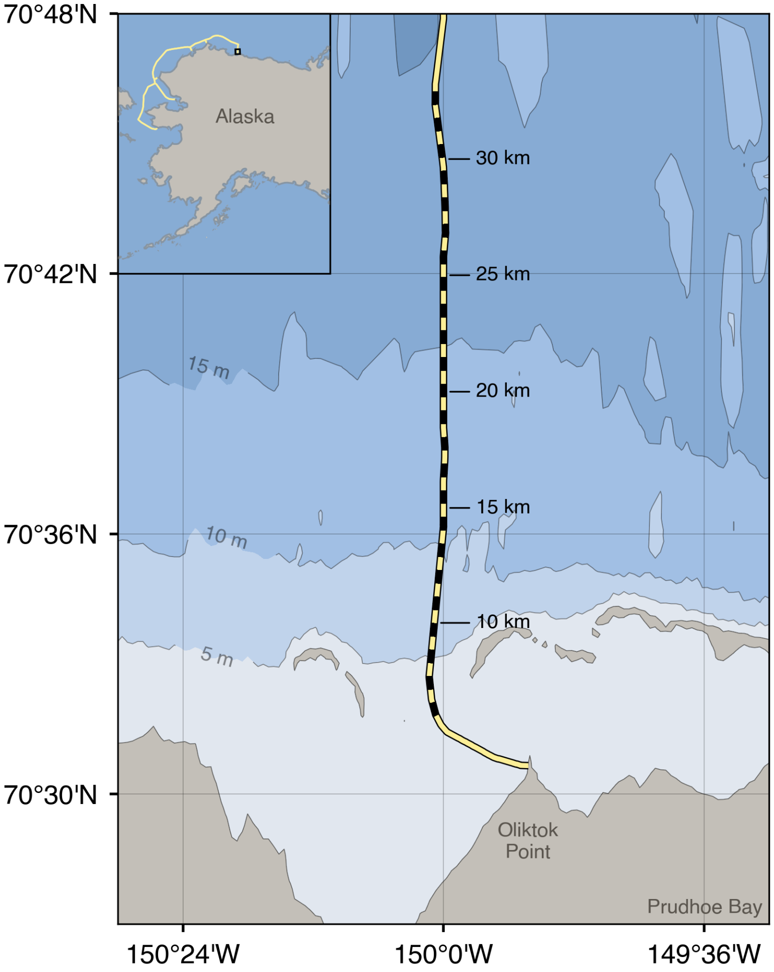

Figure 1.2: Submarine fiber-optic cable (yellow) offshore of Oliktok Point in Prudhoe Bay, Alaska. The dashed portion of the cable represents the 27.1 km of cable used in this work. The inset map in the upper left corner shows the site in the context of Alaska and the full Quintillion submarine cable network.

west, where it terminates at an onshore station in Prudhoe Bay (Figure 1.2). The cable is trenched approximately 2–4 m into the seabed over this run. One of the cable's dark fibers[4] has been leased and interrogated by researchers at Sandia National Laboratories since 2021 (Baker and Abbott, 2022). The cable has been interrogated using both DAS and distributed temperature sensing

---

[4] Unused fibers originally installed as excess capacity.

(DTS), and the data have been used to map sea ice coverage (Baker and Abbott, 2022), track ice edges (Peña Castro et al., 2023), characterize submarine permafrost (Stanciu et al., 2023), and observe wave-ice interactions (Smith et al., 2023).

Data used in Chapter 5 are DAS strain rate measurements collected in summer 2023. Three seafloor pressure moorings stationed along the cable, which had earlier been deployed through the ice in April 2023, provide ground truth estimates of surface wave elevation during this period (Thomson and Smith, 2024). Hourly pressure spectra measured by these moorings are used as targets for developing supervised machine learning-based methods to measure waves with DAS.

Chapter 2

SATURATION OF OCEAN SURFACE WAVE SLOPES OBSERVED DURING HURRICANES

Abstract: *Drifting buoy observations of ocean surface waves in hurricanes are combined with modeled surface wind speeds. The observations include targeted aerial deployments into Hurricane Ian (2022) and opportunistic measurements from the Sofar Ocean Spotter global network in Hurricane Fiona (2022). Analysis focuses on the slope of the waves, as quantified by the spectral mean square slope. At low-to-moderate wind speeds ($\leq$ 15 m s^{-1}), slopes increase linearly with wind speed. At higher winds ($>$ 15 m s^{-1}), slopes continue to increase, but at a reduced rate. This trend persists through extreme winds, up to the highest wind speed in the dataset (54 m s^{-1}). The mean square slopes are directly related to the wave spectral shapes, which over the resolved frequency range (0.03 to 0.5 Hz) are characterized by an equilibrium tail (f^{-4}) at moderate winds and a saturation tail (f^{-5}) at higher winds. The asymptotic behavior of wave slope as a function of wind speed could contribute to the reduction of surface drag at high wind speeds.*

2.1 Introduction

The physical slope of ocean surface waves, defined as the ratio of a wave's height to its length (H/L) or product of its amplitude and wavenumber (ak), is widely found to play a governing role in the exchange of momentum at the air-sea interface. Slope is essential in the parameterization of deep-water breaking processes (Duncan, 1981; Melville, 1994; Drazen et al., 2008; Schwendeman et al., 2014; Schwendeman and Thomson, 2017, and others) and is theorized to contribute to the air-sea drag coefficient through modulation of the aerodynamic roughness (Taylor and Yelland, 2001; Troitskaya et al., 2012; Takagaki et al., 2012, 2016; Donelan, 2018; Lan et al., 2022). Efforts to characterize slope as a function of wind speed trace back to Cox and Munk (1954), who used optical measurements of the sun's glint to measure the distribution of slopes in wind speeds ranging from 1 to 14 m s^{-1}. This work was followed by an extensive set of satellite radiometer measurements reported by Bréon and Henriot (2006) up to 12 m s^{-1}, the airborne lidar-based measurements of Lenain et al. (2019) from 2 to 13 m s^{-1}, and most recently, the spaceborne measurements of Guérin et al. (2022) and Li et al. (2022) up to 15 m s^{-1} and 20 m s^{-1}, respectively. These works universally agree that, in low-to-moderate winds, the mean square of the slope distribution, or *mean square slope*, increases linearly with wind speed. Dynamics above 20 m s^{-1} remain less thoroughly investigated.

The mean square slope (mss) is a metric that quantifies the average steepness of waves over a range of frequencies or wavenumbers. When estimated from the wave energy density spectrum (sea surface elevation variance spectrum), it is an integral quantity proportional to the fourth moment of the spectrum. It can be calculated across any portion (or the entirety) of the spectrum, and it is closely related to the shape of the spectrum itself. Typically, the actively forced, wind-driven gravity wave spectra in hurricanes have a single peak followed by a broad spectral "tail" (Young, 2003). The canonical tail of a wind-driven gravity wave spectrum has two distinct regions: an *equilibrium range* and a *saturation range* (Forristall, 1981; Banner, 1990; Lenain and Melville, 2017). The *equilibrium range* is defined by a balance of wind input, dissipation from breaking, and nonlinear energy fluxes. It begins just beyond the peak frequency and is characterized by a distinct f^{-4} spectral slope in frequency, or $k^{-5/2}$ in wavenumber space (Toba, 1973; Phillips, 1985). At frequencies beyond the equilibrium range, a *saturation range* exists, where the wind input is balanced by dissipation from breaking (Forristall, 1981; Banner, 1990; Romero et al., 2012; Lenain and Melville, 2017). This region is characterized by a spectral slope of f^{-5} (k^{-3} in wavenumber space). In the remaining discussion, the "saturation" range will be referred to as the "dissipation" range to avoid confusion with the use of saturation to describe the wind speed dependence of mss.

Wave slope and spectral shape, particularly the tail, are closely tied to the wind forcing. Through the use of a Phillips (1985) analytical expression for spectral energy in the equilibrium range related to mean square slope, Thomson et al. (2013) demonstrated the feasibility of estimating wind stress based on wave spectral observations alone. In that work, the equilibrium-derived estimates of wind speed compare well with observed wind speeds up to 15 m s^{-1}, enabling operational use of the method to derive proxy wind speeds in the Sofar Spotter global network

(Voermans et al., 2020). However, at higher wind speeds, the dependence of mss remains largely unexplored, except in models (Donelan, 2018) and in the laboratory (Takagaki et al., 2012, 2016).

The complex nature of hurricane waves has been studied and reported on for over a century (Cline, 1920) with the first in situ observations emerging around 1970 (Patterson, 1974; Whalen and Ochi, 1978, for example). Waves evolve rapidly in hurricanes, especially in fast-moving storms under which the "extended" or "effective" fetch (King and Shemdin, 1978) and duration of forcing changes with storm translation speed (Kudryavtsev et al., 2015; Hwang, 2016; Hwang and Fan, 2017; Hsu et al., 2019; Hell et al., 2021). Wave directions vary dramatically based on location relative to the center of the storm, with large wind-wave misalignment possible in the left quadrants (Walsh et al., 2002; Young, 2006; Hwang and Walsh, 2018; Collins et al., 2018a; Tamizi and Young, 2020; Hsu, 2021a). The interaction of waves and currents can also be significant (Yujuan et al., 2018; Hegermiller et al., 2019; Bruciaferri et al., 2021; Sun et al., 2022). Waves, both breaking and non-breaking, play a substantial role in the exchange of momentum and heat at the air-sea interface (Holthuijsen et al., 2012; Hsu et al., 2017; Kita and Waseda, 2022). This literature has lacked an observed relation between wave slopes and wind speeds in hurricanes that can be used to improve the modeling of surface stress and wave growth in this extreme environment (Janssen and Bidlot, 2023). These physics are essential for the modeling of tropical cyclone intensity and coastal inundation.

Here, we use buoy spectral measurements in hurricane winds to study the evolution of wave slope and spectral shape as a function of modeled wind speed. Section 2.2 describes the determination of mss from the buoys and describes the coupled model used for surface wind speeds. Section 2.3 presents the results, and Section 2.4 discusses the implications and relation to other studies. Section 2.5 concludes.

2.2 *Methods*

2.2.1 *Mean square slope definition*

An estimate of the wave mean square slope can be computed from a frequency spectrum as (Ticona Rollano et al., 2019, for example),

$$\mathrm{mss} = \int_{f_{\min}}^{f_{\max}} \frac{(2\pi f)^4\, E(f)}{g^2} df \tag{2.1}$$

Here f represents the wave frequency, $E(f)$ is the energy density, and g is the acceleration of gravity. This expression is directly proportional to slope squared $(ak)^2$ using the linear dispersion relationship in the deep water limit, $(2\pi f)^2 = gk$, and with $E(f) \propto a^2$. The definite integral represents an estimate of the mean square slope over a frequency extent defined by its minimum and maximum frequencies, $f_{\min}$ and $f_{\max}$. Here, the limits are taken as the lowest and highest reported frequencies of the spectrum resolvable by the finite-sized wave buoy, $f_{\min} = 0.0293$ Hz to $f_{\max} = 0.5$ Hz in $n = 38$ discrete bands, where the upper limit is set by the hydrodynamic response of the hull. We emphasize that this mean square slope metric characterizes the shape and slope contributions of the energetic scales of the spectrum, but cannot account for waves shorter than approximately 6.3 m in wavelength (see section 2.4.1).

2.2.2 *Spotter wave buoy*

Wave measurements were collected by free-drifting Spotter buoys (Sofar Ocean) which use GPS-derived motions to report hourly records of surface wave statistics in the form of scalar energy spectra and directional moments (Raghukumar et al., 2019). Raw data are collected at a 2.5 Hz sampling rate and processed into 256-sample FFTs to produce spectral estimates spanning 0.0293 Hz to 0.5 Hz in 38 bins. A constant frequency resolution of df=2.5/256 Hz is used up to 0.33 Hz, beyond which the resolution is coarsened to $3 \cdot df$ to reduce the size of the processed data which are transmitted hourly over the Iridium network. Observed spectra are corrected for Doppler shift due to a 1.2% wind slip and Stokes drift, velocity components which cause Spotters to move relative to the intrinsic wave reference frame.[1] The Doppler shift correction is described in detail in section 4.2.4 of Chapter 4.

Spotter data is collected through a combination of targeted deployments and opportunistic measurements from Sofar's spotter network—a large, persistent array of free-drifting Spotter buoys (Houghton et al., 2021). The density of the deployed arrays and Sofar's network help to overcome the sparsity of moored buoy arrays when targeting hurricanes. The Spotter's smaller hull size also has a good response to shorter waves, which can be underestimated by some larger buoys in the NBDC network (Jensen et al., 2021). The sphere-like hull is 42 cm in diameter with a mass of 7.5 kg including ballast.

2.2.3 COAMPS-TC model

Surface wind field estimates are derived from real-time operational forecasts made by the U.S. Naval Research Laboratory's (NRL) Coupled Ocean-Atmosphere Mesoscale Prediction System for Tropical Cyclones (COAMPS-TC) (Doyle et al., 2012, 2014). COAMPS-TC is a regional model which uses an outer fixed grid mesh (36-km horizontal resolution) and two nested storm-following grid meshes (12- and 4-km resolution) with 40 vertical levels ranging in altitude from 10 m above the surface to approximately 30 km. When producing real-time operational forecasts, the version of COAMPS-TC used in this study utilizes the NOAA Global Forecast System (GFS) analysis and forecasts for the initial and boundary conditions. For storms that have intensities greater or equal to 55 knots (28.3 m s^{-1}), the horizontal wind structure at the initial time of the model is generated from a modified Rankine wind vortex model combined with both physical and synthetic observations ingested from the National Hurricane Center. For time periods when the storm intensity is less than 55 knots at the initialization time, the initial TC vortex is downscaled from the NOAA GFS analysis.

Hourly 10-m winds from the inner-most 4-km grid are derived by aggregating successive forecasts leaving out the first four hours of each forecast to minimize the effect of model state

---

[1] Subsequent results differ from those presented in Davis et al. (2023b), which are not Doppler-adjusted.

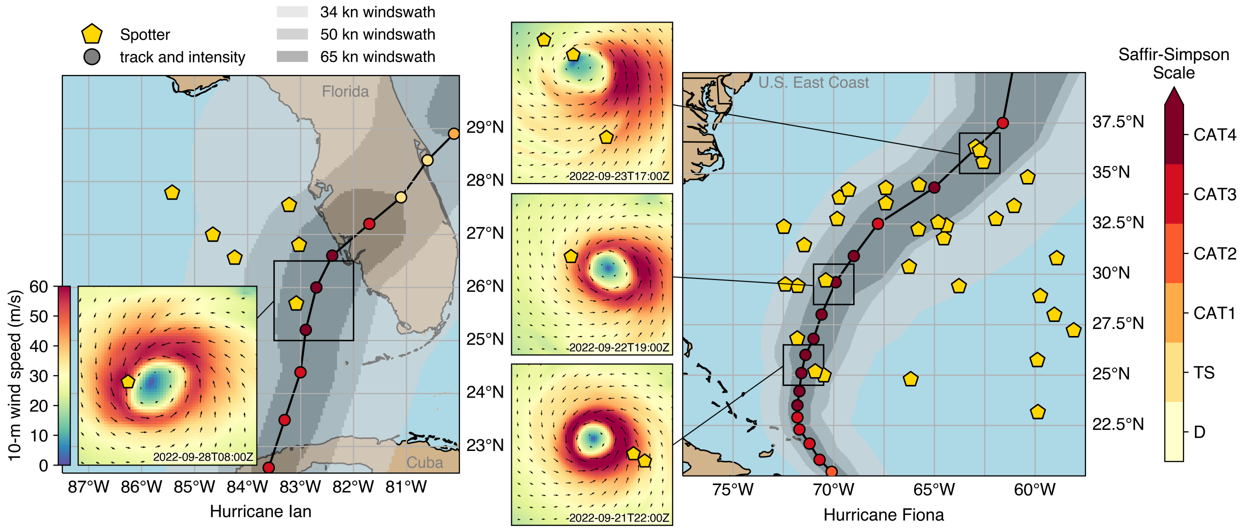

Figure 2.1: Buoy locations and storm track for Hurricane Ian (left) and Hurricane Fiona (right). Storm tracks are colored by intensity, as categorized by the Saffir-Simpson scale, and the surrounding wind swaths are shaded by wind speed threshold. The insets highlight several buoy-storm interactions using 10-m wind speeds from COAMPS-TC.

adjustments that occur early in each forecast. The 10-m winds are instantaneous values (representative of a 1-10 minute average) and gustiness is not resolved. Wind output is interpolated onto Spotter wave observations to produce wind-wave datasets in Hurricane Fiona (2022) and Hurricane Ian (2022).

2.2.4 Targeted deployment measurements in Hurricane Ian (2022)

Hurricane Ian was a Category 4 hurricane that caused widespread damage to both Cuba and the Southeastern United States during late September 2022. Ahead of Ian's first U.S. landfall on the Southwest coast of Florida, the continental shelf was seeded with an array of drifting buoys in a targeted deployment by an NP-3C aircraft (Figure 2.1) operated by Naval squadron VXS-1. Observations from six Spotter buoys in the array are co-located with wind fields from COAMPS-TC to create a dataset of 432 hourly wave measurements and modeled wind speeds from September 27 to 30, 2022. Wave observations span 2 m to 11.8 m significant wave height and

5 s to 13 s peak period, and mostly lie between the 30 m and 100 m depth contours, approximately 90 km to 275 km offshore (see Appendix, Figure 2.6). The maximum COAMPS-TC wind speed at the time and location of a Spotter observation is 52.5 m s^{-1} (117 mph).

2.2.5 Sofar Spotter Network measurements in Hurricane Fiona (2022)

Hurricane Fiona was a destructive hurricane that formed in mid-September 2022 and made landfall in Puerto Rico and the Dominican Republic before traveling northward across the Atlantic, peaking in intensity as a Category 4, then striking Eastern Canada as an extratropical cyclone. Fiona's track through the open Atlantic intersected with several buoys in Sofar's Spotter network. The 2772 hourly observations from 33 Spotters (Figure 2.1) contain measurements up to 17.5 m significant wave height and 20.5 s peak period, with a maximum interpolated model wind speed of 54.4 m s^{-1} (122 mph).

2.3 Results

2.3.1 Mean square slope versus wind speed

At low-to-moderate wind speeds (< 15 m s^{-1}), observed mean square slopes have a linear dependence on 10-m surface-level wind speed (Figure 2.2). This result is qualitatively consistent with the measurements of Cox and Munk (1954) at wind speeds of 2-14 m s^{-1}.

At higher wind speeds (> 15 m s^{-1}), the increases in observed mss are much smaller. This trend persists through the extent of available buoy data, up to the maximum wind speed of 54.4 m s^{-1} (122 mph) as modeled by COAMPS-TC. Bin centers shown in Figure 2.2 represent the mean and standard deviation of mss in each bin. Bins centered on wind speeds [2.5, 5.5, 8.5, 12.5, 17.5, 22.5, 30, 40, 50] m s^{-1} have mss mean ± standard deviation values of [0.002 ± 0.001, 0.004 ± 0.002, 0.007 ± 0.002, 0.012 ± 0.002, 0.015 ± 0.002, 0.017 ± 0.002, 0.019 ± 0.002, 0.023 ± 0.001, 0.024 ± 0.002]. Lateral uncertainty in the wind speed is estimated using COAMPS-TC 6-h forecast error relative to the National Hurricane Center best track re-analysis. A 7 m s^{-1} error is placed on high wind speeds ($\geq$ 25 m s^{-1}), near the radius of maximum winds, which derives

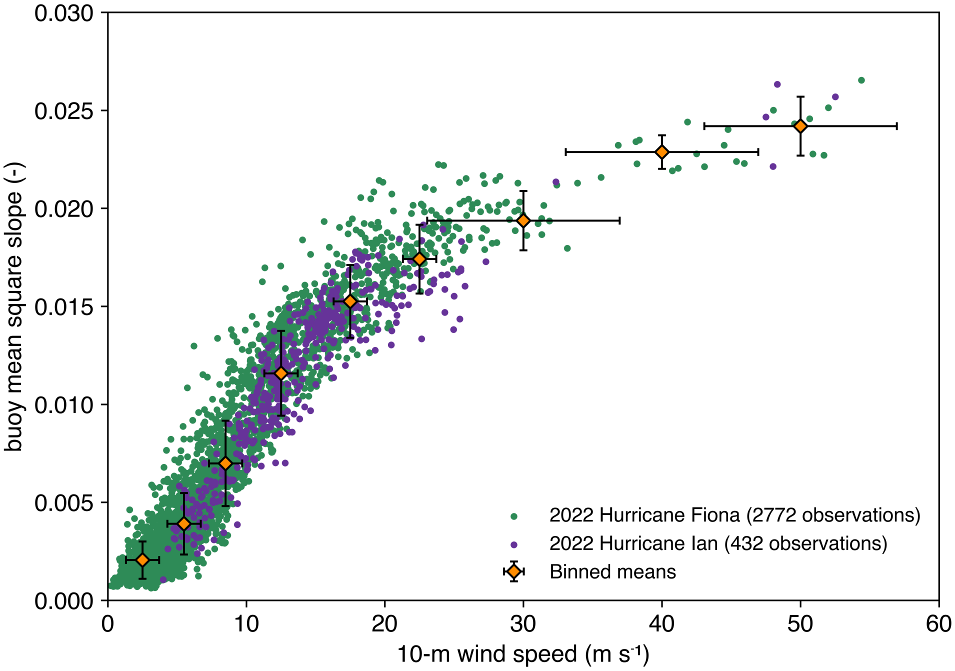

Figure 2.2: Spotter mean square slope from wave measurements in Hurricanes Ian and Fiona as a function of COAMPS-TC 10-m wind speed. Bin centers are the mean mss in each bin, and vertical error bars are standard deviations. Lateral error bars represent uncertainty in COAMPS-TC wind speeds.

from the standard deviation of the distribution of COAMPS-TC 6-h intensity errors evaluated for hundreds of major hurricane forecasts. A 1.2 m s^{-1} error is used at lower wind speeds (< 25 m s^{-1}), located in the outer part of the storm, and is estimated from an error distribution created by shifting the COAMPS-TC forecast on top of the best track position and comparing the updated wind speed at the buoy's position to the originally-forecasted wind speed.

Ticona Rollano et al. (2019) observed wave slope saturation with wind speed starting at 11 m s^{-1} and noted the behavior to be qualitatively similar to the saturation of measured turbulent dissipation in the ocean surface layer. In wind-wave flume experiments, Troitskaya et al. (2012) found wave slope to have a tendency toward saturation, which was coincident with saturation of their lab-measured air-sea drag coefficients above wind speeds of 25 m s^{-1}. The authors attribute

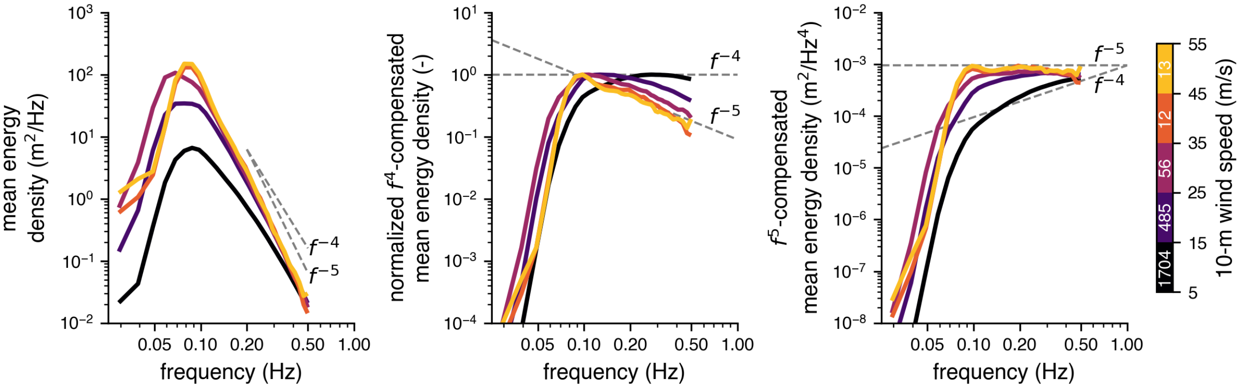

Figure 2.3: *Left panel*: mean energy density in 10 m s^{-1} bins. Bin counts (1-hour spectra) are labeled inside of the color bar. *Center panel*: the mean energy spectra compensated by f^4 (as *energy* $\cdot f^4$) and normalized by their respective maximum value. In such a scaling, f^{-4} trends collapse to a constant line (as indicated by the correspondingly labeled dashed line). *Right panel*: mean energy spectra compensated by f^5.

the decrease in slope to the "tearing of the wave crests at severe wind conditions." The University of Miami Wave Model predicts a similar transition in mean square slopes at high winds (Donelan, 2018). A more complete comparison with other mss results from the literature is given in the discussion (Sec 2.4.1).

2.3.2 *Spectral shape change with wind speed*

Mean square slope is a measure of both the physical wave slope (a^2k^2) as well the wave spectral shape (i.e., as the fourth moment of the spectrum). The evolution of the observed wave spectra with wind speed is shown in Figure 2.3 as the mean energy density in 10 m s^{-1} bins. At low-to-moderate wind speeds ($<$ 15 m s^{-1}), the spectral tail above 0.10 Hz follows the canonical f^{-4} slope expected of the equilibrium range (wind input, dissipation from breaking, and nonlinear energy fluxes in balance).

From 15 to 25 m s^{-1}, the frequency extent of the equilibrium range is shorter and the tail of the spectrum, from 0.2 Hz onward, transitions to the f^{-5} slope characteristic of the dissipation range (wind input balanced solely by dissipation). This change is coincident with the weakening of the wind speed dependence of mss in Figure 2.2. The equilibrium range (f^{-4}) continues to narrow with increasing wind speed, until the spectral tail is almost entirely dominated by the dissipation range (f^{-5}) at the most extreme winds (45 to 55 m s^{-1}). For any given total wave energy (or significant wave height), the change in spectra shape to f^{-5} results in a reduction in mss relative to an f^{-4} shape with the same total energy. Though much of this energy is contained in lower frequencies of the spectrum, changes in the high frequency tail have the highest influence on the mss integral due to the f^{4} dependence of Equation (2.1). Thus, wave heights can continue to increase with increasing wind speed, while mss saturates. The growth of the peak wavelength as a function of wind speed is specific to the evolution of a storm, but approaches 200-300 m near 40 m s^{-1} for both hurricanes (Appendix, Figure 2.9).

The spectral slopes are in general agreement with the large number of hurricane wave observations collected by Tamizi and Young (2020) which vary from f^{-4} to f^{-5}. Observations of the transition in spectral tail slope from f^{-4} to f^{-5} by Vincent et al. (2019) and Lenain and Melville (2017) demonstrate the transition frequency (and wavenumber) decreases with increasing wind speed (in wind speeds up to 20 m s^{-1}). While neither result extends to the extreme, 54 m s^{-1} wind speeds observed here, the transition frequency appears to decay exponentially with an apparent asymptote at 0.30 Hz in the Vincent et al. (2019) data (max winds 20 m s^{-1}).

Spectra with a narrow f^{-4} range and dominant f^{-5} tail are also present in the SWIFT buoy observations of Schwendeman et al. (2014), consistent with results in Figure 2.3. The authors note the SWIFT spectra derive from young, highly forced waves (which is the case here) as defined by the wave age, or the ratio of wave phase speed to the 10-m wind speed. A similar trend is described in Romero and Melville (2010), who demonstrate a narrowing of the equilibrium range with decreasing wave age. When binned by wave age, Spotter spectra exhibit the same wave age dependence (Appendix, Figure 2.5).

2.4 Discussion

2.4.1 Limitations of wave scales observed by buoys

It is well known that buoys cannot measure waves shorter than a few meters because the hydrodynamic response of their hull is limited to frequencies higher than the natural frequency (typically 0.5-1.0 Hz, see Thomson et al. (2015) for details). At low-to-moderate wind speeds and wave conditions, a substantial portion of the total mean square slope is supported by shorter waves only measurable by methods such as lidar (Lenain and Melville, 2017; Lenain et al., 2019) and polarimetry (Zappa et al., 2008). The buoy mss can be partially corrected by incorporating empirical parameters into (2.1) which effectively extrapolate the spectra to higher frequencies,

$$\text{adjusted mss} = \alpha \int_{f_{\min}}^{f_{\max}} \frac{(2\pi f)^4 E(f)}{g^2} df + \beta. \tag{2.2}$$

The empirical factors α and β are introduced to account for the mean square slope contributions of the higher frequency waves not resolvable by the Spotter buoy (i.e., waves shorter than $f_{\max} =$ 0.5 Hz or 6.3 m in wavelength). Fitting α in Equation (2.2) to Cox and Munk (1954) over the linear regime of Figure 2.4 (from 2 to 15 m s^{-1}) yields $\alpha = 5.0$ with an offset of β=0.011.

In Figure 2.4, adjusted mss (with α=5.0 and β=0.011) is compared to the data of Cox and Munk as well as the slopes modeled by Donelan (2018) using the University of Miami Wave Model. The Miami wave model includes the full spectrum of gravity, capillary-gravity and capillary waves in prescribing mss. In all datasets, the transition to a regime with weaker mss dependence on wind speed is observed near 15 m s^{-1}, corresponding to an approximate mss of 0.08 or $\tan(16\,\text{deg})^2$ as identified by Cox and Munk (1954). The adjusted mss and Donelan results are in good agreement across all wind speeds. The Miami model exhibits a sensitivity to fetch above 30 m s^{-1} (which is beyond the scope of the present study). Interestingly, the adjusted buoy mss in Figure 2.4 approaches the upper limit on omnidirectional mean square slope proposed by Plant (1982), $\text{mss}_{\max} = 0.08 \pm 0.04$, or using the upper value, $\text{mss}_{\max} = 0.12$. The limit is proposed based on requirement that the flux of momentum from wind to waves should not exceed the wind stress

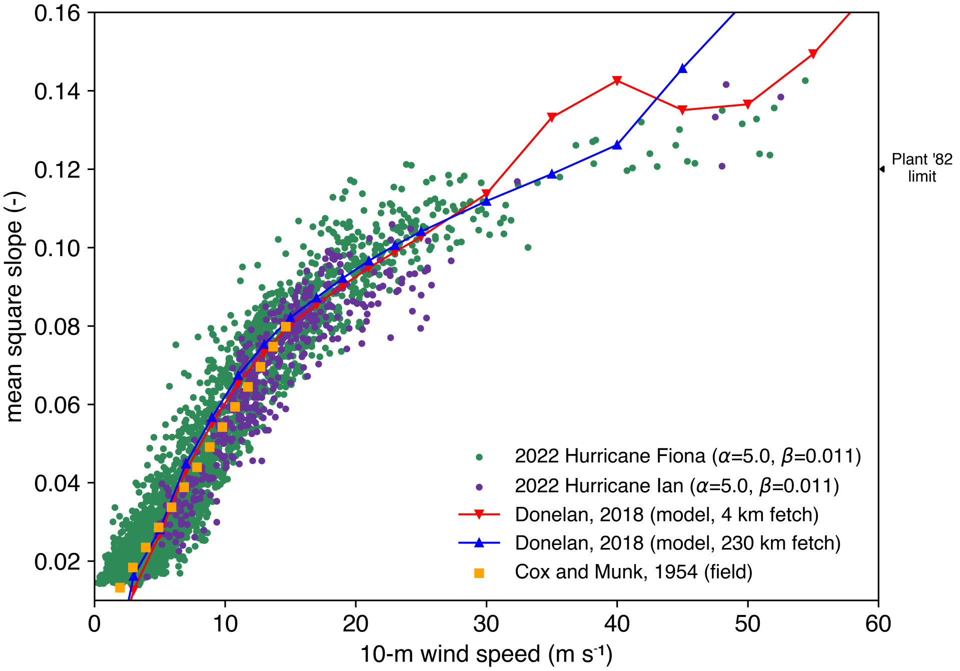

Figure 2.4: Adjusted mean square slope, calculated from Equation (2.2) with α=5.0 and β=0.011 using wave measurements in Hurricanes Ian and Fiona, as a function of model 10-m wind speed. The classic field measurements of Cox and Munk (1954) are superimposed along with the University of Miami Wave Model slope estimates at fetches of 4 km and 230 km from Donelan (2018).

for wave growth proportional to $(u^*/c)^2$ (ratio of friction velocity to wave phase speed, squared), and is employed by Elfouhaily et al. (1997) to vet several candidates for parametric spectra.

While useful for a rough comparison of buoy mss to slopes calculated over larger frequency extents, there remains large uncertainty in the use of α and β to correct buoy mss to total mss. The coefficient α is biased when the transition from the equilibrium range to the dissipation range (Figure 2.3) is well within the frequencies resolvable by the buoy, which occurs around wind speeds of 15 to 20 m s^{-1}, since the contribution to mss of a saturated portion of the spectrum is less significant than that of an equilibrium portion of the spectrum (or similarly higher-sloped portion). An alternative approach is to extend the observed f^{-5} tail, however this would not capture the evolution of the wave spectrum in the gravity-capillary range (wavelengths less than

1 m down to several millimeters) which changes shape with increasing wind speed (Zappa et al., 2008; Laxague et al., 2018). A parametric tail, e.g. Elfouhaily et al. (1997), could be imposed, but many parameterizations are developed on wind speeds not exceeding 20 m s^{-1}.

In future work, the NOAA Wide Swath Radar Altimeter (WSRA) and Stepped Frequency Microwave Radiometer (SFMR) instruments are good candidates for producing relevant datasets of hurricane winds and waves (Walsh et al., 2021; Klotz and Uhlhorn, 2014). The WSRA measures wave topography (which can be used to compute mss) and SFMR provides a measure of surface wind speed. Both fly concurrently aboard the NOAA WP-3D aircraft during Hurricane Hunter missions.

2.4.2 Considerations for free-drifting platforms

A free-drifting, buoy-based observation of wave steepness fundamentally relies on time series and thus frequency analysis. Doppler shift of the observed wave spectrum can occur when a measurement platform propels in or against waves (Collins et al., 2017) or when waves pass through gradients in surface currents (Iyer et al., 2022). At high wind speeds, it is unlikely that such waves can exist without the presence of a surface currents. While Spotter buoys mostly make observations in a wave-following, intrinsic reference frame, the surface-relative drift induced by windage (wind slip) can become significant at high wind speeds. Spotter data are thus corrected for Doppler shift due to both wind slip and stokes drift (see Chapter 4, section 4.2.4). Future studies should focus on a direct measurement of slope using other technologies.

2.4.3 Implications for surface drag coefficient

The air-sea drag coefficient, which governs the rate of momentum transfer between the air and ocean surface, depends on the surface roughness length under neutral stability (Charnock, 1955). Using a groundbreaking set of GPS sonde tropical cyclone field measurements, Powell et al. (2003) observed a saturation and eventual reduction in both roughness length and drag coefficient at extreme wind speeds. More recent studies have verified this result and added functional dependencies (e.g., Holthuijsen et al. (2012)). The subsequent adoption of a reduced drag coefficient in models has been essential to improving tropical cyclone intensity forecasts (Davis et al., 2008, for example). The evolution of mean square slope presented here is qualitatively similar, increasing steadily through moderate winds before leveling-off at higher wind speeds. Taylor and Yelland (2001) demonstrated the ability of a roughness length scaling based on bulk wave slope (H_s/L_p, or the ratio of significant wave height to peak wavelength) to predict observed roughness across a wide range of datasets, including the open ocean. This bulk steepness is closely related to mss and shares a tendency to saturate at high wind speeds in our data (Appendix, Figure 2.8). Takagaki et al. (2012) report a similar H/L roughness dependence in the lab. The roughness length dependence wave slope, combined with the saturation of slopes at high wind speeds observed here, might thus contribute to the reduction of the drag coefficient at hurricane force wind speeds.

The observed progression of spectral shape can be directly linked to sea-state dependent drag. Plant (1982) hypothesized a wave growth function proportional to $(u^*/c)^2$ where the friction velocity u^* is a function of the wave energy spectrum within the equilibrium range of the spectral tail (Phillips, 1985). Here, the f^{-4} equilibrium range narrows rapidly for winds exceeding 25 m s^{-1} and is replaced by the f^{-5} dissipative range, leading to enhanced wave breaking. In addition to limiting wave steepness, intense wave breaking promotes the generation of spray, which becomes increasingly present within a multi-phase surface foam layer and is hypothesized to modulate the drag coefficient for winds above 30 m s^{-1} (Holthuijsen et al., 2012; Troitskaya et al., 2016, 2019; Hwang, 2018, and others). Recently, Lan et al. (2022) achieved notable tropical cyclone model skill improvement through the use of a roughness parameterization that depends both on sea state and foam, employing the Taylor and Yelland (2001) slope scaling at low wave ages (<15.2) and the Drennan et al. (2003) wave age scaling at higher wave ages.

Though a mean square slope integrated to frequencies beyond the buoy observations might be necessary for a direct relation to the skin friction component of the drag coefficient, the slope of the waves measured by buoys remains important to the understanding of form drag and pressure work (Kudryavtsev and Makin, 2007; Donelan, 2018, and others). The buoy measurements, though lacking the very highest frequency waves, include the vast majority of the total energy in the wave spectrum. More practically, the buoy measurements are the wave information most readily available for real-time assimilation into coupled forecast models.

2.4.4 Secondary dependencies of mss at high winds

Although this set of buoy data has been sufficient to determine a parametric relation between mss and wind speed, it has not been sufficient to determine secondary dependencies. Building on ideas from the literature, we have tested the residual scatter from a tanh fit to the data for dependence on storm quadrant (position relative to the center and heading of the storm), wind-wave alignment, wave age, and storm speed. While none of these tests show a statistically significant result, there are some possible signals. When viewing the time series of each individual buoy rather than the aggregated data, the mss values are higher for a given wind speed when the winds and waves are well-aligned. The alignment dependence would be consistent with formulations for wind-wave growth that utilize the wind stress vector and the wave celerity vector (Gemmrich et al., 1994). Porchetta et al. (2019) found alignment can improve the parameterization of roughness length, observing an increase in roughness with large misalignment, though the authors report it has almost no effect in young waves. Depth also plays a role in the transformation of waves in shallow water, however spectrograms of relative depth indicate that the frequencies of interest to mss, 0.10 Hz and above, remain above the deep water limit (Appendix, Figure 2.6). Dependency on storm quadrant may be obscured by COAMPS-TC track position errors, though the standard deviation of 6-h track errors (based on hundred of major hurricane forecasts) is 21 km, likely not large enough to place a buoy at the edge of the eyewall on the other side of the eye (e.g., Appendix, Figure 2.7)

2.5 Conclusions

Ocean surface wave buoy measurements within two hurricanes show a consistent regime change in the relation of wave slopes to wind speeds. Up to moderate wind speeds (< 15 m s^{-1}), wave slopes increase linearly with wind speed, as has been documented in the literature. At higher wind speeds (15 to 54 m s^{-1}), the rate of mss increase with wind speed is drastically reduced.

When adjusted to account for mss contributions from shorter waves, the highest mss values are close a heuristic value of 0.12 proposed by Plant (1982). This mss limit is directly related to the emergence of an f^{-5} dissipation (saturation) range as the dominant shape of the scalar wave energy spectra under high wind speeds. The wave slope changes are likely related to changes in the surface drag coefficient, for which a more comprehensive dataset of mss coincident with momentum fluxes is needed to evaluate. A larger dataset of wave observations in hurricanes will be valuable for considering secondary effects, such as dependencies on storm quadrant, wind-wave alignment, interaction between swell and wind-sea, and storm speed.

Open Research

The wind and wave data originally used in Davis et al. (2023b) are publicly available on Dryad at `https://doi.org/10.5061/dryad.g4f4qrfvb` (Davis et al., 2023a). The storm track and speed data used to test secondary dependencies were sourced from IBTrACS (Knapp et al., 2010a, 2018). Shapefiles of the storm track and wind swaths used in the maps are from the National Hurricane Center GIS Archive available at `https://www.nhc.noaa.gov/gis/`.

Acknowledgments

This work was funded by the U.S. National Ocean Partnership Program (NOPP) as part of the NOPP Coastal Hurricane Impacts project. Co-authors Doyle, Komaromi, and Moskaitis gratefully acknowledge support from Office of Naval Research grant Program Element (PE) 0601153N. Computational resources for the COAMPS-TC forecasts were provided by the Navy Department of Defense Supercomputing Resource Center in Stennis, Mississippi. Air-support was provided by the Navy VXS-1 Scientific Deployment Squadron via the Naval Research Laboratory. The Spotter global network data was provided by Sofar Ocean.

This material is based upon work supported by the National Science Foundation Graduate Research Fellowship Program under Grant No. DGE-2140004. Any opinions, findings, and conclusions or recommendations expressed in this material are those of the author(s) and do not necessarily reflect the views of the National Science Foundation.

Appendix

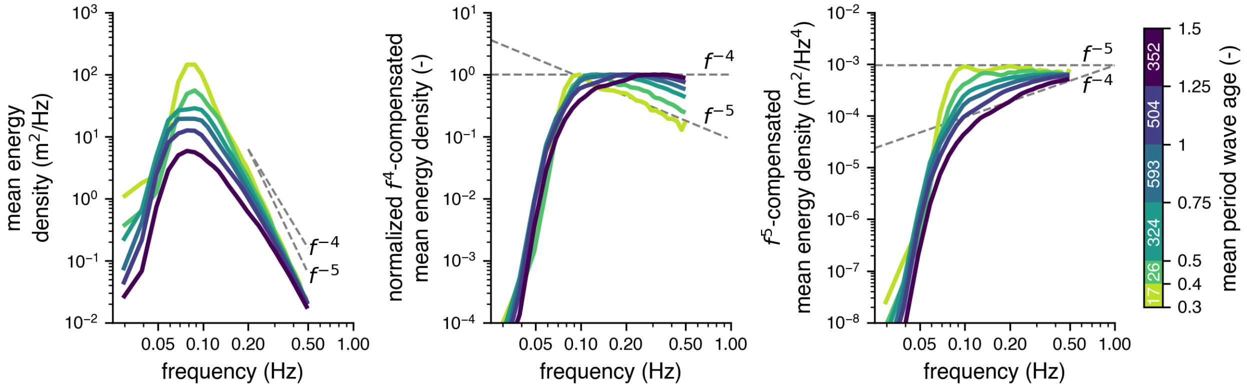

Figure 2.5: *Left panel*: mean energy density binned by wave age (bin counts labeled inside color bar). The wave age is calculated as the ratio of the wave phase speed, at the mean period, to the 10-m wind speed. Bin resolution is increased at low wave ages to highlight the behavior of young seas. *Center panel*: mean energy spectra compensated by f^4 (as *energy* $\cdot f^4$) and normalized by their maximum value. *Right panel*: mean energy spectra compensated by f^5.

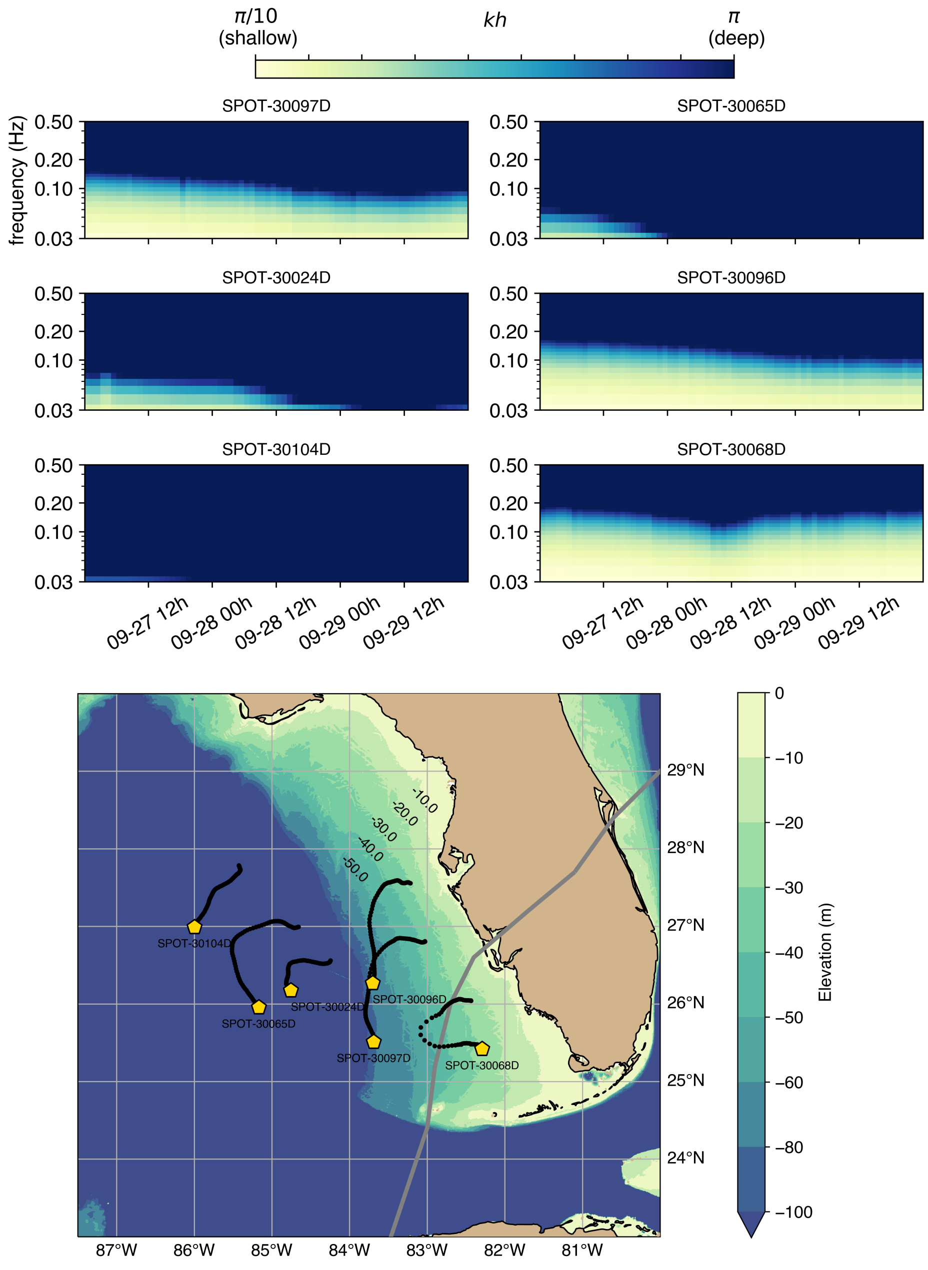

Figure 2.6: *Upper panel*: spectrograms of *kh* (product of wavenumber and depth) for each Spotter in Hurricane Ian. The color bar extent is placed at the deep and shallow water limits such that values beyond either limit saturates. *Lower panel*: bathymetry of the Florida shelf. The Spotter drift tracks are shown in black and the end of each track is marked by a gold symbol. The best track is shown as a grey line. Elevations (negative depths) are from GEBCO 2023.

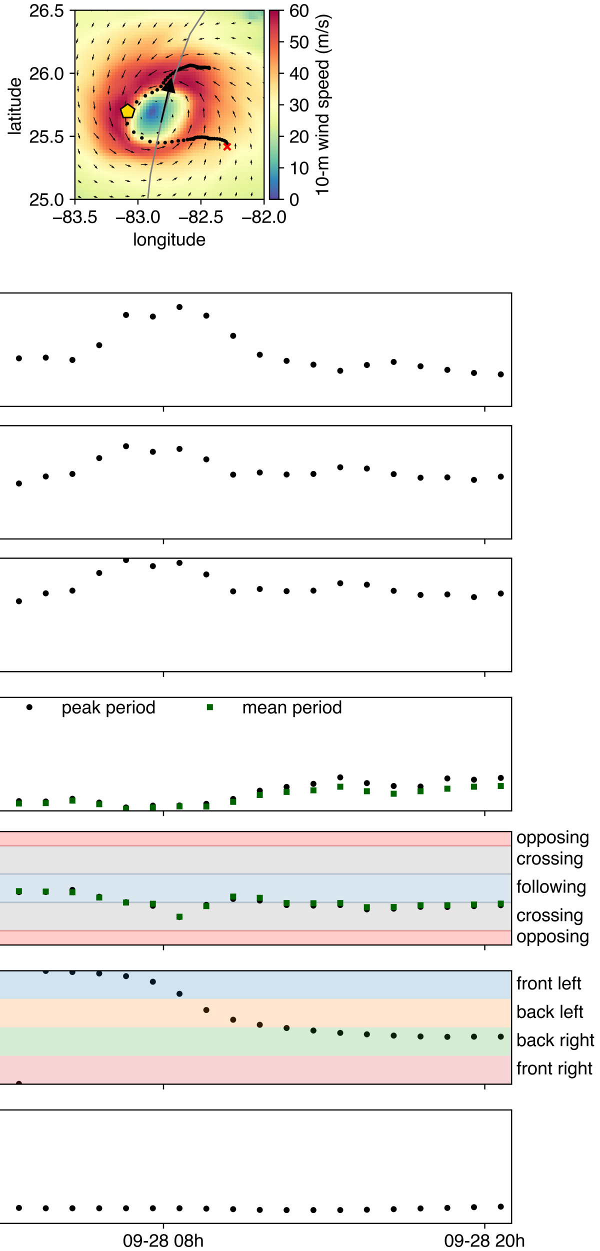

Figure 2.7: Spotter-Ian time series. In the topmost image, the hurricane and Spotter buoy are shown at the mean time. Their trajectories are shown as a grey line with a black arrow (hurricane path and direction) and as black dots (hourly buoy positions). The red ‘x’ indicates the end of the buoy’s trajectory. Where applicable, metrics derived from both the peak and mean periods are indicated as black dots and green squares, respectively.

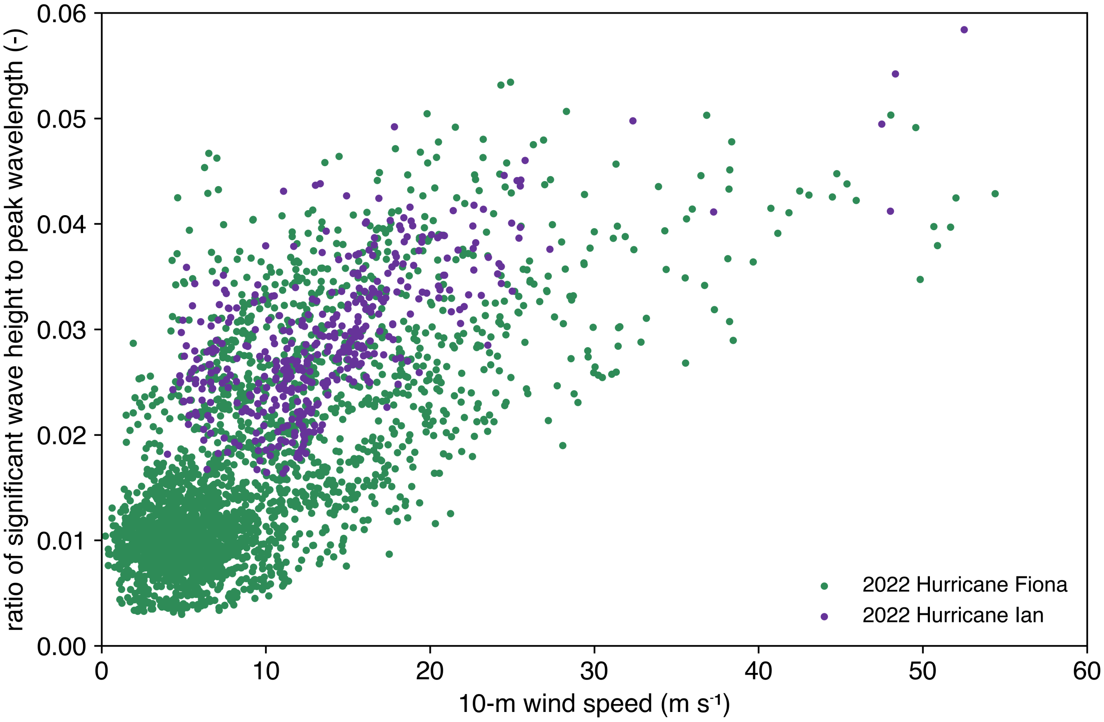

Figure 2.8: Ratio of significant wave height to peak wavelength (bulk steepness, H_s/L_p) versus model wind speed.

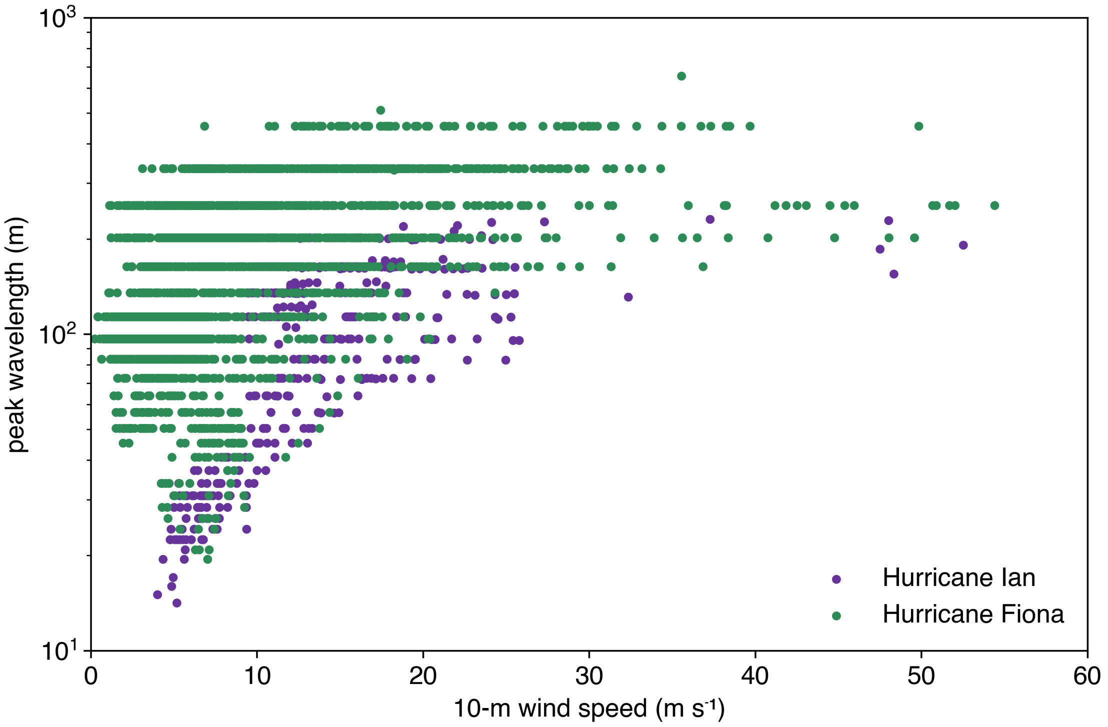

Figure 2.9: Spotter peak wavelength (L_p) versus wind speed.

Chapter 3

MULTISCALE MEASUREMENTS OF HURRICANE WAVES USING BUOYS AND AIRBORNE RADAR

Abstract: *The processes important to hurricane wave generation cover scales from kilometers to centimeters. Within a storm, waves have complex spatial variations that are sensitive to hurricane size, strength and speed. This makes it challenging to measure the spatial variability of hurricane waves with any single instrument. To obtain both broad spatial coverage and resolve the full range of wave scales, we combine arrays of drifting wave buoys with airborne radar altimetry. The microSWIFT (UW-APL) and Spotter (Sofar) buoys are air-deployed along a given storm track. These buoys resolve the scalar wave frequency spectrum from 0.05 Hz to 0.5 Hz, which is approximately 600 m to 6 m wavelength (in deep water). The Wide Swath Radar Altimeter (WSRA) flies into hurricanes aboard the NOAA Hurricane Hunter P-3 aircraft. The radar altimetry data is processed to produce a 2D directional spectrum from 2.5 km to 80 m wavelength, and the radar backscatter provides an estimate of the mean square slope down to centimeter wavelengths. We introduce a method to use colocated mean square slope observations from each instrument to infer the shape of the spectral tail from 0.5 Hz to almost 3 Hz. The method is able to recover the frequency* f^{-5} *tail characteristic of the saturation range expected at these frequencies (based on theory and measurements in lower wind speeds). We also explore the differences between WSRA and buoy mean square slopes, which represent the mean square slope of the intermediate wavelength waves (6 m down to 20 cm). Together, the fusion of these wave measurements provides a multiscale view of the hurricane-generated waves. These ocean surface waves are critical as drivers of the air-sea coupling that controls storm evolution and as drivers of coastal impacts by hurricanes.*

3.1 Introduction

The ocean surface wave energy spectrum spans wavelengths from kilometers to millimeters. The tail of the spectrum is important for understanding wave-induced stress (Hwang, 2005; Reichl et al., 2014; Chen et al., 2020b). The canonical tail of the scalar wave frequency spectrum is typically described in terms of two distinct regions which have different dynamic balances: the *equilibrium range* and the *saturation range*. The equilibrium range arises due to a balance of wind input, dissipation from breaking, and nonlinear energy fluxes, and is characterized by an f^{-4} tail in frequency (Toba, 1973; Phillips, 1985). The higher frequency saturation range follows the equilibrium range, as marked by a "transition frequency". Within the saturation range, wind input is balanced by dissipation from breaking, and the spectrum has an f^{-5} tail which extends to the high frequency, short gravity waves (Forristall, 1981; Banner, 1990; Lenain and Melville, 2017).

3.1.1 1-D wave spectra in hurricanes

Observations show hurricane wave spectra are mostly unimodal (Young, 2006; Tamizi and Young, 2020), though there are notable exceptions, particularly on the left side of the storm where the wind-sea and swell are propagating in different directions, resulting in two distinct peaks (Hu and Chen, 2011). In Tamizi and Young (2020), the authors fit a JONSWAP spectral model to buoy data and find the spectral tails steepen from f^{-4} to f^{-5} with decreasing wave age (defined as the ratio of 10-m wind speed to the phase speed at the spectral peak). The mean tail exponent of all their observations is −4.68. Hwang et al. find substantial scatter in their observed spectral slopes (between −4 and −5), and instead suggest the treatment of the spectral slope exponent as a random variable (Hwang et al., 2017). The Gaussian fit to their data has a mean of −4.48 and standard deviation of 0.53. Drifting buoy observations from hurricanes suggest that the spectral tail is dominated by the f^{-5} saturation range beyond 30 m s^{-1}(Davis et al., 2023b). These observations do not extend beyond 0.5 Hz (waves shorter than 6 m), such that, in hurricanes, the shape of 1-D wave spectra at higher frequencies remains an open question.

3.1.2 Mean square slope

The mean square slope (mss) of the ocean surface is a high-order moment of the spectrum which is closely related to the tail. When resolved down to sufficiently small wavelengths, mss is widely interpreted as a measure of roughness (Cox and Munk, 1954; Walsh et al., 1998; Hwang, 2005; Boisot et al., 2015; Li et al., 2022). It has also been suggested that mean square slope is related to form drag, which can contribute substantially to the total stress (Donelan et al., 2012; Donelan, 2018; Sullivan et al., 2018).

Mean square slope can be calculated from the wavenumber spectrum as

$$\mathrm{mss} = \int_{k_1}^{k_2} k^2 E(k)\mathrm{d}k \tag{3.1}$$

where $E(k)$ is the ocean wave energy spectrum as a function of wavenumber, k, and k_1 and k_2 define the wavenumber extent over which the spectrum, and thus mss, is resolved. Using the deep water dispersion relationship, $\omega^2 = gk$, where $\omega = 2\pi f$ is angular frequency and g is the acceleration of gravity, wavenumber-based mss (Equation 3.1) can be expressed as a function of the frequency spectrum

$$\mathrm{mss} = \frac{(2\pi)^4}{g^2} \int_{f_1}^{f_2} f^4 E(f)\mathrm{d}f \tag{3.2}$$

where $E(f)$ is the wave energy spectrum as a function of frequency, f. Mean square slope is highly sensitive to the scale of the waves and therefore the magnitude varies across instruments which resolve different wavenumber ranges. It is less sensitive to the lower limit, since long waves contribute little to the mss magnitude (Lenain and Melville, 2017).

Pioneering work by Cox and Munk Cox and Munk (1954) used photographs of sun glitter on the ocean surface collected from an airplane to calculate the slope distribution at 12.5 m wind speeds from 2 m $s^{-1}$to 14 m s^{-1}. Their results show the distribution of wave slopes is nearly Gaussian, and that the variance of the distribution, the mss, increases linearly with wind speed. The optical-nature of their measurements suggest this approaches an estimate of the *total* mean square slope (the mss of the wave spectrum down to the smallest waves in the gravity-capillary and capillary wave regimes). They repeated their experiment in the presence of an oil-slicked surface, which was found to reduce mss by a factor of 2-3. The slick suppresses wavelengths shorter than ~0.3 m (Hwang, 2005). The Cox and Munk mean square slopes have since been corroborated by modern measurement techniques, e.g., lidar, polarimetry, radar, and satellite-based radiance (Bréon and Henriot, 2006; Zappa et al., 2008; Lenain et al., 2019; Guérin et al., 2022). These works agree that mean square slope has a linear dependence on wind speed in winds less than 20 m s^{-1}.

3.1.3 Radar-derived mean square slope

Radar-based remote sensing has been used to make estimates of the sea surface slope distribution for several decades (e.g., Wentz, 1977). Radar are useful for characterizing the surface slope of smaller waves (centimeter-scale) at high wind speeds, since they can be applied in challenging conditions such as hurricanes (Walsh et al., 2014; Hwang and Fan, 2018).

Radar backscatter is proportional to the probability density of surface wave slopes from which the mean square slope can be determined using an optical model (Barrick, 1968; Liu et al., 2000). The radar-estimated mean square slope depends on the scattering regime (e.g., Bragg scattering or quasi-specular) and the wavelength resolution is limited by the radar wavelength.

Jackson et al. (1992) estimated mss using Ku-band radar and reported a linear fit as a function of 10-m wind speed. Their mean square slope estimates are equivalent to Equation 3.1 integrated from small wavenumbers (large wavelengths) to an upper wavenumber of 63 rad m^{-1} (0.1 m wavelength). Observations from Vandemark et al. (2004) using Ka-band radar (upper wavenumber of 250 rad m^{-1} or 0.02 m wavelength) and Walsh et al. (1998) using the NASA Scanning Radar Altimeter at Ku-band have instead reported a logarithmic dependence on wind speed below 15 m s^{-1}. The logarithmic relationship is in better agreement with the laboratory observations of Wu (1990) than with those of Cox and Munk. Similarly, a power-law dependence was reported by Hauser et al. (2008) using C-band radar (upper wavenumber of 51 rad m^{-1}, 0.12 m wavelength) later supported by Chen et al. (2018).

3.1.4 Observations at higher wind speeds

There are few reported estimates of the high frequency spectral tail (frequencies > 0.5 Hz) or of the mean square slope beyond wind speeds of 15 to 20 m s^{-1}. The lack of such estimates in extreme wind speeds has made it challenging to validate the use of spectral wave models, which require an empirical tail at these frequencies, in hurricanes (Reichl et al., 2014; Chen et al., 2020a).

Global positioning system reflectometry (GPS-R), L-band observations of mean square slope have been made in hurricanes in wind speeds up to 59 m s^{-1}(Katzberg et al., 2013; Gleason et al., 2018; Hwang et al., 2021). The GPS-R mss estimates follow a logarithmic form and represent an upper wavenumber of approximately 11 rad m^{-1} (0.57 m). Buoy-based estimates of mss (upper limit 1 rad m^{-1}, 6.2 m) measured in hurricanes effectively saturate beyond 25 m $s^{-1}$and can be described using a tanh relationship up to 54 m s^{-1}(Davis et al., 2023b). Additional, radar-based high wind characterizations of mean square slope appear to be on the horizon (e.g., KaIA and CYGNSS) (Sapp et al., 2021; Carreno-Luengo et al., 2021).

Here we combine hurricane wave observations from buoys and airborne radar to characterize the mean square slope at intermediate wavelengths (6 m to 0.2 m) in high wind speeds. We then introduce a method to use colocated mss observations to infer the slope of the high-frequency spectral tail at these wavelengths (approximately 0.5 Hz to 2.8 Hz).

3.2 Methods

3.2.1 Buoys

Hurricane wave buoy observations are from two types of small, free-drifting wave buoys: the microSWIFT (UW-APL) and Spotter (Sofar). Each uses GPS-derived elevations and velocities to estimate wave elevation. Every hour, the wave elevations are processed into spectra which are telemetered through the Iridium satellite network.

The microSWIFT buoy is an expendable wave buoy sized for deployment through the dropsonde chute of scientific aircraft (Thomson et al., 2023). The buoy is cylindrical with an 8.9 cm diameter, 51.0 cm length, and a mass of 2.9 kg. Wave elevation time series collected at a rate of 4 Hz are transformed to spectra using 256 s windows each with 75% overlap. The spectra are then frequency-merged and output in 42 bins spanning frequencies of 0.05 Hz to 0.5 Hz.

The Sofar Spotter is a sphere-like buoy which is 42 cm in diameter has a mass of 7.5 kg, including ballast (Raghukumar et al., 2019). When air-deployed, the Spotters are specially rigged for deployment through an open door (Dorsay et al., 2023b). Raw data are collected at 2.5 Hz sampling rate and processed into 256-sample FFTs. The final spectra span 0.0293 Hz to 0.5 Hz in 38 bins. A constant frequency resolution of df = 2.5/256 Hz is used up to 0.33 Hz, beyond which the resolution is coarsened to 3 df for bandwidth efficiency when transmitting over the Iridium network.

Data from the full-sized v3 SWIFT buoys were used to evaluate the proposed spectral tail extrapolation method in moderate conditions. The v3 SWIFTs have a 0.35 m diameter hull and a 1.25 m draft (Thomson, 2012). Wave spectra are reported at 42 frequency bins (0.01 Hz to 0.05 Hz) from 8-minute time series of wave elevation. Multiple spectra within a comparison period are averaged, where applicable.

3.2.2 *Wide Swath Radar Altimeter*

The Wide Swath Radar Altimeter (WSRA) is a 16.15 GHz (Ku-band) radar which flies into hurricanes aboard one of the Hurricane Hunter P-3s (Walsh et al., 2014, 2021; PopStefanija et al., 2021). It uses altimetry to estimate the 2-D directional wavenumber spectrum from 2.5 km wavelength down to 80 m. The spectra represent an approximately 14 km^2 area collected over 50 s and are corrected for Doppler shift as well as a skewing effect which occurs as the radar scans perpendicular to wave crests.

The WSRA also uses backscatter to estimate mean square slope based on the geometric optics model, which relates the normalized radar cross section per unit area (σ_0) to mean square slope (Barrick, 1968):

$$\sigma_0 = \frac{|R(0^\circ)|^2}{\mathrm{mss}} \sec^4\theta \exp\left(\frac{-\tan^2\theta}{\mathrm{mss}}\right) \tag{3.3}$$

where $|R(0^\circ)|^2$ is the Fresnel reflection coefficient at normal incidence, θ is the off-nadir angle, and mss is the mean square slope. Under this assumption, when the logarithm of σ_0 is plotted against $\tan^2\theta$, mean square slope is inversely proportional to the slope. In practice, mss is estimated using a fit through the data (PopStefanija et al., 2021).

For the WSRA, this calculation is restricted to off-nadir angles from 0 deg to 14 deg (where 0 deg is pointing directly down at nadir) such that the scattering remains within the quasi-specular regime. When determined using this model, the mean square slope estimate is not sensitive to the calibration of the radar and is likely less sensitive to rain attenuation since all the returns

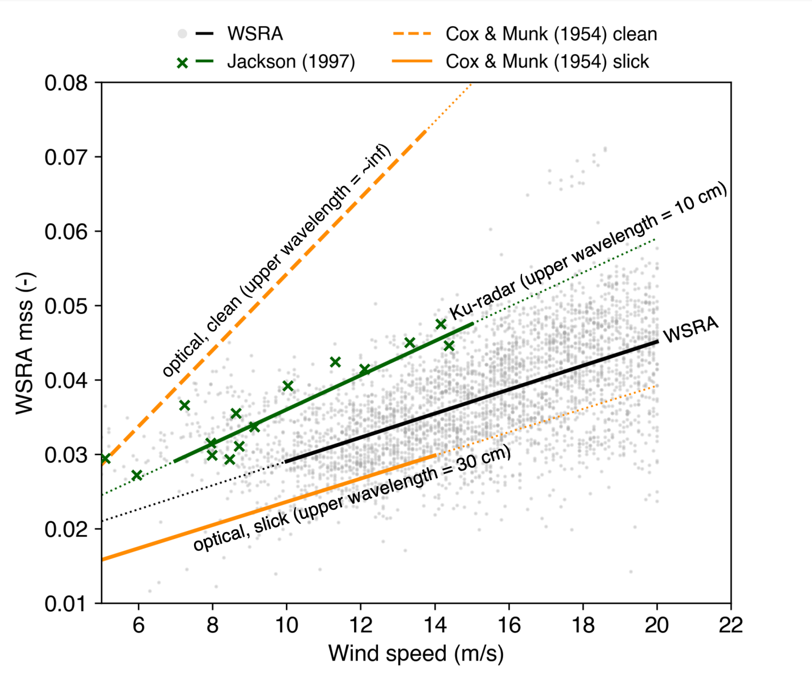

Figure 3.1: WSRA mean square slopes compared to those from Cox and Munk (1954) and Jackson et al. (1992). The black line represents a linear fit to the WSRA data (grey points) from 10 to 20 m s^{-1}. The WSRA mss falls between that of the Jackson et al. (1992) Ku-radar measurements, rigorously determined to have an upper wavelength of 10 cm, and the "slick" sea surface measurements of Cox and Munk (1954) which extend to 30 cm. Linear fits to the mss data are given by: $\mathrm{mss} = 0.003 + 0.00512U_{12.5}$ for $U_{12.5} \in [2, 14]$ m s^{-1}(Cox and Munk, clean), $0.008 + 0.00156U_{12.5}$ (Cox and Munk, slick), $0.013 + 0.0023U_{10}$ for $U_{10} \in [7, 15]$ m s^{-1}(Jackson), and $0.013 + 0.0016U_{10}$ for $U_{10} \in [10, 20]$ m s^{-1}(WSRA).

are attenuated by a similar amount. A minor correction is applied to account for the slightly increased path length further off nadir.

In this scattering regime, the estimated mean square slope represents Equation 3.1 integrated from approximately the width of the swath (100's of meters) down to several times the radar wavelength, λ_r (Jackson et al., 1992). For WSRA, the radar wavelength is λ_r = 1.85 cm. The exact upper wavelength of most quasi-specular mss measurements, sometimes called the diffraction limit, is often not well known, and estimates in the literature range from 2 to 10 times λ_r (Jackson et al., 1992; Vandemark et al., 2004; Hauser et al., 2008). By comparing to prior estimates of mean square slope with known extents, we determine that the upper wavelength resolved by the WSRA is on the order of 0.2 m (20 cm) (Figure 3.1). This corresponds to 10.8 λ_r. The upper limit is sensitive to range of off-nadir angle (which is constant) and possibly wind (Thompson et al., 2005; Hauser et al., 2008).

3.2.3 *Colocated observations*

Colocated buoy and WSRA observations are from three datasets. Buoy observations in hurricanes are from targeted air deployments into Hurricane Ian (2022) and Hurricane Idalia (2023) as part of the NOPP Hurricane Coastal Impacts project (NHCI). The microSWIFT and Spotter buoys intersected with the flight path of the NOAA Hurricane Hunter P-3 carrying the WSRA (H1 and and I1 planes in Ian and Idalia, respectively). The colocated observations are within a 100 km radius and 90 minutes of one another. Additional data from the Atlantic Tradewind Ocean-Atmosphere Mesoscale Interaction Campaign (ATOMIC) (2020) are included for evaluation of the tail extrapolation method at lower wind speeds. The ATOMIC field campaign took place in the tropical North Atlantic east of Barbados January through February 2020 (Quinn et al., 2020; Pincus et al., 2021). Several flight tracks from the P-3/WSRA are directly overhead of the SWIFT drifters.

3.3 Results

3.3.1 *WSRA mean square slope versus wind speed*

WSRA data from hurricanes Earl (2022), Fiona (2022), Ian (2022), Julia (2022), Idalia (2023), and Lee (2023) are combined with 10-m wind speed estimates from the stepped frequency microwave radiometer (SFMR) which flies concurrently aboard the NOAA P-3s (Sapp et al., 2019). The WSRA data are filtered to remain within limits for aircraft roll (±2.5°), altitude (1000-4000 m), ground-speed (80-250 m s^{-1}), and rainfall rate (< 50 mm hr^{-1}). Rainfall rate estimates from both the SFMR and WSRA are used for filtering purposes. SFMR wind speed observations flagged as invalid were excluded.

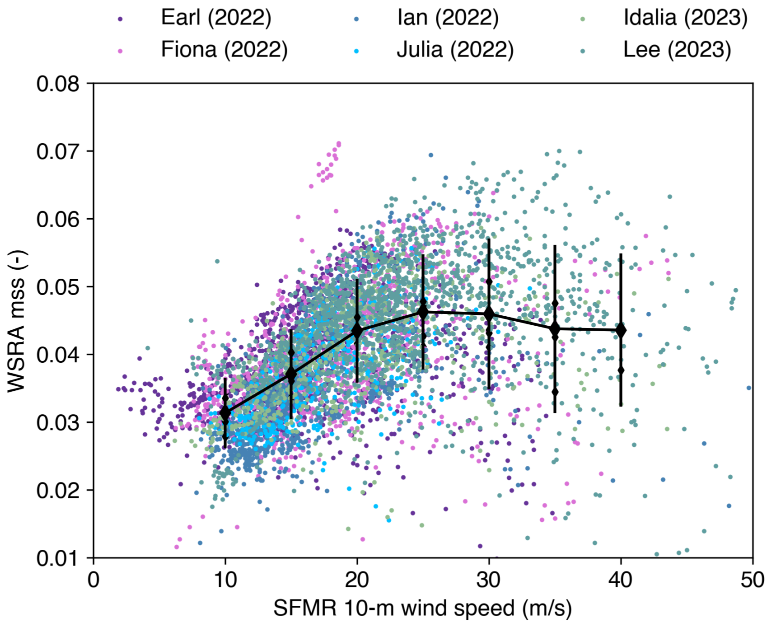

Figure 3.2: WSRA mean square slopes versus SFMR 10-m wind speed, colored by hurricane. Black diamonds indicate bin-averages from the combined data, and the error bars represent one standard deviation in each bin.

WSRA mean square slopes measured in all six hurricanes saturate at high wind speeds and, in many cases, reduce at the highest wind speeds (Figure 3.2). Bin-averages, which include data from all hurricanes, reach a maximum around 25 m s^{-1}, beyond which they reduce slightly and then level-off around 35 m s^{-1}. The WSRA mss wind speed dependence is similar to that of the L-band GPS-R mss summarized in Hwang et al. (2021), though the WSRA mss is higher due to its higher upper wavenumber (31.4 rad m^{-1} compared to 11 rad m^{-1}). Deviation from the linear dependence on wind speed (above 20 m s^{-1}) in the WSRA mss hurricane datasets presented here and from GPS-R are qualitatively similar to those measured by drifting buoys (Davis et al., 2023b).

3.3.2 Mean square slope at intermediate wavelengths

WSRA mss represents waves with lengths from several hundred meters down to 0.2 m (20 cm). While the exact lower limit is not well-defined, the extent overlaps with the wavelengths mea-

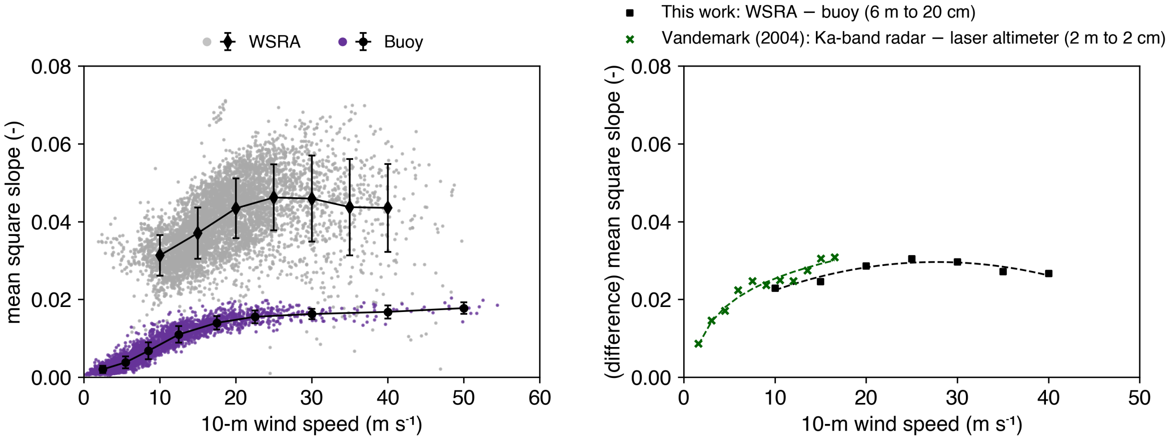

Figure 3.3: WSRA mss and buoy mss (left) and their difference (right), which represents waves from 6 m to 20 cm. The difference is calculated from the bin averaged WSRA mss and buoy mss (diamonds and circles on the left plot). Data from Vandemark (2004) are shown for comparison (their Figure 10, “coastal” observations), including the logarithmic fit $0.004 + 0.0093\ln(U_{10})$ for $U_{10} \in [1.5, 16.5]$ m s^{-1}. Lower wind speed WSRA mss observations are required to fit a comparable logarithmic function to the difference of WSRA mss and buoy mss, however the SFMR does not produce reliable U_{10} estimates at low wind speeds (Sapp et al., 2019). A second-order polynomial fit is shown: $-2.3 \cdot 10^{-5}U_{10}^2 + 0.00128U_{10} + 0.012$. for $U_{10} \in [10, 40]$ m s^{-1}.

sured by buoys, 600 m to 6 m. Assuming the WSRA longer wavelength limit is comparable to that of the buoy, and that these waves have little contribution to the overall mss, the difference of the WSRA mss and buoy mss should approximate the mss of waves between 6 m and 0.2 m. The difference between the mss measurements also saturates with 10-m wind speed (Figure 3.3). The results agree with a set of similar, yet lower wind speed, observations from Vandemark et al. (2004) which represent the difference of a Ka-band radar mss (0.02 m lower wavelength) and a laser altimeter mss (2 m lower wave length) and thus waves from 2 m to 0.02 m. The authors report a logarithmic fit to their data.

3.3.3 *Spectral tail extrapolation*

Buoys measure the energy spectrum in frequency from 0.05 Hz to 0.5 Hz. Since mean square slope in Equation 3.2 is proportional to the area beneath an Ef^4 spectrum, colocated observations of WSRA mss and buoy mss, which overlap in frequency extent, can be used to infer information about the spectral tail beyond 0.5 Hz. In particular, colocated observations of the difference between WSRA mss and buoy mss (Figure 3.3) can be used to constrain the spectral slope from 0.5 Hz to 2.8 Hz (from 6 m to 0.2 m in deep water).

The difference of the WSRA and buoy mean square slopes is defined as

$$\mathrm{mss}_\delta = \mathrm{mss}_{\mathrm{WSRA}} - \mathrm{mss}_{\mathrm{buoy}} \tag{3.4}$$

where $\mathrm{mss}_{\mathrm{buoy}}$ is the mean square slope from the integrated buoy spectrum, which cover fre-

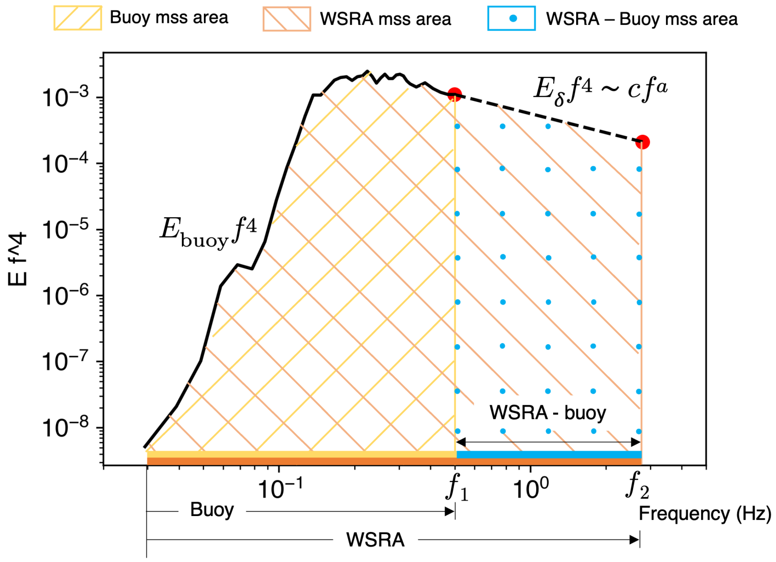

Figure 3.4: Extrapolation of the f^4-compensated buoy spectrum, $E_{\mathrm{buoy}}(f)f^4$, with a compensated tail $E_\delta(f)f^4$ of the form cf^a. When compensated, the area beneath the spectrum is proportional to mean square slope, Equation 3.2. The colored bars and shading represent the frequency and mss extent of the buoy (yellow, hatched), WSRA (orange, hatched), and their difference (blue, stippled).

quencies from ~ 0.05 Hz to 0.5 Hz, and $\mathrm{mss}_{\mathrm{WSRA}}$ is the quasi-specular WSRA mean square slope estimate which is assumed to cover ~ 0.05 Hz to 2.8 Hz.

We seek to extend the buoy spectrum, $E_{\mathrm{buoy}}(f)$, with a spectral tail of the form $E_{\delta}(f) = cf^{n}$ which starts at the end of the buoy spectrum, $f_1 = 0.5$ Hz, and extends to the frequency of the smallest wavelength resolved by the WSRA mss, $f_2 = 2.8$ Hz. Here c is a constant and n is the unknown slope exponent. When f^4-compensated, $E_{\delta}(f)f^4$ has the form cf^a where $a = n + 4$ (Figure 3.4). The integral of cf^a should be equal to the area determined by the mean square slope in Equation 3.2,

$$\int_{f_1}^{f_2} cf^a df = \frac{c}{a+1}\left(f_2^{a+1} - f_1^{a+1}\right) = \frac{g^2}{(2\pi)^4}\mathrm{mss}_{\delta} \tag{3.5}$$

Since the spectrum must be continuous at f_1, then

$$E(f_1)f_1^4 = cf_1^a \tag{3.6}$$

such that

$$c = E(f_1)f_1^{(4-a)} \tag{3.7}$$

Inserting (3.7) into (3.5) results in an equation with one unknown, the exponent a, which can be determined by root-finding:

$$\frac{E(f_1)}{a+1}f_1^{(4-a)}\left(f_2^{a+1} - f_1^{a+1}\right) - \frac{g^2}{(2\pi)^4}\mathrm{mss}_{\delta} = 0 \tag{3.8}$$

Once a is found, the form of the regular energy spectrum over this frequency extent is then

$$E_{\delta}(f) = cf^n \tag{3.9}$$

where $n = a - 4$.

This method was applied to 21 sets of colocated WSRA and buoy observations. Since the WSRA reports mss every minute, all mss observations within a buoy reporting window are used to obtain $\mathrm{mss}_{\mathrm{WSRA}}$. The inferred tail slopes range from $n = -4.1$ to $n = -5.8$, with a mean of

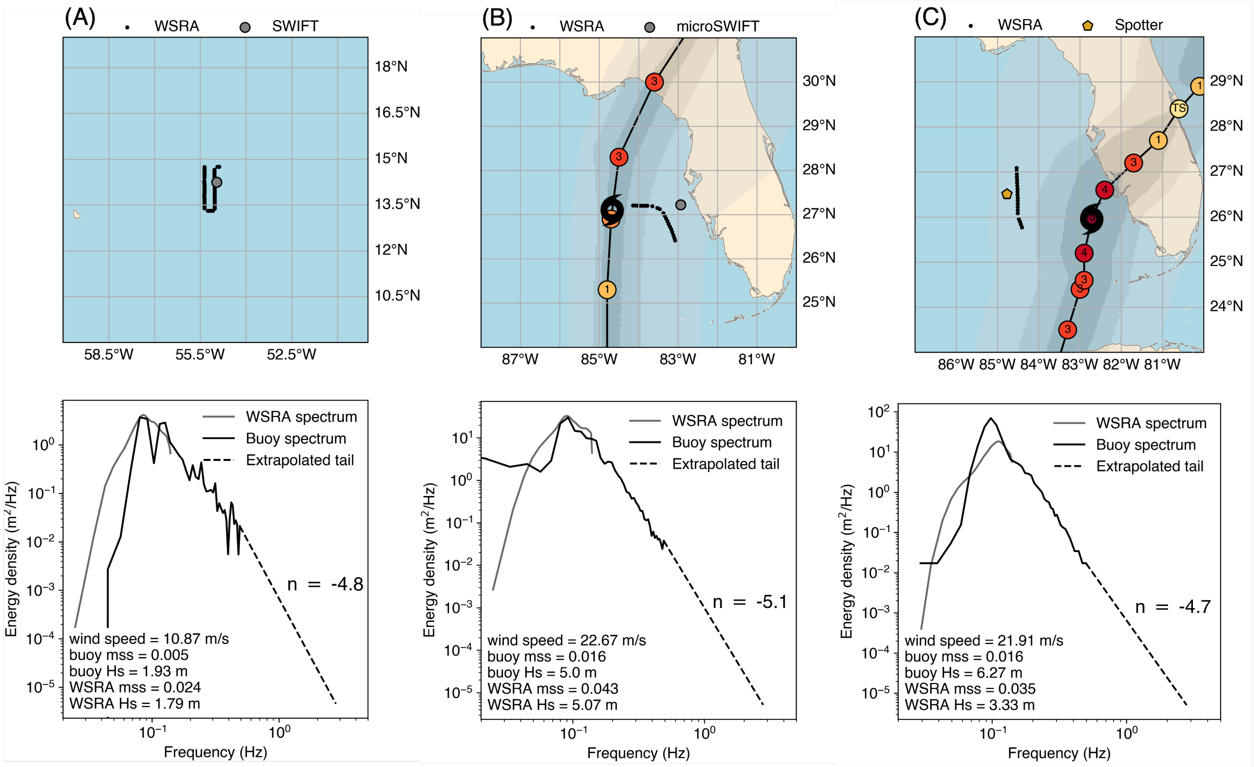

Figure 3.5: Slope extrapolation example cases from ATOMIC (A), Hurricane Idalia (B), and Hurricane Ian (C). For each case, the top panels show the WSRA and buoy locations and the bottom panels show the spectra and extrapolated tails. The dashed line represents the $E_\delta(f)$ tail and n corresponds to the inferred spectral slope exponent in cf^n.

$n = -4.8$ and a standard deviation of 0.41. Wind speeds vary from 10.5 m s^{-1}to 25.6 m s^{-1}and buoy-measured significant wave heights span 1.9 m to 6.9 m.

Three examples of the tail extrapolation method, using cases from the ATOMIC campaign (2020), Hurricane Idalia (2023), and Hurricane Ian (2022), are shown in Figure 3.5. The ATOMIC case (Figure 3.5A) is in moderate conditions with a mean wind speed of 10.9 m s^{-1}and a buoy-measured significant wave height of 1.93 m. The largest separation distance is 22.14 km, and half of the WSRA flight track is directly over the SWIFT. The 1-D WSRA frequency spectrum, derived from the 2D wavenumber spectrum using the Jacobian to convert wavenumber space to frequency-direction space (e.g., Barstow et al. (2005)), is shown for comparison. The WSRA spectrum is only resolved from 0.025 Hz to 0.14 Hz (2500 m to 80 m), but has similar energy levels and captures the main peak. The significant wave height reported by the WSRA is 1.79 m, slightly less than that of the buoy.

The Ian and Idalia cases (Figure 3.5B-C) are characterized by higher wind speeds (22.7 m $s^{-1}$and 21.9 m s^{-1}, respectively) and more energetic sea states (buoy significant wave heights of 5.0 m and 6.3 m). There is good agreement in the shape and energy levels of the 1D spectra and significant wave height between WSRA (5.1 m) and the microSWIFT buoy (5.0 m) in the Ian case. The mean distance between the observations is 68.64 km. In the Idalia case, however, the WSRA spectrum has lower overall energy levels and a higher peak frequency than the Spotter buoy. The WSRA-reported significant wave height (3.3 m) is nearly half that of the buoy (6.3 m). The mean separation distance, 51.49 km, is lower than in Ian.

3.4 Discussion and Conclusions

The saturation of WSRA mean square slope (wavelengths > 0.2 m) with wind speed in hurricanes is consistent with the behavior of buoys (> 6 m) (Figures 3.2 and 3.3) (Davis et al., 2023b). The wind speed at which the WSRA mean square slopes saturate is higher than that of the buoys (approximately 25-30 m s^{-1}compared to 20 m s^{-1}) which may be due to the evolution of the intermediate wavelengths (6 m to 0.2 m) resolved by the WSRA but not the buoy.

The mss of these intermediate wavelengths is represented by the difference of the WSRA mss and buoy mss which also ceases to increase beyond 25 m s^{-1}(Figure 3.3). The data are in general agreement with a set of similar measurements from Vandemark et al. (2004) which are described by a logarithmic wind speed dependence below 18 m s^{-1}. This suggests it is not only the mss of the larger waves that saturate at the extreme wind speeds found in hurricanes. Following the interpretation of mean square slope as a measure of surface roughness, the saturation and roll-off captured in both the WSRA mss and in the difference between the WSRA mss and buoy mss is consistent with the qualitatively similar behavior of the sea surface roughness length first observed by (Powell et al., 2003). The WSRA mss, however, contains slope information that may be relevant to both form and viscous components of the drag.

The mean square slope of the intermediate waves can be used to extrapolate the tail of the buoy spectrum by inferring a constant spectral slope over the frequencies 0.5 Hz to 2.8 Hz. When the equilibrium-to-saturation transition frequency is higher than 0.5 Hz, the constant spectral shape assumption does not hold. However the transition frequency decreases with increasing wind speed (Lenain et al., 2019; Vincent et al., 2019) and is consistently lower than 0.5 Hz beyond 12 m s^{-1}in the data of Vincent et al. (2019).

The mean spectral slope ($n = -4.8$) from 21 colocated WSRA-buoy pairs (within 100 km and 90 minutes), as well as the examples from ATOMIC ($n = -4.8$), Idalia ($n = -5.1$), and Ian ($n = -4.7$) are all close to the canonical f^{-5} tail anticipated at these frequencies. In the ATOMIC case, there is generally good agreement between the energy levels of the WSRA and buoy 1D WSRA frequency spectra as well as between the reported significant wave heights (Figure 3.5A). However the ATOMIC wave conditions were sometimes characterized by two separate wave systems (swell from the north and wind sea from the east), and it appears the higher frequency peak was not captured by WSRA. Good agreement is also observed in the Idalia case, though the wind speed and significant wave height are much higher (22.7 m $s^{-1}$and 5 m, respectively) (Figure 3.5B).

There is substantial disagreement between WSRA and buoys in the Ian example (Figure 3.5C). The WSRA misses the peak and has far lower energy levels, reporting a significant wave height of only 3.3 m relative to the 6.3 m reported by the buoy. The latter is much more typical of hurricane waves, and it is unlikely the observations are close enough to the hurricane eye for a gradient this large to be realistic (Tamizi and Young, 2020). Further, the WSRA observations are also closer to the hurricane than the buoy. Still, the WSRA mss (0.035) is comparable to the other two cases and is close to being within a standard deviation of the observations shown in Figure 3.2. The WSRA mss estimate from the backscatter is upstream of the spectral estimate in the WSRA processing pipeline and does not require correction for the skewing effect caused by the waves during altimetry (PopStefanija et al., 2021). This suggests the WSRA mss, and thus the spectral tail extrapolation method, may still yield reasonable values even when wave height estimates are inaccurate.

Despite good agreement with the canonical result, several sources of uncertainty remain. The exact lower and upper wavenumber limits of the WRSA mss, and whether they may be evolving with wind speed (e.g. Hauser et al., 2008), are not well-known. Uncertainty may be narrowed through more careful examination of raw backscatter data to determine the diffraction limit (upper wavenumber), as was done in Jackson et al. (1992). Errors are introduced by separation in space and time, as hurricane sea states can have large spatial gradients, and the mss response time can be well under an hour (Chen et al., 2016). This motivates more carefully colocated wave buoys and airborne WSRA in future hurricanes.

With reduced error, this method can be used to understand the evolution of the spectral tail in high winds, and its dependence on factors such as storm size, speed, and strength. A better-parameterized tail will enable more accurate predictions of stress in models which require a prescribed tail (Reichl et al., 2014; Chen et al., 2020b).

Data Availability

Wide Swath Radar Altimeter data can be accessed from `https://www.prosensing.com/wsra-level-4-data` and the accompanying met data can be downloaded from `https://seb.noaa.gov/pub/acdata/2023/MET/`. Spotter and microSWIFT data from Hurricane Ian are available at `https://orcid.org/0000-0001-8623-2141`. SWIFT data from ATOMIC are at `https://doi.org/10.5194/essd-13-3281-2021` (Pincus et al., 2021) and WSRA data are at `https://doi.org/10.5194/essd-13-1759-2021` (Quinn et al., 2020). A master archive of microSWIFT data, which contains data from additional hurricanes, is at `https://datadryad.org/stash/dataset/doi:10.5061/dryad.jdfn2z3j1`.

Acknowledgment

This work was funded by the U.S. Office of Naval Research and the U.S. National Ocean Partnership Program (NOPP) as part of the NOPP Coastal Hurricane Impacts project. Air-support was provided by the Naval Research Laboratory's Scientific Deployment Squadron (VXS-1).

The authors thank APL-UW engineers Alex de Klerk, Phil Bush, Emily Iseley, and Joe Talbert for preparation and maintenance of SWIFT and microSWIFT buoys in the ATOMIC and NOPP Hurricane Coastal Impacts projects. Spotter data was provided by Sofar Ocean.

This material is based upon work supported by the National Science Foundation Graduate Research Fellowship Program under Grant No. DGE-2140004. Any opinions, findings, and conclusions or recommendations expressed in this material are those of the author(s) and do not necessarily reflect the views of the National Science Foundation.

Chapter 4

OCEAN SURFACE WAVE SLOPES AND WIND-WAVE ALIGNMENT OBSERVED IN HURRICANE IDALIA

Abstract: *Drifting buoy observations in Hurricane Idalia (2023) are used to investigate the dependence of ocean surface wave mean square slope on wind, wave, and storm characteristics. Mean square slope has a primary dependence on wind speed that is linear at low-to-moderate wind speeds and approaches saturation at high wind speeds (> 20 m* s^{-1}*). Inside Hurricane Idalia, buoy-measured mean square slopes have a secondary dependence on wind-wave alignment: at a given wind speed, slopes are higher where wind and waves are aligned compared to where wind and waves are crossing. At moderate wind speeds, differences in mean square slope between aligned and crossing conditions can vary 15% to 20% relative to their mean. These changes in wave slopes may be related to the reported dependence of air-sea drag coefficients on wind-wave alignment.*

4.1 Introduction

Hurricane-generated ocean surface waves drive the exchange of heat and momentum at the air-sea interface and also contribute to coastal flooding and erosion. A major mechanism by which waves influence these processes is through the modulation of air-sea drag. While wind stress generally increases with wind speed, the rate at which it increases, often described by an air-sea drag coefficient, is complex and under continued investigation. Growing evidence suggests the air-sea drag coefficient depends on sea state through wave age (Janssen, 1989; Toba et al., 1990; Drennan et al., 2003; Edson et al., 2013), wave slope (Taylor and Yelland, 2001; Edson et al., 2013), and more recently, wind-wave alignment (Holthuijsen et al., 2012; Zhou et al., 2022; Potter et al., 2022; Chen et al., 2022; Husain et al., 2022; Manzella et al., 2024). This is critical in hurricanes, since the drag coefficient parameterization used in forecast models influences the simulated intensity of a hurricane (Emanuel, 2003; Davis et al., 2008).

Inside a hurricane, waves are complex and spatially varying. Characteristics such as wave height and direction are asymmetric with respect to the center, and wave growth depends on the size, strength, and translational speed of a storm (Young, 2003). The largest waves are typically found on the right side of the hurricane with respect to the direction of translation (in the Northern Hemisphere), where the storm and the winds are moving in the same direction as the waves while they are being generated (Wright et al., 2001; Hu and Chen, 2011; Collins et al., 2018b; Tamizi and Young, 2020). On the right side of the storm, general alignment of the hurricane's motion and winds results in an "extended" (or "moving") fetch, whereby the waves traveling in the same direction as the storm remain in the wind for an extended period of time (King and Shemdin, 1978).

Swell generally propagates outward from the storm center in an "arc" spanning the right-front, left-front, and left-rear quadrants (King and Shemdin, 1978). The alignment of wind and long period waves (which eventually become swell) within hurricanes, or *wind-wave alignment*, is the subject of some of the earliest research on hurricane waves (Tannehill, 1936; Arakawa, 1954). Misalignment is typically observed on the left half of the storm, and it is often reported to be greater in the left-rear quadrant (Tannehill, 1936; Black et al., 2007; Hu and Chen, 2011; Tamizi and Young, 2020; Schönau et al., 2024). Outward wave propagation in the front of the storm frequently causes slight misalignment to occur in the right-front quadrant (King and Shemdin, 1978; Hu and Chen, 2011). Most studies report the closest wind-wave alignment in the right-rear quadrant, with some suggesting this is due to the sea state in this quadrant being mostly comprised of locally generated waves, and not previously generated swell which has propagated from another region of the storm (Arakawa, 1954; Young, 2006; Hu and Chen, 2011; Hwang et al., 2017; Collins et al., 2018b; Tamizi and Young, 2020). Notable exceptions exist, with some observations showing alignment to the right-front of the storm and crossing, disorganized wind-waves to the right-rear (Holthuijsen et al., 2012; Schönau et al., 2024). The alignment of mean wind direction and dominant wave direction has been shown to have a sinusoidal dependence on azimuth (Hwang et al., 2017; Kudryavtsev et al., 2021).

One dimensional (i.e., scalar wave energy) frequency spectra inside hurricanes are typically unimodal, but can be bimodal (or even trimodal), particularly on the left side where wind-sea and longer period waves propagate in different directions (Doyle, 2002; Young, 2006; Hu and Chen, 2011; Hwang et al., 2017; Tamizi and Young, 2020; Hsu, 2021b). The high frequency tail of observed hurricane spectra span the range of canonical shapes: in a typical spectrum, the energy just beyond the spectral peak is expected to decay as the frequency power-law f^{-4} characteristic of the equilibrium range (wind input balanced by dissipation from breaking and nonlinear energy fluxes) (Toba, 1973; Phillips, 1985). Beyond this range, the spectrum transitions to an f^{-5} saturation range (wind input is balanced by dissipation from breaking) until frequencies approach those of gravity-capillary and capillary waves (Forristall, 1981; Banner, 1990; Romero et al., 2012; Lenain and Melville, 2017). Tamizi and Young (2020) fit their hurricane wave observations from buoys to a generalized Joint North Sea Wave Project (JONSWAP) spectral model and find the spectral tail steepens from f^{-4} to f^{-5} with decreasing wave age, where wave age is the ratio of wave phase speed to wind speed. The mean of their slope exponent observations is -4.68. Drifting buoy observations suggest the tail becomes dominated by the f^{-5} saturation range above wind speeds of 25 m s^{-1} at frequencies spanning from the peak frequency to the maximum resolved frequency of 0.5 Hz (Davis et al., 2023b). Hwang et al. (2017) find substantial scatter in their observed spectral slopes (between -4 and -5), and instead suggest the treatment of the spectral slope exponent as a random variable. The Gaussian fit to their data has a mean of -4.48 and standard deviation of 0.53.

Mean square slope (mss) is an integral quantity closely related to the shape and total energy of the spectral tail. It is frequently used as an integral metric for model spectral comparisons (Elfouhaily et al., 1997; Reichl et al., 2014; Romero and Lubana, 2022). When calculated from the wave spectrum, mss is the second moment in the wavenumber domain:

$$\mathrm{mss} = \int_{k_1}^{k_2} k^2 E(k) dk \tag{4.1}$$

where $E(k)$ is elevation variance spectral density as a function of wavenumber, k, which is integrated over limits k_1 and k_2. With energy proportional to wave amplitude, a, squared, as $E(k) \sim a^2$, Equation 4.1 yields an expression proportional to wave slope characterized by the product of amplitude and wavenumber squared, $(ak)^2$. Buoys (and other point measurements) measure energy in the frequency domain, $E(f)$, thus mss estimates rely on the dispersion relationship to relate frequency to wavenumber:

$$(2\pi f)^2 = gk \tanh{(kh)} \tag{4.2}$$

where g is the acceleration of gravity and h is water depth. The quantity kh is the relative depth, which determines the effect of depth on wave properties. Equation 4.2 can be used in all water depths and is valid in the reference frame intrinsic to the waves (see Section 4.2.4). Energy spectra also need to be transformed from the frequency domain to the wavenumber domain using

$$E(k) = E(f)\frac{df}{dk} \tag{4.3}$$

where $df/dk = c_g/(2\pi)$ is a Jacobian proportional to group velocity, c_g, calculated using wavenumber and depth (Holthuijsen, 2007). An explicit expression for mss can also be derived by substituting the deep water limit of the dispersion relation, $k = (2\pi f)^2/g$, into Equation 4.1. The k^2 dependence of Equation 4.1 yields an f^4 dependence in the frequency domain.

The magnitude of mss is sensitive to wavelength (or frequency) extent, thus the magnitude varies widely across instruments. Optical methods, such as the sun glint measurements of Cox and Munk (1954), lidar (Lenain et al., 2019), or polarimetry (Zappa et al., 2008), approach estimates of the "total" mean square slope. (Despite broad wavelength coverage, the long and short wavelength limits of mss estimates from these methods are constrained by field of view and pixel resolution, respectively.) A total mean square slope is equivalent to Equation 4.1 integrated from $k_1 \simeq 0$ rad m^{-1} to $k_2 \simeq \infty$.

Other methods which resolve mss over a shorter range of wavelengths, such as buoys (Davis et al., 2023b) and radar (Gleason et al., 2018), have smaller mss. The k^2 dependence of Equation 4.1 weights the tail of the spectrum which contains the high frequency, short wavelength waves. At low-to-moderate wind speeds and wave conditions, a substantial portion of the total mean square slope magnitude is contributed by short waves typically not measurable by buoy and radar (Lenain and Melville, 2017).

Mean square slope, mss, has a primary dependence on wind speed. Most observations suggest mss, resolved down to wavelengths ranging from several meters to less than a centimeter, has an approximately linear relationship to wind speed up to 15-20 m s^{-1} (Cox and Munk, 1954; Jackson et al., 1992; Bréon and Henriot, 2006; Lenain et al., 2019; Guérin et al., 2022; Davis et al., 2024a). Other observations have found logarithmic (Wu, 1990; Walsh et al., 1998; Vandemark et al., 2004; Ross and Dion, 2007) or power-law (Hauser et al., 2008; Chen et al., 2018) relationships over similar wavelengths and wind speeds.

In hurricanes, mss approaches quasi-saturation at high wind speeds as measured by buoys (Davis et al., 2023b; Shimura et al., 2024) and radar (Katzberg et al., 2013; Gleason et al., 2018; Hwang et al., 2021; Davis et al., 2024a). L-band GPS reflectometry measurements in hurricanes (0.57 m minimum wavelength) have a logarithmic dependence on wind speed and increase little with growing wind speed beyond 25 m s^{-1} (Hwang et al., 2021). Buoy-based mss estimates (6 m minimum wavelength) measured in hurricanes effectively saturate beyond 25 m s^{-1} and can be described using a tanh relationship up to 54 m s^{-1} (Davis et al., 2023b). Mean square slopes estimated by the Wide Swath Radar Altimeter (WSRA), a Ku-band radar which flies aboard the "Hurricane Hunter" P-3s (0.2 m minimum wavelength), are linear up to 20 m s^{-1}, saturate around 25 m s^{-1}, and even reduce slightly at higher wind speeds (Walsh et al., 2014; PopStefanija et al., 2021; Davis et al., 2024a).

Mean square slope has been shown to have a secondary dependence (variation at a given wind speed) on atmospheric stability. Hwang and Shemdin (1988) find slopes are lower in stable conditions, which was also supported by subsequent laser glint measurements (Shaw and Churnside, 1997). Lenain et al. (2019) were unable to find an mss dependence on atmospheric stability using the Richardson number, though their observations mostly consisted of neutral to unstable conditions. Other works have reported a dependence on fetch (Vandemark et al., 2004; Donelan, 2018), however the modeled mss of Donelan (2018) suggest this dependence is weak until wind speeds exceed 30 m s^{-1}, beyond which the influence of fetch varies. Vandemark et al.

(2004) find mss of waves longer than 2-m measured near the coast to be smaller than in the open ocean, which Sun et al. (2001) had previously attributed to energy transfer from short to long waves via wave-wave interaction. Close to shore (within 2 km), mss first increases due to shoaling and then decreases drastically due to active breaking in the surf zone (Anctil and Donelan, 1996; Sun et al., 2001). In hurricanes, Hwang and Fan (2018) report that their parametric model of mss (based on observations) has a secondary dependence on wind field asymmetry, varying 10–15% at a given wind speed and generally increasing as asymmetry grows. Their mss has a weak secondary dependence on the radius of maximum wind.

The spectral tail, which can be characterized by mss, is closely tied to wind forcing. Within the f^{-4} equilibrium range, the wind friction velocity is proportional to mss (Plant, 1982; Phillips, 1985). Wave-derived wind stress estimates compare well to direct covariance flux observations in wind speeds from 5 m s^{-1} to 15 m s^{-1} (Thomson et al., 2013). Energy levels in the equilibrium range can be used to derive proxy wind speeds from measurements of the wave spectrum (Voermans et al., 2020; Shimura et al., 2022; Mudd et al., 2024). The empirical relationship between mss and wind speed is frequently used to infer wind speed using satellite mss observations (Clarizia and Ruf, 2016; Hauser et al., 2017; Gleason et al., 2018) as well as surface buoy mss observations (Zhong et al., 2022).

When resolved down to sufficiently small wavelengths, mss is widely interpreted as a measure of roughness (Cox and Munk, 1954; Walsh et al., 1998; Hwang, 2005; Boisot et al., 2015; Li et al., 2022). The air-sea drag coefficient, which sets the rate of momentum transfer between the atmosphere and ocean, is often expressed as a function of a roughness length (Charnock, 1955; Edson et al., 2013). Root mean square slope, $\sqrt{\mathrm{mss}}$, has previously been used to develop a roughness length parameterization at moderate conditions in the coastal waters of Lake Ontario (Anctil and Donelan, 1996). A similar form was adopted by Taylor and Yelland (2001) in their widely used roughness length parameterization, but with $\sqrt{\mathrm{mss}}$ replaced by a bulk slope calculated as the ratio of significant wave height to peak wavelength. Mean square slope also correlates with wave form drag (Sullivan et al., 2018). Theoretical formulations for form drag depend on the shape and energy levels within the spectral tail, both of which are captured by changes in mss (Donelan et al., 2012; Reichl et al., 2014). At high wind speeds, form drag is the dominant contributor to total drag (Donelan et al., 2012; Sullivan et al., 2018; Donelan, 2018).

At the high wind speeds found in hurricanes, many observational drag coefficient estimates begin to saturate around 25 m s^{-1} to 35 m s^{-1} (Powell et al., 2003; Donelan, 2004; Black et al., 2007; Holthuijsen et al., 2012; Takagaki et al., 2012). (The measurements originally presented in Donelan (2004) have since been revised in Curcic and Haus (2020).) The saturation of drag coefficient with wind speed is qualitatively similar to the dependence of mss on wind speed, which is generally monotonic but increases little beyond 25 m s^{-1} (Davis et al., 2023b). The observations of Powell et al. (2003) and Holthuijsen et al. (2012) suggest drag coefficient reduces at high wind speeds ($>$ 35 m s^{-1}), however more recent studies have raised concerns about substantial uncertainty and bias inherent to the dropsonde profile methods used to estimate surface stress in these prior works (Richter et al., 2016, 2021).

Recent work has demonstrated a dependence of drag coefficient on wind-wave alignment inside hurricanes. Holthuijsen et al. (2012) find that drag coefficient, estimated from GPS dropsonde hurricane wind profiles, is reduced when wind and long-period wave directions are crossing below wind speeds of 25 m s^{-1}, but is significantly enhanced from 30 m s^{-1} to 50 m s^{-1} (relative to aligned and opposing wind and waves). Zhou et al. (2022) estimate drag coefficients in hurricanes using a combination of upper-ocean current observations and a coupled ocean–wave model. They report a significant reduction in drag coefficient above 25 m s^{-1} when wind-wave alignment exceeds 45 degrees. Large eddy simulations of monochromatic waves, with a wave age characteristic of tropical cyclones, suggest drag coefficient is reduced when wind-wave alignment exceeds 22.5 to 45 degrees (Manzella et al., 2024).

Here, we use wave observations from a densely-populated array of drifting buoys in Hurricane Idalia (2023) to explore the secondary dependencies of mss within hurricanes. Based on the connection of mss to the spectral tail, we hypothesize mss will have a secondary dependence on wind-wave alignment in hurricanes that is similar to that of drag. While a related dataset of wave observations collected in Hurricanes Ian and Fiona (2022) was sufficient to establish a regime change in the primary wind speed dependence of mss, from linear growth to saturation, it was unable to reveal any concrete relationships that explained spread at a given wind speed (Davis et al., 2023b). This was likely due to the sparsity of simultaneous observations on both sides of the storm. Understanding variation in mss at a given wind speed may help to explain changes in the spectral tail and underlying wave field, and thus wave-induced drag within hurricanes. These observations are also useful for wave model validation and improvement within hurricanes (Reichl et al., 2014).

Section 4.2 provides an overview of the conditions within Hurricane Idalia and describes the free-drifting wave buoys used to estimate mss and the forecast model used to estimate 10-m winds. Section 4.3 presents the results, and Section 4.4 connects the results to recent studies related to the dependence of drag coefficient on wind-wave alignment. Section 4.5 concludes.

Buoy observations used in this work fundamentally measure in the frequency domain, whereas mss is a spatial property dependent on k through Equation 4.1. This necessitates switching between wavenumber and frequency domains often throughout the methods, results, and discussion. As a general rule, physics will be described in the wavenumber domain (especially as related to mss) whereas observations will be described in the frequency domain.

4.2 Methods

This section describes wave observations and model-simulated winds in Hurricane Idalia used to study the dependence of mss on wind-wave alignment in a storm-following reference frame. We first provide an overview of wind and wave conditions in Hurricane Idalia and the storm's meteorological characteristics. Next, we describe specifications of the microSWIFT and Spotter buoys and their spectral processing methods, followed by details on buoy mss calculation and a surface drift Doppler adjustment applied to remove the effect of windage on Spotter mss estimates. We then describe the COAMPS-TC model used to produce wind fields and the process of transforming the buoys into a storm-following reference frame based on the model's forecasts and ancillary Best Track data. This section concludes with the definition of wind-wave alignment used throughout the results.

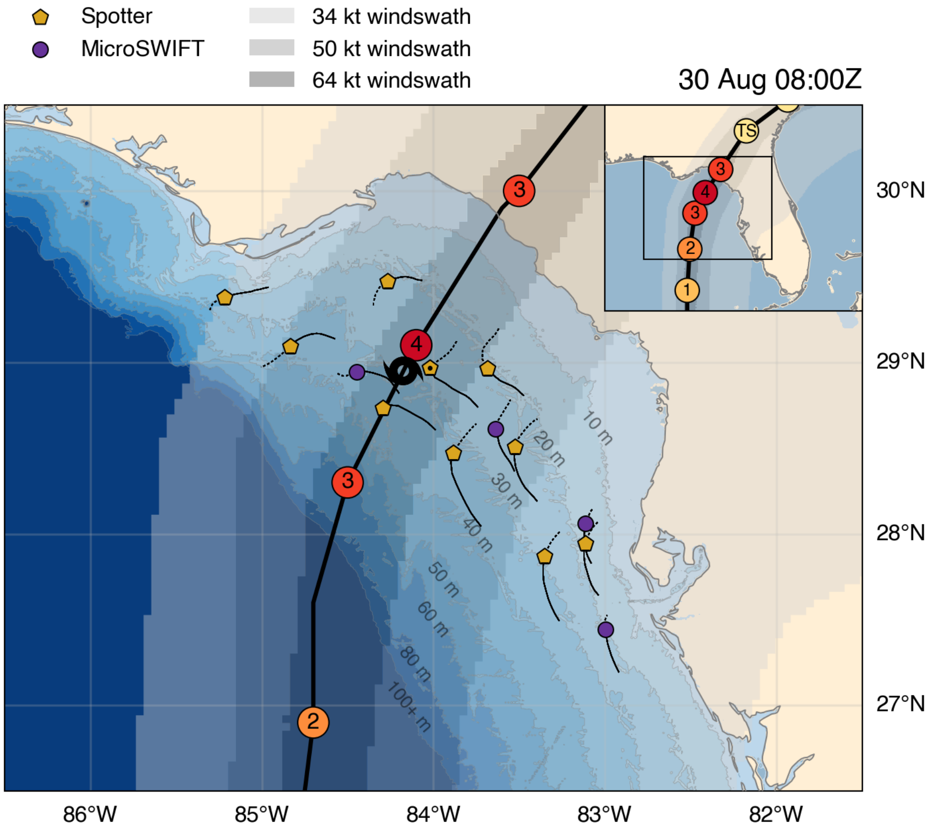

Figure 4.1: Wave buoys in Hurricane Idalia (2023). The hurricane symbol represents Idalia's position at 30 August 0800Z, and markers represent buoy positions at this time. Drift tracks over a 15-hour period on 30 August, used later to produce storm-following visualizations, are shown as thin black lines. Track lines are solid up to the position shown (0000Z to 0800Z) and dashed beyond (0800Z to 1500Z). The Spotter buoy nearest to the storm center (SPOT-30103D), indicated with a dot at its center, is used in the representative time series shown in Figure 4.2. Idalia's intensity on the Saffir-Simpson Hurricane Wind Scale is indicated inside the circles along the track, and shaded regions represent the extent of the 34 knot, 50 knot, and 64 knot wind swaths. Bathymetry contours are constructed from the 2023 GEBCO grid. The inset map in the upper right corner shows Idalia's track in the larger context of the Florida Gulf coast.

4.2.1 Hurricane Idalia

Hurricane Idalia made landfall as a category 4 hurricane in the Florida Big Bend region on August 30, 1145 UTC (Cangialosi and Alaka, 2024). Two days prior, a P-3 aircraft operated by the

U.S. Naval Research Laboratory's Scientific Development Squadron (VXS-1) deployed an array of drifting wave buoys on both sides of the storm's forecasted path (Figure 4.1). At the time of Idalia's closest approach to the buoys, approximately 0800Z on 30 August, the array spanned the Big Bend coastline with most buoys 50 km to 120 km offshore. Water depth along buoy trajectories varied within the 10 m to 40 m depth contours, as indicated by the 2023 General Bathymetric Chart of the Oceans (GEBCO) (GEBCO Bathymetric Compilation Group, 2023). Using a relative depth metric weighted by energetic wavelengths of the spectrum, 53% of observations are in intermediate relative depths ($\pi/10 < kh < \pi$) and 47% are in deep water ($kh \geq \pi$). The maximum significant wave height recorded by the array was 7.5 m at a peak period of 12.8 s, and the maximum COAMPS-TC 10-m wind speed at a buoy's location was 52 m s^{-1} (Figure 4.2a-d).

During the 24-hour period ahead of landfall, Idalia's translation speed increased from 7 to 11 m s^{-1}, radius of maximum wind (RMW) decreased from 28 to 19 km, and max 1-min averaged, 10-m wind speed intensified from 36 to 50 m s^{-1} (Figure 4.2e-g). Storm metrics are from the International Best Track Archive for Climate Stewardship (IBTrACS) (Knapp et al., 2010b; Gahtan et al., 2024). The Kudryavtsev et al. (2021) criterion for wave trapping, or "resonance" between the group velocity and storm translation speed, suggests the storm was too slow to reach resonance on approach to the buoy array until about 06Z on 30 August, beyond which the ratio dropped below unity (faster than resonance) until landfall (Figure 4.2e). The period of time when the trapping criterion crosses through unity coincides with the storm's closest approach to the array.

4.2.2 *Wave measurements*

Surface wave measurements are from two types of free-drifting buoys: the UW-APL microSWIFT and the Sofar Spotter. Both buoys use GPS-derived velocities to estimate hourly records of surface wave statistics in the form of scalar energy spectra, $E(f)$, and directional moments, a_1, b_1, a_2, b_2 (Herbers et al., 2012).

The microSWIFT is a small and expendable wave buoy designed for aerial deployment from the A-sized dropsonde chute of research aircraft (Thomson et al., 2023). The buoy has a 45.7 cm (18 in) long, 8.9 cm (3.5 in) diameter cylindrical hull and a mass of 2.4 kg. A specialized float

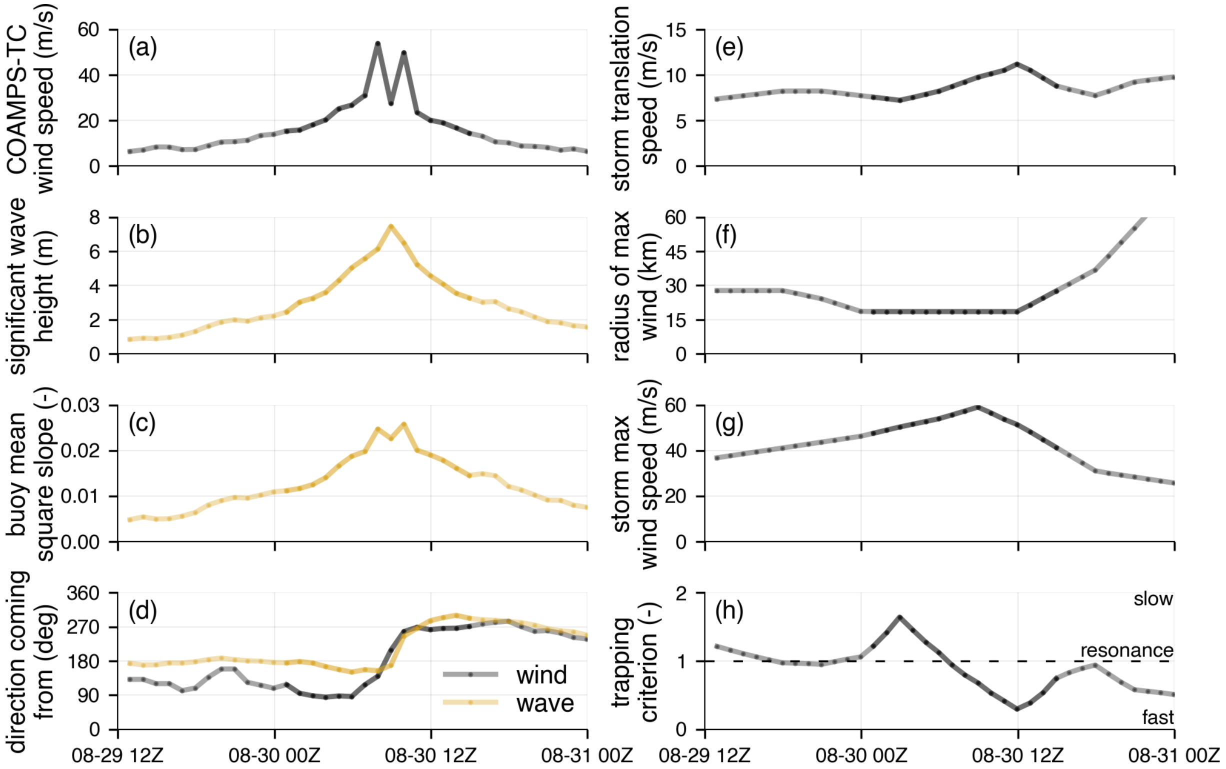

Figure 4.2: Time series of a representative buoy (SPOT-30103D, dotted in Figure 4.1) and Idalia's meteorological metrics over a 36-hour period: (a) COAMPS-TC wind speed; (b) buoy-measured significant wave height; (c) buoy-measured mean square slope; (d) buoy-measured energy-weighted wave direction and COAMPS-TC wind direction (at the buoy's position); (e-g) storm translation speed, radius of maximum wind, and maximum wind speed (all as reported by IBTrACS); and (h) Kudryavtsev et al. (2021) trapping criterion (ratio of dimensionless radius of maximum wind to critical fetch, their Equation 16). Idalia made landfall close to 12Z on 30 August. Wave heights peak as the storm passes closest to buoy. The bold regions correspond to the time period shown in the storm-following reference frame.

collar provides additional buoyancy and hydrodynamic damping. In still water, the hull has 3.5 inches of freeboard. Every hour, GPS velocities are sampled at 5 Hz for 30-minutes and are processed into spectra using 256-s windows with 75% overlap. Each window is high-pass filtered using a cutoff frequency of 0.04 Hz. After band merging every three adjacent frequencies, the spectra have 48 degrees of freedom and span 0.0098 Hz to 0.490 Hz in 42 frequency bins. Wave energy density at the first 39 frequencies is estimated from the horizontal GPS velocities (north-south and east-west components), while the remaining 3 highest frequencies, which span 0.466 Hz to 0.490 Hz, are estimated from the vertical GPS velocities to prevent motion contamination from the buoy's pitch (or roll) natural frequency within these bands. The buoy's heave natural frequency, 0.74 Hz, is above the highest reported frequency. Energy density, directional moments, and the mean geospatial coordinates within the hour are transmitted via Iridium.

The Spotter is a small and versatile solar-powered buoy which is deployed here in a free-drifting format (Raghukumar et al., 2019). Spotters used in this project were specially rigged for air-deployment out of the P-3 aircraft's open door (Dorsay et al., 2023b). The sphere-like hull is 38 cm in diameter with a mass of 5.5 kg. GPS velocities are sampled at 2.5 Hz and are processed into 256-sample FFTs to produce hourly spectra spanning 0.0293 Hz to 0.5 Hz in 38 frequency bins. The spectral estimates have a frequency resolution of $\Delta f = 2.5/256$ Hz up to the 0.33 Hz bin and a coarser, $3\Delta f$ resolution above this frequency to reduce the size of the Iridium message. In addition to wave measurements, Spotter buoys were also equipped with barometers and water temperature sensors. Spotter wave spectra can be used to derive proxy wind observations from the equilibrium range of the tail (Dorsay et al., 2023a), however this method is not used in the current work.

4.2.3 Buoy mean square slope

Mean square slope is estimated using Equations 4.1–4.3 integrated from $k_1 = 0.01$ rad m^{-1} to $k_2 = 1$ rad m^{-1} (wavelengths from 620 m to 6 m). This corresponds to frequencies from 0.05 Hz to 0.5 Hz, in deep water. These frequencies contain the high energy gravity waves and typically include the spectral peak and the start of the tail (in moderate wind conditions). The upper limit of 1 rad m^{-1}, or 0.5 Hz, means waves shorter than 6 m cannot be resolved and included in the mss. Some publications refer to an mss calculated over a truncated frequency range as a "band-pass" or "low-pass filtered" mss (Hwang, 2005; Chen et al., 2016, for example). Buoy-resolved mss is a fraction of total mss at moderate wind speeds (approximately 20% relative to Cox and Munk), but it remains useful as a measure of the steepness and of the shape and energy level of the equilibrium and early saturation ranges captured within the spectral tail at these frequencies (Vincent et al., 2019). The Lagrangian nature of free-drifting buoys also means they measure smoother troughs and sharper crests relative to a fixed Eulerian measurement, since buoys spend more time in wave crests and less time in troughs (Longuet-Higgins, 1986). A Lagrangian-measured mss is reduced relative to an Eulerian-measured mss, though this effect should be order $(ak)^2$ and thus less than 1%.

4.2.4 Surface drift Doppler adjustment

A platform that is moving relative to waves experiences a Doppler shift which causes measurements made in the platform's *observed* reference frame to deviate from the reference frame that is *intrinsic* to the waves (Collins et al., 2017; Colosi et al., 2023; Amador et al., 2023, and references therein). Free-drifting buoys are nearly Lagrangian surface-following platforms, however drift components due to Stokes drift and windage (i.e., wind slip) can cause buoys to move relative to the intrinsic wave reference frame (Iyer et al., 2022). The dispersion relationship used to connect frequency domain to wavenumber domain (Equation 4.2) is valid in the intrinsic reference frame, thus observed spectra are adjusted to the intrinsic frame prior to computing mss (Figure 4.3). For spectral wave measurements made in time, the Doppler shift manifests as a modulation in frequency. Frequencies in the observed reference frame are mapped to frequencies in the the intrinsic reference frame as

$$f_{\mathrm{in}} = f_{\mathrm{ob}} + \frac{Uk\cos(\theta_r)}{2\pi} \tag{4.4}$$

where f_{in} is frequency in the intrinsic reference frame, f_{ob} is frequency in the observed reference frame, k is the magnitude of the wavenumber vector (which is invariant between reference frames), U is the platform's speed, and θ_r is the relative heading of the platform with respect to the waves. After mapping the frequencies, the Jacobian, $df_{\mathrm{ob}}/df_{\mathrm{in}}$, is used to map the observed energy spectrum to the intrinsic reference frame

$$E_{\mathrm{in}}(f_{\mathrm{in}}) = E_{\mathrm{ob}}(f_{\mathrm{ob}})\frac{df_{\mathrm{ob}}}{df_{\mathrm{in}}} \tag{4.5}$$

where E_{in} and E_{ob} are the intrinsic and observed elevation variance spectra, respectively. Equation 4.5 is required to conserve variance and can be estimated using finite differencing (Collins et al., 2017). Following previous Doppler adjustment procedures, the deep water linear dispersion relationship, $f_{\mathrm{in}} = \sqrt{gk}/(2\pi)$, is used with Equation 4.4 to obtain a quadratic equation in k. The observed frequencies are then mapped to intrinsic frequencies considering ambiguities and limits discussed in Collins et al. (2017) and Colosi et al. (2023). The Doppler shift experienced in the observed reference frame is typically largest at high frequencies (high k). While the effect on low-order moments (e.g., significant wave height) can be minimal, differences in high-order moments between observed and intrinsic reference frames can be large.

Spotter drift relative to the surface is due to a small amount of windage (i.e., wind slip) and surface Stokes drift. MicroSWIFTs have minimal wind slip due to their low freeboard, thus any surface-relative drift is assumed to be due to Stokes drift. Spotter wind slip is estimated by comparing to microSWIFT buoys within the dataset, after removing Stokes drift contributions from the mean drift speed derived from hourly GPS fixes for both buoys. Across all wind speeds in the dataset, microSWIFTs have a mean drift-to-wind-speed ratio of 3.0%, which is the rule of thumb for ocean surface drift speed as 3% of the 10-m wind speed (Samelson, 2022). The mean drift-to-wind-speed ratio of the Spotters is 4.2%, which suggests the 1.2% difference is due to wind slip. This is close to the 1% wind slip estimated for the Spotter in Houghton et al. (2021) and the 1.09% mean wind slip for the similar full-sized SWIFT v4 (Iyer et al., 2022). The drift-to-wind-speed ratio for each buoy varies with wind speed, though the 1.2% difference remains nearly constant. Surface Stokes drift is calculated from the spectral integral form for intermediate water depths. The upper frequency of 0.5 Hz may result in an underestimation of the Stokes

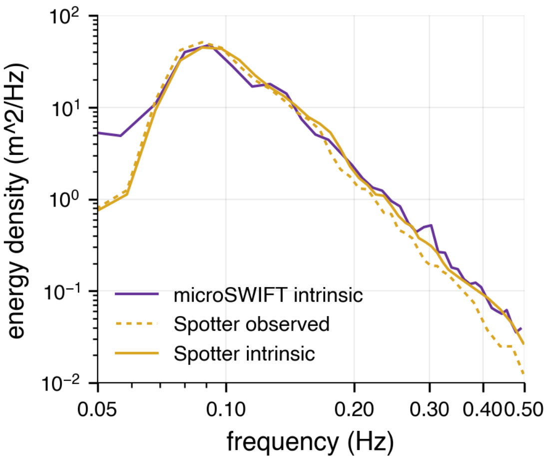

Figure 4.3: Comparison of intrinsic (Doppler shift adjusted) and observed energy spectra in 35 m s^{-1} winds. After adjustment for Doppler shift due to both wind slip and Stokes drift, Spotter mss calculated from the spectra shown here increased by 31%, from 0.016 (observed) to 0.021 (intrinsic). The intrinsic spectrum reported by a nearby (33 km away) microSWIFT, adjusted only for Stokes drift, is shown for comparison. In contrast, microSWIFT mss increased only 10%, from 0.020 (observed, not shown) to 0.022 (intrinsic). At this time instance, the percent difference between the Spotter and microSWIFT slopes reduced from 22% (observed) to 5% (intrinsic).

drift (Lenain and Pizzo, 2020), however contributions from Stokes drifts are minor relative to contributions from windage.

Platform speed relative to the surface, U, is set to the magnitude of the wind slip and surface Stokes drift vector sum. The relative heading of the platform with respect to waves, θ_r in Equation 4.4, is determined using a wave direction estimated from the buoy's directional moments and the surface-relative drift direction

$$\theta_r(f) = \theta_{\text{wave}}(f) - \theta_{\text{drift}} \tag{4.6}$$

here θ_{wave} is a smoothed, frequency-dependent wave direction calculated from energy-weighted directional moments, $a_1(f)$ and $b_1(f)$, in sliding windows of 7 frequency bands. Surface-relative drift direction, θ_{drift}, is set to the direction of the Stokes drift and wind slip vector sum. (The direction of the Stokes drift vector is calculated from buoy directional moments, and the direction of the wind slip vector is the direction of the wind.) This direction is generally aligned with the mean drift estimated from hourly GPS fixes. Both θ_{wave} and θ_{drift} are in the “going to” convention.

The Doppler adjustment procedure relies on the validity of the deep water dispersion limit and the assumption that effects of current shear are minimal. While longer waves in the spectrum are in intermediate water depths for more than half of the observations in the dataset, all observations have an mss-weighted relative depth that indicates shorter waves are in deep water. These correspond to the high frequencies which determine mss and are subject to the largest Doppler shift, such that the deep water assumption remains valid. These short waves have a small vertical distribution of wave motion such that they effectively experience surface currents (Zippel and Thomson, 2017).

4.2.5 COAMPS-TC surface winds

Surface wind estimates are from real-time operational forecasts of Hurricane Idalia made by the U.S. Naval Research Laboratory’s (NRL) Coupled Ocean-Atmosphere Mesoscale Prediction System for Tropical Cyclones (COAMPS-TC) (Doyle et al., 2012, 2014). Real-time COAMPS-TC forecasts use a nested grid system with initial and boundary conditions from the NOAA Global Forecast System (GFS). When initial storm intensity is greater than 28.3 m s^{-1} (55 knots), the initial horizontal wind structure is generated from a modified Rankine wind vortex based on physical and synthetic observations from the National Hurricane Center. Below this intensity, the initial vortex is downscaled from the NOAA GFS analysis.

Surface winds (10-m reference height) from the inner-most 4-km grid are aggregated from sequential short-range real-time operational forecasts to produce “reforecast” wind fields. The first hour of each forecast is omitted to minimize the effect of model state adjustments that occur early in each forecast. Lead times of successive forecasts span 1 to 6 hours. Reforecast fields are adjusted from original operational forecast fields such that the maximum 10-m wind speed matches the NHC final Best Track intensity and the minimum sea-level pressure matches the NHC final Best Track minimum sea-level pressure. Surface winds, output every 15 minutes starting at the top of each hour, are interpolated onto wave buoy observations using bilinear interpolation in space and time.

Hurricane Idalia COAMPS-TC wind speeds are validated using Stepped Frequency Microwave Radiometer (SFMR) observations collected from 29 August to 30 August. The distribution of COAMPS-TC wind speed errors, created from $n = 1,289$ comparisons, has an estimated bias of 2 m s^{-1} and an error of 6 m s^{-1} over all wind speeds (see Appendix B). This error is nearly equivalent to the 7 m s^{-1} uncertainty used previously in Davis et al. (2023b), estimated by comparing COAMPS-TC 6-hr intensity errors to the National Hurricane Center Best Track re-analysis across hundreds of major hurricane forecasts. Error grows as approximately 22% of wind speed. There is no discernible bias across storm quadrants.

COAMPS-TC wind direction is compared with observations from National Data Buoy Center (NDBC) Station 42036 moored at (28.501 N, 84.508 W). Station 42036 was approximately 10 km from Idalia's center on 30 August 06Z. COAMPS-TC wind direction is estimated to have a bias of -6 degrees and an error of 19 degrees, as estimated from a distribution of wind direction differences created from $n = 282$ comparisons to 10-minute observations over 29 August 00Z to 31 August 00Z (see Appendix B). The validation of COAMPS-TC Wind speed and direction against SFMR and NDBC Station 42036 is described further in Appendix B.

4.2.6 Storm-following reference frame

The density of buoys in the Hurricane Idalia dataset enables visualization of wave measurements in a storm-following reference frame (Schönau et al., 2024, for example). To transform observations into the storm-following reference frame, the hourly position of each buoy relative to the storm center was determined using Best Track storm positions from IBTrACS. Storm positions (reported every 3 hours) were interpolated onto buoy observation times and used to compute northings and eastings relative to the storm center.

During some hours, the COAMPS-TC reforecast track (as determined by the minimum pressure) deviated from the Best Track. Since interpolation of 10-m wind speed at buoy observations close to the storm center is sensitive to errors in track, COAMPS-TC longitude-latitude grids were reprojected onto an x-y grid (centered on the storm and measured in meters) using a transverse Mercator projection. The position of each buoy relative to the IBTrACS Best Track was then translated onto this grid, and translated positions (now relative to COAMPS-TC) were used to extract 10-m wind vectors from the model x-y grid. The buoys were sufficiently offshore such that this adjustment did not translate any of them onto land, which would result in an inaccurate wind speed.

4.2.7 *Definition of wind-wave alignment*

Directional alignment between wind and waves (wind-wave alignment) is calculated using COAMPS-TC 10-m wind direction and bulk wave direction measured by the buoys. A goal of this work is to understand the influence of longer, energetic waves on mss. Wind-wave alignment is thus calculated using an energy-weighted wave direction from the buoy's energy-weighted directional moments (Kuik et al., 1988)

$$\theta_{\text{wave}} = \left(270^\circ - \frac{180^\circ}{\pi}\text{arctan2}(\overline{b}_1, \overline{a}_1)\right) \mod 360^\circ \tag{4.7}$$

where

$$\overline{a}_1 = \frac{\int a_1(f)E(f)df}{\int E(f)df} \qquad \overline{b}_1 = \frac{\int b_1(f)E(f)df}{\int E(f)df} \tag{4.8}$$

and $a_1(f)$ and $b_1(f)$ are the first two directional moments which represent wave motion along the N-S and E-W principle axes at each frequency, respectively (Thomson et al., 2018, Appendix). An energy-weighted direction characterizes a similar region of the spectrum as peak direction, but it is more stable in cases when there is not a well-defined peak, or when there are multiple peaks. Wind-wave alignment is defined here as the smallest angle resulting from a difference between the wind and wave directions

$$\Delta\theta = \begin{cases} \theta_{\text{wind}} - \theta_{\text{wave}}, & \text{if } -180^\circ \leq \theta_{\text{wind}} - \theta_{\text{wave}} \leq 180^\circ \\ \theta_{\text{wind}} - \theta_{\text{wave}} - 360^\circ, & \text{if } \theta_{\text{wind}} - \theta_{\text{wave}} > 180^\circ \\ \theta_{\text{wind}} - \theta_{\text{wave}} + 360^\circ, & \text{if } \theta_{\text{wind}} - \theta_{\text{wave}} < -180^\circ \end{cases} \tag{4.9}$$

or more concisely as

$$\Delta\theta = (\theta_{\text{wind}} - \theta_{\text{wave}} + 180^\circ \mod 360^\circ) - 180^\circ \tag{4.10}$$

where θ_{wind} and θ_{wave} are in the “going to” convention and mod is the modulo operation. This definition ensures, for example, that wind heading towards 0° (north) and waves heading to 270° (west) results in an alignment of 90° and not −270°. Signed wind-wave alignment is $\in [-180^\circ, 180^\circ]$. Wind-wave alignment can also be thought of as the wave heading relative to wind direction.

4.3 Results

4.3.1 Spatial distribution of wind and waves

Observations from the array over a 15-hour period, from 00:00Z to 15:00Z on 30 August, are transformed into a storm-following reference frame to visualize their spatial distribution within Idalia (this time period is emboldened in Figure 4.2). Buoy positions (1-hour apart) are normalized by the storm’s radius of maximum wind, which is nearly constant at 18.5 km (10 nmi) over the period (Figure 4.2f). The 34-knot and 50-knot 10-m wind speed swaths, as indicated by COAMPS-TC and the Best Track wind radii, extend further to the right side of the storm (Figure 4.4a). Buoy-measured mss is generally highest closest to the storm center due to the dependence of mss on wind speed (Figure 4.4b).

The absolute wind-wave alignment ($|\Delta\theta| \in [0^\circ, 180^\circ]$) is smallest to the right and rear of the storm’s center (Figure 4.4c). Wind and waves are less aligned towards the right-front, and are

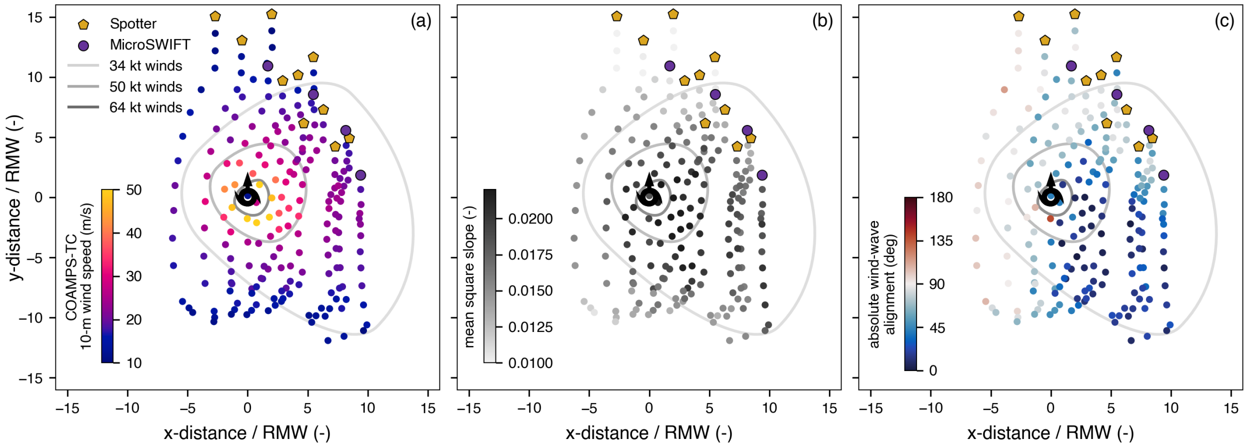

Figure 4.4: (a) COAMPS-TC 10-m wind speed, (b) mean square slope, and (c) absolute wind-wave alignment in a storm-following reference frame over a 15-hour period in Hurricane Idalia (2023). The initial position of each buoy is indicated by the markers with subsequent observations each spaced an hour apart. The storm center (minimum pressure) is at $(0, 0)$, and the storm heading is always in the direction of the y-axis (up). All distances are normalized by the radius of maximum wind (RMW) at each observation time. The concentric rings provide a visualization of the spatial structure of the storm and represent the approximate extent of 34 knot (17.5 m s^{-1}) tropical storm force, 50 knot (25.7 m s^{-1}) storm force, and 64 knot (32.9 m s^{-1}) hurricane force winds from the NHC Best Track. The rings are drawn by connecting the radii at each wind speed (reported for each quadrant and averaged over the 15 hour period) with arcs.

the least aligned on the left side of the storm, with most observations on the left side spanning 90° to 135° alignment. Wind-wave alignment can be categorized using definitions proposed by Holthuijsen et al. (2012) and used to describe regions in which long period waves and locally-generated short period waves, and thus the wind direction, are *aligned*, *crossing*, or *opposing*:

- *aligned*: long period waves traveling within 45° of the wind; $|\Delta\theta| \in [0^\circ, 45^\circ]$

- *crossing*: long period waves traveling within 45° from the normal to the wind; $|\Delta\theta| \in (45^\circ, 135^\circ]$

- *opposing*: long period waves traveling within 45° from the opposing wind direction; $|\Delta\theta| \in (135^\circ, 180^\circ]$

(Note that “aligned” has been renamed from its original category, “following”.)

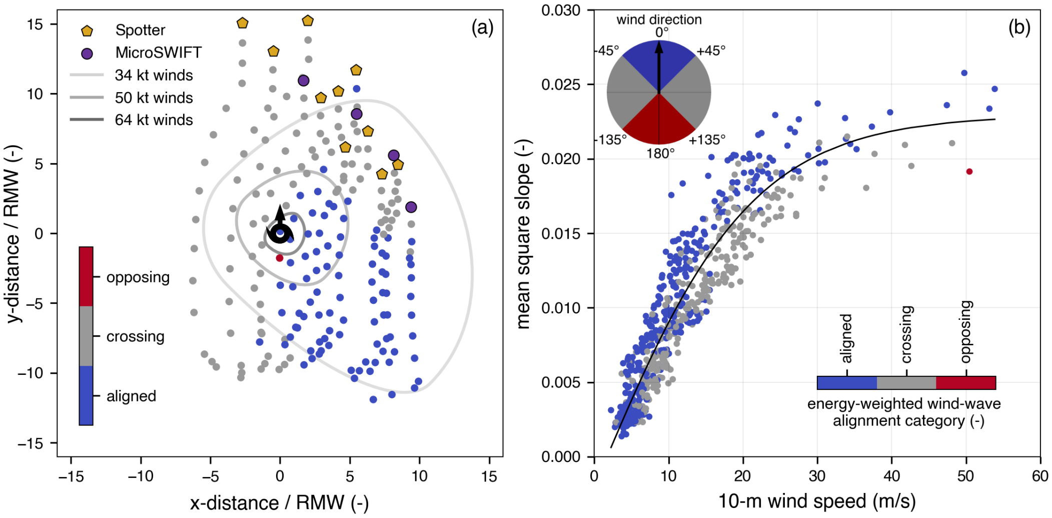

Figure 4.5: (a) Wind-wave alignment categories in the storm-following reference frame and (b) buoy mean square slope versus COAMPS-TC 10-m wind speed, classified by wind-wave alignment using an energy-weighted wave direction. The overall fit, Equation 4.11, is shown in (b). The legend in the upper left corner of (b) shows the definition of the alignment categories based on the wave direction (azimuth) relative to the wind direction (black arrow at 0°).

In the storm-following reference frame, the aligned wind and waves are concentrated mostly in the right-rear quadrant of the storm, extending slightly into the right-front quadrant (Figure 4.5a). The remaining observations surrounding the storm are categorized by crossing wind and waves. Opposing wind and waves are only observed once, to the rear of the storm and at a distance of 2 RMW from the center. A distinct spatial structure in wind-wave alignment has been reported by numerous authors, though the location of the aligned waves varies between the right-front (Holthuijsen et al., 2012; Schönau et al., 2024) and right-rear quadrant of the storm (Arakawa, 1954; Hu and Chen, 2011; Tamizi and Young, 2020). In many cases, the use of wind-wave alignment to describe a hurricane wave field can be more effective than the traditional use of quadrants (Zhou et al., 2022).

4.3.2 Dependence of mean square slope on wind-wave alignment

Buoy-derived mss is approximately linear as a function of 10-m wind speed up to 20 m s^{-1}, but approaches quasi-saturation at the highest wind speeds (Figure 4.5b), as described by Davis et al. (2023b). A hyperbolic tangent fit to the data is

$$\mathrm{mss} = a \tanh(b\,U_{10}) + c \tag{4.11}$$

with $a = 0.0250 \pm 0.0009$, $b = 0.0476 \pm 0.0040$ (m/s)$^{-1}$, and $c = -0.0020 \pm 0.0006$ where uncertainties represent 95% confidence intervals on the parameters derived from the covariance matrix estimated during the nonlinear least squares fitting. The root mean square error of the fit is 0.0020. Equation 4.11 is valid for $U_{10} \in [2, 52]$ m s^{-1} and for an mss integrated from $k_1 = 0.01$ rad m^{-1} to $k_2 = 1$ rad m^{-1} (wavelengths from 620 m to 6 m). Despite the asymptotic nature of tanh as $U_{10} \to \infty$, mss at these scales is not expected to asymptote completely, since a spectrum dominated by the saturation range has a nonzero contribution to mss (though the increase in slope with wind speed is drastically reduced).

When separated by wind-wave alignment, mean square slopes corresponding to aligned wind and waves have positive residuals (observations minus fit), generally sorting above the fit for wind speeds exceeding 5 m s^{-1}. Where wind and waves are crossing, mss tends to lie below the fit (negative residuals). Individual fits of Equation 4.11 to categorized mss indicate the parameter a is unique to each category (the remaining parameters are contained within confidence intervals of the other category's fit). Treating wind-wave alignment as a categorical variable, a multivariate fit to the categorized data is

$$\mathrm{mss}(U_{10}, \Delta\theta) = \left(a + a'\mathbf{1}_{\mathrm{aligned}}(\Delta\theta)\right) \tanh\left(b\,U_{10}\right) + c \tag{4.12}$$

where $\mathbf{1}_{\mathrm{aligned}}(\Delta\theta)$ is an indicator function which evaluates to 1 if $\Delta\theta$ is categorized as "aligned" and evaluates to 0 if $\Delta\theta$ is categorized "crossing" such that

$$\mathrm{mss}(U_{10}, \Delta\theta) = \begin{cases} (a + a')\tanh(b U_{10}) + c, & 0^\circ \leq |\Delta\theta| \leq 45^\circ \text{ (aligned)} \\ a \tanh(b U_{10}) + c, & 45^\circ < |\Delta\theta| \leq 135^\circ \text{ (crossing)} \\ \text{not observed} & 135^\circ < |\Delta\theta| \leq 180^\circ \text{ (opposing)} \end{cases} \tag{4.13}$$

With $a = 0.0236 \pm 0.0007$, $a' = 0.0037 \pm 0.0005$, $b = 0.0502 \pm 0.0035$ (m/s)$^{-1}$, and $c = -0.0028 \pm 0.0006$ with a root mean square error of 0.0018. The approximate 95% confidence interval on a', $[0.0032, 0.0042]$, does not contain zero, which suggests this parameter, and thus the impact of alignment on the fit, is statistically significant (Figure 4.9A). Only one observation falls into the "opposing" wind-wave alignment category such that the behavior of mss within this category is unknown.

The inverse dependence of mss on wind-wave alignment is strongest on the right side of the storm and away from the storm center (Figure 4.6). Some observations within a distance of approximately 2.5 times the RMW (2.5 × 18.5 km, or 46 km) from the center may have high mss,

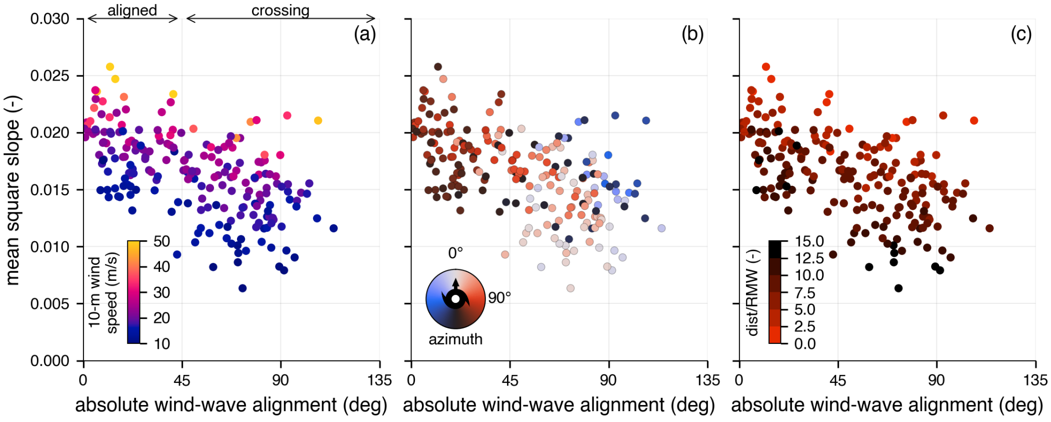

Figure 4.6: Mean square slope versus absolute wind-wave alignment classified by (a) 10-m wind speed, (b) azimuth, and (c) RMW-normalized distance relative to the center of the hurricane. The color map used in (b) is cyclic with red points corresponding to observations on the right side of the storm and blue points corresponding to observations on the left side.

even when the wind-wave alignment is large. This is likely because wind and wave directions can vary rapidly over short distances close to the center of the storm (Holthuijsen et al. (2012) remove observations inside a 30 km radius for a similar reason). Further from the center, but still within the radius of 50 knot (25.7 m s^{-1}) winds, mss is 2-3 times higher when the wind and waves are aligned compared to when the wind and waves crossing (Figure 4.6). The variance in mss increases with increasing absolute alignment.

4.3.3 *Spatial distribution of slope spectra*

The dependence of mss on wind-wave alignment suggests energy levels in the spectral tail and steepness are amplified in certain regions of the storm. The slope spectrum describes the contribution of each wavelength and direction to mss

$$S(k, \varphi) = k^2 E(k, \varphi) \tag{4.14}$$

Where φ is spectral wave direction. To compute slope spectra from buoy observations, directional energy density spectra, $E(f, \varphi)$, are estimated from the Maximum Shannon Entropy Method (MEM-II) and converted to the wavenumber domain, $E(k, \varphi)$, using Equation 4.3 (Kobune and Hashimoto, 1986; Christie, 2024). A comparison of directional slope spectra with wind and wave directions by storm quadrant is shown for four representative buoys in Figure 4.7. Observations in each quadrant are from unique buoys between 2 RMW to 4 RMW from Idalia's center and are collected within a three-hour span.

Where wind and waves are aligned, the highest energy at each frequency in the slope spectrum is concentrated along the same direction and slopes are elevated. At these wind speeds, the highest frequencies are dominated by the f^{-5} (k^{-3}) saturation range, thus energy levels in slope spectra decay (as f^{-1}) as the frequency increases (Figure 4.12). The wind-wave alignment dependence means mss can be substantially higher in aligned conditions compared to crossing crossing conditions, even if wind speeds are comparable. This is the case in Figure 4.7: in the right-rear quadrant $U_{10} = 34$ m s^{-1}, $|\Delta\theta| = 10°$, and mss $= 0.023$ compared to the left-front with

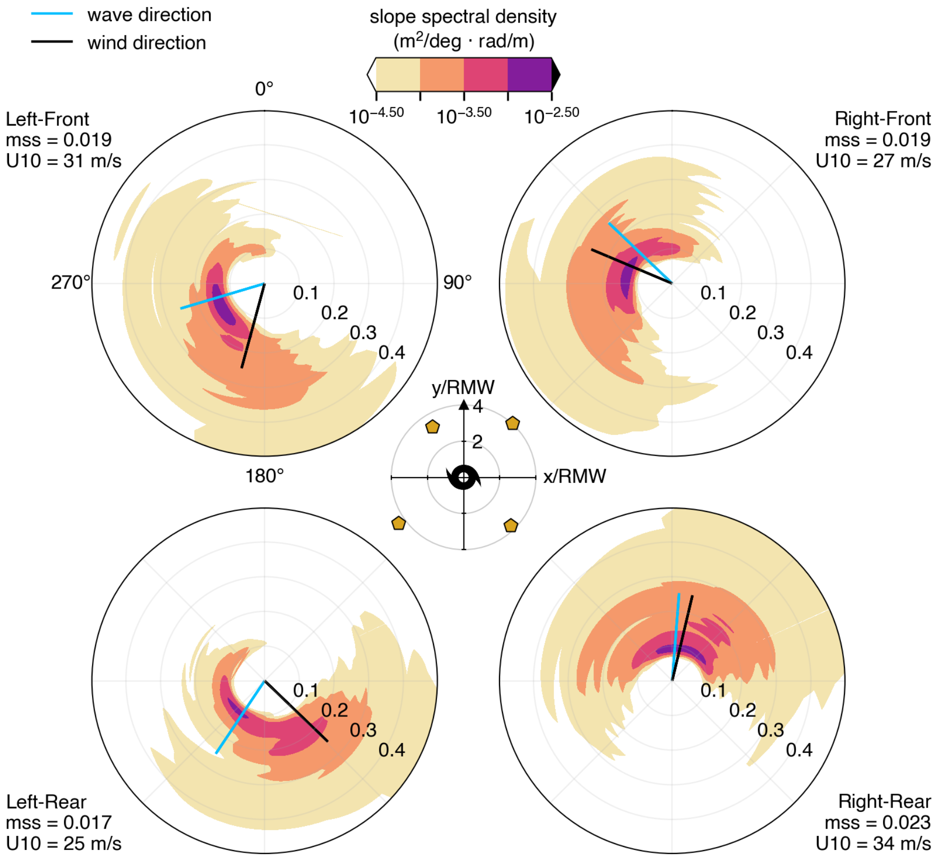

Figure 4.7: Example directional slope spectra in each of the four quadrants. In each plot, the azimuth indicates the direction of the energy and frequency increases radially outward (frequencies are shown as mapped from their corresponding wavenumber via the dispersion relation). All directions are in the "going to" convention and 0° is aligned with the hurricane's heading. The center panel shows the position (in RMW-normalized coordinates) of each buoy relative to the hurricane's center.

$U_{10} = 31$ m s^{-1}, $|\Delta\theta| = 54^{\circ}$, and mss $= 0.019$. The percent difference in mss across quadrants is 19%. In contrast, evaluating the fit to all data in Equation 4.11 (primary wind speed dependence) at these wind speeds predicts only a 5% difference (mss = 0.020 to mss = 0.021). (However, these wind speeds fall within the 7 m s^{-1} uncertainty estimated for high wind regions in COAMPS-TC.)

4.3.4 Down-wind and cross-wind mean square slope

Down-wind and cross-wind mss components describe slope energy projected along and perpendicular to wind direction, respectively. After the directional slope spectrum is rotated such that wind direction is aligned with the positive x-axis, the down- and cross-wind mss are the components along each axis (Elfouhaily et al., 1997)

$$\mathrm{mss}_{\mathrm{down}} = \int_{k_1}^{k_2} \int_{0}^{2\pi} \cos^2(\varphi) S(k, \varphi) d\varphi dk \tag{4.15}$$

and

$$\mathrm{mss}_{\mathrm{cross}} = \int_{k_1}^{k_2} \int_{0}^{2\pi} \sin^2(\varphi) S(k, \varphi) d\varphi dk \tag{4.16}$$

where φ is defined in the mathematical convention: 0° is aligned with the positive x-axis (wind direction), directions indicate “going to”, and values are measured positive counterclockwise. By definition, $\mathrm{mss} = \mathrm{mss}_{\mathrm{down}} + \mathrm{mss}_{\mathrm{cross}}$.

Down-wind slopes are consistently higher in aligned wind and wave conditions across all wind speeds (Figure 4.8). Cross-wind slopes are elevated in aligned wind and waves until 30 m s^{-1}, beyond which cross-wind slopes in the aligned condition cease to increase. In contrast to

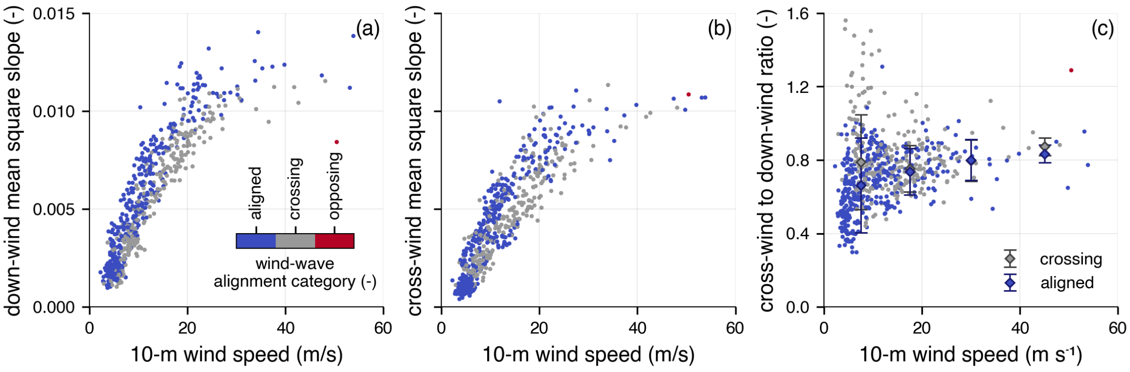

Figure 4.8: Mean square slope components: (a) Down-wind ($\mathrm{mss}_{\mathrm{down}}$), (b) cross-wind ($\mathrm{mss}_{\mathrm{cross}}$), and (c) cross-wind to down-wind ratio, all versus 10-m wind speed and classified by wind-wave alignment using an energy-weighted wave direction.

the components, the ratio of cross-wind to down-wind mss, a measure of slope directionality, does not show substantial variation over most wind speeds (Figure 4.8c). The exceptions are at low wind speeds, where the ratio is sensitive, and at high wind speeds, where there are few data points. Bins centered on wind speeds [7.5, 17.5, 30.0, 45.0] m s^{-1} with [10, 10, 15, 15] m s^{-1} widths have medians ± 1 standard deviation of [0.66 ± 0.17, 0.74 ± 0.11, 0.80 ± 0.11, 0.83 ± 0.11] (aligned) and [0.79 ± 0.26, 0.75 ± 0.13, 0.80 ± 0.11, 0.87 ± 0.05] m s^{-1} (crossing).

4.4 Discussion

4.4.1 Drag coefficient and wind-wave alignment

Mean square slope is enhanced in aligned conditions (low wind-wave alignment values) relative to crossing conditions (moderate wind-wave alignment) as shown in Figures 4.5 and 4.6. The dependence of mss on wind-wave alignment in hurricanes is consistent with the dependence of drag coefficient on wind-wave alignment in hurricanes shown in some models (Husain et al., 2022; Manzella et al., 2024) and in some observations (Chen et al., 2022; Zhou et al., 2022). These studies find drag coefficient is lower in crossing conditions relative to aligned conditions. The reduction of drag coefficient with decreasing wind-wave alignment may be attributed to the reduction of long wave-induced form drag in crossing sea states (Zhou et al., 2022). Model studies have demonstrated correlation between mss and form drag (Sullivan et al., 2018), thus the dependence of both mss and drag coefficient on wind-wave alignment is plausibly related. Buoy-measured mss is only a partial representation of the spectral tail (up to 0.5 Hz or 6-m wavelength), but it captures the energetic region of the gravity wave spectrum including larger and longer waves hypothesized to steer form stress in aligned and crossing sea states, the equilibrium range, and the start of the saturation range (at moderate wind speeds).

Despite qualitative agreement between the dependence of mss and drag coefficient on alignment, based on results from the aforementioned models and observations, drag coefficient is not consistently observed to decrease in crossing wind and waves. Drag coefficients reported by Holthuijsen et al. (2012) are lower in crossing conditions than in following (aligned) conditions below 25 m s^{-1}, which agrees with the mss dependence. Above this wind speed, however, drag coefficients in crossing winds and waves greatly exceed drag coefficients in following winds and waves, which is opposite the mss dependence. A modest increase of drag coefficient in crossing conditions has also been observed outside of tropical cyclones, including behind atmospheric cold fronts embedded in extratropical cyclones (Sauvage et al., 2024). These inconsistencies suggest the dependence of drag coefficient on wind-wave alignment varies across regimes. Variation in mss dependence on wind-wave alignment across similar regimes has yet to be explored.

4.4.2 Generalization to other tropical cyclones

The spatial pattern of wind-wave alignment is similar to that of Zhou et al. (2022) and Chen et al. (2022): wind and waves are aligned to the rear of the storm significantly far from the center, but are misaligned in the far right-front (beyond 2-3 × RMW) and on the left side of the storm (Figure 4.5a). While this pattern is frequently reported in hurricane observations, it is not universal. Other works, for example, have reported alignment towards the right-front (Holthuijsen et al., 2012; Schönau et al., 2024).

It is likely that the strength, size, and translational speed of a hurricane shift wave directions, and thus the aligned region, within the right side of the storm due to the moving fetch phenomenon (Kudryavtsev et al., 2021). While the self-similar solutions for wave direction derived by Kudryavtsev et al. (2021) might be used with Equation 4.12 to produce a spatial map of mss based on storm metrics alone, the validity of the solutions is limited to waves within a radius of 3 × RMW (most observations are further from the storm due to Idalia's small RMW, Figure 4.5). The correlation between mss and wind-wave alignment suggests the region with elevated slopes should consistently coincide with the region of best alignment, however conclusive evidence will require observations across several storms with varying spatial distributions of wave direction. The region of highest slopes is unlikely to be constrained by quadrant (e.g, the highest slopes may not always occur in the right-rear quadrant).

4.4.3 Storm-following reference frame considerations

Buoy data over a 15-hour period are used to construct the storm-following reference frame observations shown in Figures 4.4 and 4.5. Wave observations are made simultaneously in the cross-track direction, but mostly rely on the storm's progression over the array to sample in the along-track direction (though there are instances where the array spans all four quadrants at the same time, e.g., Figure 4.7). In the first half of this period, from 00Z to 06Z on 30 August, the maximum wind speed increased by 6 m s^{-1} (12 knots) peaking at 53.5 m s^{-1} (104 knots) while the array was still in the front half of the storm (Figure 4.2g). Past 06Z, the maximum wind speed fell by 2 m s^{-1} (4 knots) as the array was in the back half of the storm. Thus it is unlikely that storm intensification is responsible for the elevated mss in the right-rear of the storm. While waves in the back half of the storm experience a longer duration of forcing as the storm passes, prior work suggests the response time of buoy-measured mss is between 0.4 and 1.2 hours (at 14 m s^{-1}), and that the response time decreases as wind speed increases, as the upper frequency limit increases, and as atmospheric stability decreases (Chen et al., 2016). The 1-hour spacing of the buoy observations should be sufficient for mss to respond.

4.4.4 Doppler Adjustment Implications

Buoy observations require an adjustment for the Doppler shift that occurs between the observed reference frame of the buoy and the intrinsic reference frame of the waves. Spotter spectra are adjusted for Doppler shift due to a 1.2% wind slip and Stokes drift, while microSWIFT spectra are adjusted only for Stokes drift. Spotter mean square slopes at the highest wind speeds (> 30 m s^{-1}) can increase by as much as 30% after adjusting to the intrinsic frame, which indicates saturation of mss with wind speed is less acute than previously described in Davis et al. (2023b) (see Appendix A). The dependence of mss on wind wave alignment is robust whether data are adjusted for the Doppler shift or not (Figure 4.9). Equation 4.11 fit to the observed (not adjusted) data suggests the b parameter is instead unique to each category. Using the same indicator function, this coefficient can be replaced with $b + b'\mathbf{1}_{\text{aligned}}(\Delta\theta)$ where $a = 0.0208 \pm 0.0006$, $b = 0.0530 \pm 0.0040$

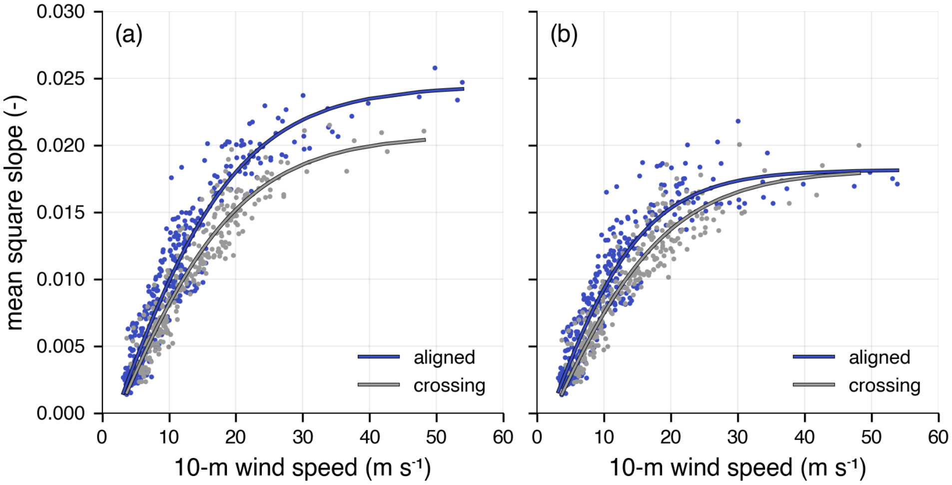

Figure 4.9: Aligned and crossing fit to mean square slope versus 10-m wind speed for (a) Intrinsic (Doppler-adjusted) mean square slope and (b) observed mean square slope.

(m/s)$^{-1}$, $b' = 0.0121 \pm 0.0023$ (m/s)$^{-1}$, and $c = -0.0026 \pm 0.0006$ (95% confidence intervals). The upper and lower bounds on b' are $[0.0098, 0.0144]$ (m/s)$^{-1}$ such that this coefficient remains statistically significant between categories when fit to observed mss. Aligned and crossing observed mss converge at high wind speeds (> 30 m s^{-1}), since the spectral tail that determines mss is significantly Doppler shifted due to wind slip.

4.4.5 Other secondary dependencies

There are several other plausible mss secondary dependencies aside from wind-wave alignment. Inverse wave age, the ratio of wind speed to the wave phase speed, is commonly used to parameterize drag coefficient (Edson et al., 2013). When calculated using phase speed at the energy-weighted wave period, inverse wave age correlates with wind speed, but does not explain variation in mss at a given wind speed (Figure 4.10a). Long waves steepen as they shoal and may modulate shorter waves through sheltering or increased turbulence, however there is not a distinct dependence of mss on relative depth (Figure 4.10b). It is possible that depth still effects mss indirectly through an increase in wind-wave misalignment as larger waves shoal, though

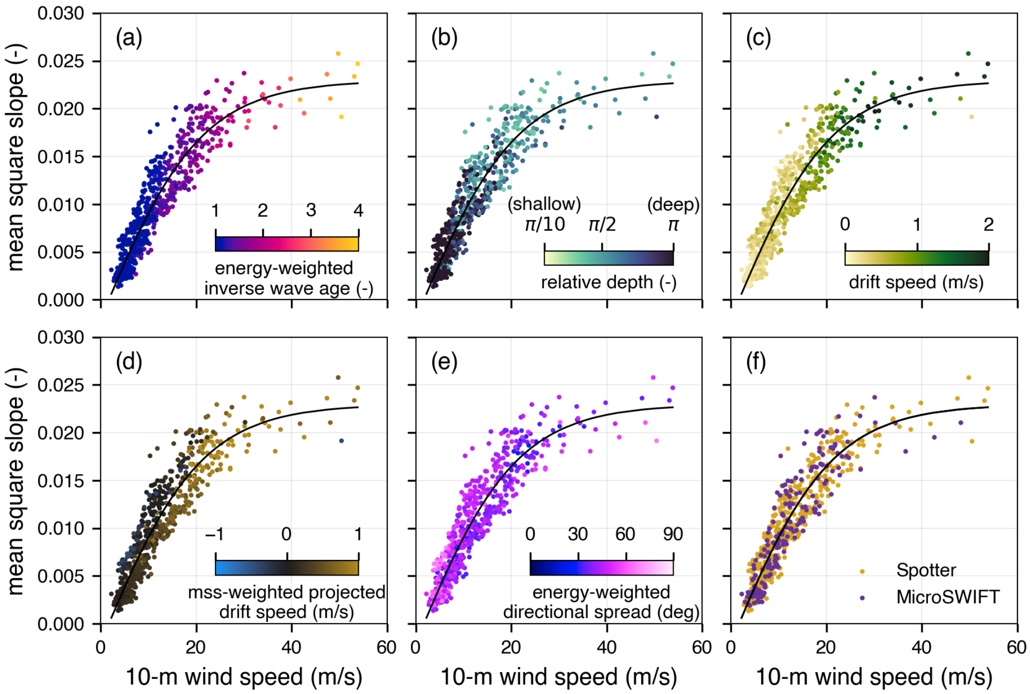

Figure 4.10: Mean square slope versus 10-m wind speed classified by: (a) inverse wave age calculated using wave phase speed at the energy-weighted period; (b) relative water depth, or kh, calculated as the product of energy-weighted wavenumber and water depth; (c) buoy drift speed; (d) drift speed projected onto mss-weighted wave direction; (e) wave directional spread calculated from energy-weighted directional moments; and (f) buoy type.

this would require comparison to observations in deep water (Chen et al., 2020a). Wave steepening (or flattening) can occur as waves cross surface current gradients (Iyer et al., 2022). Buoy drift speed, a proxy for surface current magnitude, increases with increasing wind speed approximately as the 3% rule of thumb, e.g., Samelson (2022) (Figure 4.10c). When projected onto mss-weighted wave direction, projected drift speed does not elevate or lower mss as observed in Iyer et al. (2022); waves would need to be measured crossing surface current gradients for a Doppler shift of this type to be directly observed (Figure 4.10d). The mss-weighted wave direction used in the projected drift speed is calculated from Equation 4.8 with an a_1 and b_1 weighted by the fourth spectral moment and is chosen since this is the wave direction at the frequencies with the largest contribution to mss. There is not substantial variation of mss with the directional spread calculated using energy-weighted moments, though normalization of mss by directional spread was found to improve parameterizations by Banner et al. (2002) and Schwendeman et al. (2014) (Figure 4.10e). There is no appreciable bias introduced by buoy type (Figure 4.10f).

Hwang and Fan (2018) find a moderate secondary dependence on hurricane wind field asymmetry, a weaker dependence on the maximum wind speed, and little to no dependence on the radius of maximum wind speed. Several modeling and observational studies have reported variations in wind stress and drag coefficient from deep to shallow water (Jiménez and Dudhia, 2018; Chen et al., 2020a, 2022). Variations are primarily attributed to wave shoaling, and specific trends appear to have a complex dependence on factors such as beach slope and storm translation speed. A comparison across datasets with a similar spatial density, but with varying hurricane conditions, is required to test for mss dependencies on water depth and storm strength, size, and translational speed.

4.4.6 Extension to higher wavenumbers

The primary dependence of mss on wind speed in hurricanes is consistent across measurement platforms, including radar measurements which resolve mss down to wavelengths of 0.2 m (Davis et al., 2024a). From the present dataset, it is not clear whether the secondary dependence of mss on wind-wave alignment persists down to shorter wavelengths. Future work should use methods capable of near-synoptic measurements of short-wave mss and wave direction in hurricanes to test for this dependence. Efforts to test the dependence of Wide Swath Radar Altimeter mss on wind-wave alignment are ongoing.

4.5 Conclusions

Mean square slope, mss, has a primary dependence on wind speed that is linear at low-to-moderate wind speeds and approaches saturation at hurricane wind speeds. Observations from an array of drifting buoys deployed inside Hurricane Idalia (2023) show mss, resolved down to 6 m wavelength, has a secondary dependence on wind-wave alignment which can help explain variation in mss at a given wind speed. Mean square slopes are higher where wind and waves are aligned than where wind and waves are crossing. This dependence is robust across all observed wind speeds, as indicated by fits to the respective categories. In the case of Idalia, slopes are elevated in the right-rear of the storm where wind-wave alignment is the closest. The dependence of mss on wind-wave alignment resembles the dependence of drag coefficient on wind-wave alignment described in recent observational and model studies (Zhou et al., 2022; Manzella et al., 2024). Form drag formulations depend on the shape and energy level within the spectral tail, both of which are reflected by changes in mss (Donelan et al., 2012). This suggests dependencies of mss and drag coefficient on wind-wave alignment are related. Future work should focus on testing this dependence with methods that can resolve wave spectra at higher frequencies inside hurricanes.

Open Research Section

Data are available on Dryad (`https://doi.org/10.5061/dryad.zw3r228h7`) and are cited as Davis et al. (2024b). Source code can be accessed via GitHub (`https://github.com/jacobrdavis/ocean-surface-wave-slopes-and-wind-wave-alignment-observed-in-Hurricane-Idalia`) or Zenodo (`https://doi.org/10.5281/zenodo.13953570`) and are cited as Davis (2024). Hurricane Best Track data and storm metrics are from the International Best Track Archive for Climate Stewardship (IBTrACS) (Knapp et al., 2010b; Gahtan et al., 2024). Shapefiles of the storm track and wind swaths used in the maps are from the National Hurricane Center GIS Archive available at `https://www.nhc.noaa.gov/gis/`. Bathymetric data are from the 2023 General Bathymetric Chart of the Oceans (GEBCO Bathymetric Compilation Group, 2023). Data from National Data Buoy Center Station 42036 (West Tampa) are available on the NDBC archive (NOAA National Data Buoy Center, 1971). Stepped Frequency Microwave Radiometer data are available at `https://www.aoml.noaa.gov/2023-hurricane-field-program-data/#idalia`. Colormaps are from colorCET (`https://colorcet.holoviz.org/`) and cmocean (`https://matplotlib.org/cmocean/`) (Kovesi, 2015; Thyng et al., 2016). Directional spectra are estimated using the Rogue Wave Spectrum package (`https://github.com/sofarocean/oceanwavespectrum`).

Acknowledgments

This work was funded by the U.S. National Ocean Partnership Program (NOPP) as part of the NOPP Hurricane Coastal Impacts project (ONR Grant N00014-21-1-2194). Air-support was provided by the Navy VXS-1 Scientific Deployment Squadron via the Naval Research Laboratory. Gijs de Boer, Brian Butterworth, Elizabeth Thompson and Chris Fairall were additionally supported by the NOAA Physical Sciences Laboratory, and the work was supported in part through NOAA cooperative agreement NA22OAR4320151, for the Cooperative Institute for Earth System Research and Data Science (CIESRDS). Co-authors Doyle and Moskaitis gratefully acknowledge support from Office of Naval Research grant Program Element 0601153N. Computational resources for the COAMPS-TC forecasts were provided by the Navy Department of Defense Supercomputing Resource Center in Stennis, Mississippi. We thank APL engineers Alex de Klerk, Phil Bush, and Brenton Salmi for their work to prepare and test the microSWIFTs. This material is based upon work supported by the National Science Foundation Graduate Research Fellowship Program under Grant No. (NSF grant DGE-2140004). Any opinions, findings, and conclusions or recommendations expressed in this material are those of the author(s) and do not necessarily reflect the views of the National Science Foundation.

Appendix A: Doppler-adjusted observations

The Doppler-adjusted Hurricane Ian and Fiona (2022) datasets (prior work) are shown with the Idalia (2023) dataset (current work) in Figure 4.11. There is little to no difference between observed and intrinsic observations below 20 m s^{-1}, however intrinsic mss can be as much as 30% higher compared to observed mss at wind speeds exceeding 35 m s^{-1}. Intrinsic mss saturation is not as strong as previously reported, however the rate of increase in mss with 10-m wind speed is substantially reduced above 25 m s^{-1}.

When the Doppler-adjusted Idalia data are binned by 10-m wind speed (following prior work), the mean spectra remain dominated by the f^{-5} saturation range at the highest wind speeds (Figure 4.12). The f^{-4} equilibrium range is progressively narrowed until it is nearly absent at

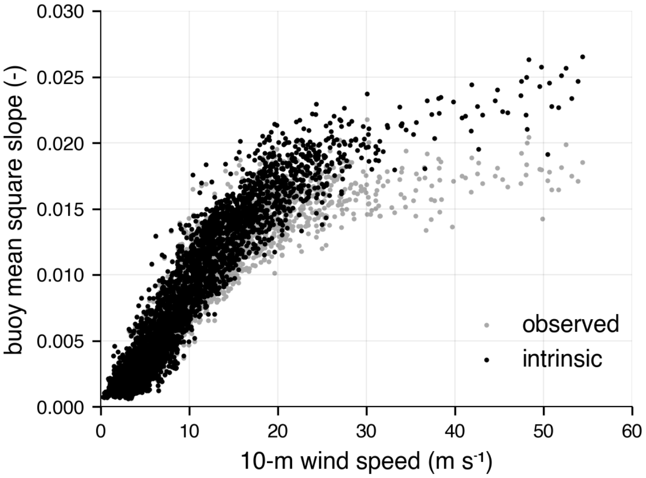

Figure 4.11: Observed and intrinsic mean square slope (0.05 Hz to 0.5 Hz) versus wind speed. The data include observations from Hurricane Idalia (this study) and Hurricanes Ian and Fiona (Davis et al., 2023b).

wind speeds exceeding 25 m s^{-1}. The increase in spectral tail steepness is directly reflected in the change in mss: an mss integrated over a largely saturated spectrum with $E(f) \sim c_s f^{-5}$ has only logarithmic contributions to mss with increasing frequency, whereas the contributions of equilibrium range with $E(f) \sim c_e f^{-4}$ are linear in frequency (c_s and c_e are constants related to the spectral energy levels).

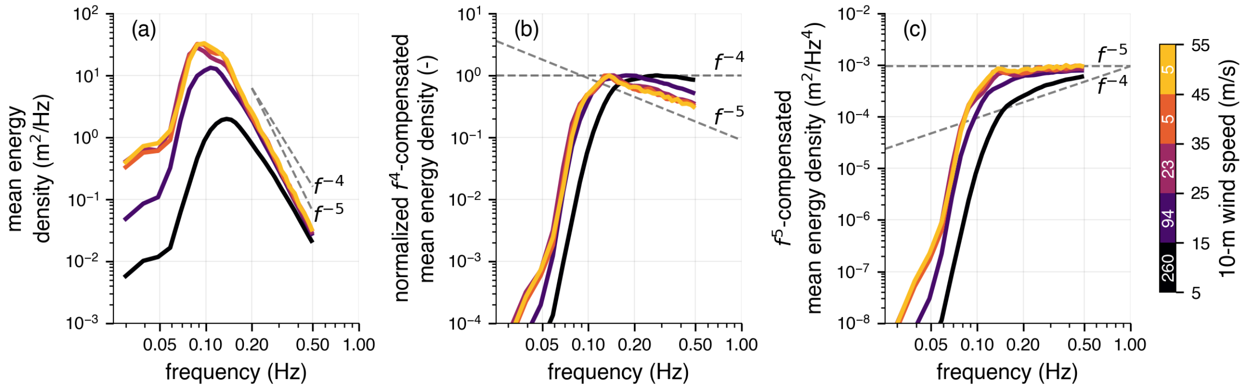

Figure 4.12: Hurricane Idalia Spotter spectra in 10 m s^{-1} wind speed bins: (a) mean energy density; (b) mean energy density compensated by f^4 and normalized by the maximum value in each respective bin; and (c) mean energy density compensated by f^5. Bin counts (number of 1-hour spectra) are labeled inside of the color bar.

Appendix B: COAMPS-TC validation

Reforecast COAMPS-TC fields were validated using observations collected from 29 August to 31 August 2023. Surface wind speed SFMR observations from five missions flown by NOAA and the United States Air Force Reserve Weather Reconnaissance Squadron were colocated with COAMPS-TC using the same interpolation method used to colocate buoy observations. SFMR observations (1 Hz) were averaged to 1-minute wind speeds (COAMPS-TC outputs instantaneous values representative of a 1–10 min average).

The distribution of COAMPS-TC wind speed errors relative to SFMR, created from n = 1,289 comparisons, has a mean (bias) of 2 m s^{-1} and a standard deviation (error) of 6 m s^{-1} (Figure 4.13). When grouped into 10 m s^{-1} bins spanning 15 m s^{-1} to 55 m s^{-1}, error increases as 19–24% of wind speed. Above 30 m s^{-1}, COAMPS-TC is biased high relative to SFMR (Figure 4.14a). A storm-centered composite of COAMPS-TC wind speed errors suggests COAMPS-TC overestimated the size of the storm near the actual RMW (Figure 4.14b). Most buoy observations are outside the RMW, where COAMPS-TC and SFMR are in good agreement (Figures 4.4 and 4.5). Despite an underestimation of storm size, there is little bias across storm quadrants (which might otherwise produce an erroneous mean square slope dependence on wind-wave alignment).

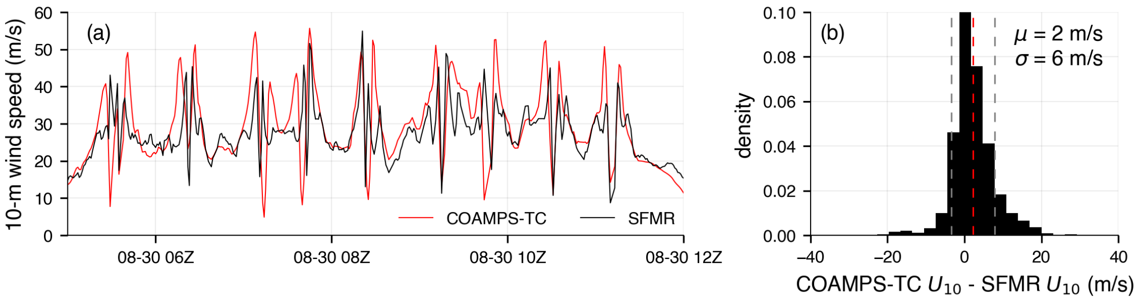

Figure 4.13: (a) Example time series of COAMPS-TC and SFMR 10-m wind speed. SFMR data are from mission 20230830U1 flown on 30 August. (b) Histogram of COAMPS-TC surface wind speed error, relative to SFMR surface wind speed, created from n = 1,289 total observations. Dashed lines represent the mean (red) and mean ± 1 standard deviation (gray).

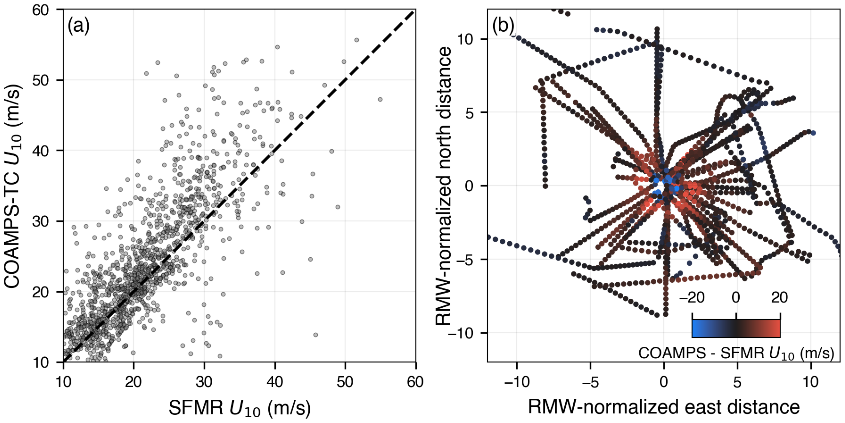

Figure 4.14: (a) Comparison of SFMR and COAMPS-TC surface wind speed estimates. (b) COAMPS-TC surface wind speed error in a storm-centered, RMW-normalized reference frame.

Hurricane Idalia passed almost directly over NDBC Station 42036 moored at (28.501 N, 84.508 W). Station 42036 was as close as 10 km to Idalia's center on 30 August 06Z. COAMPS-TC 10-m wind directions were compared with NDBC-measured wind direction, reported every 10-minutes at an anemometer height of 3.8 m. A distribution of COAMPS-TC wind direction errors relative to NDBC, created from $n = 282$ comparisons, has a mean of -6 degrees and a standard deviation of 19 degrees (Figure 4.15). The accuracy of COAMPS-TC wind direction should be sufficient for the broad categorization of wind-wave alignment used to obtain the results (aligned, crossing, or opposing).

COAMPS-TC and NDBC Station 42036 wind speeds compare well until the buoy is inside Idalia (Figure 4.16). Within the storm, Station 42036 reported a maximum 10-minute wind speed of 25 m s^{-1} and maximum 1-minute wind speed of 28 m s^{-1} (at 3.8-m anemometer height). These observations are much lower than the maximum 10-m wind speed of 46 m s^{-1} reported by COAMPS-TC at the buoy's location. (Station 42036 recorded gusts as high as 36.5 m s^{-1} at anemometer height, though gustiness is not resolved by COAMPS-TC.) The large difference in buoy-measured and modeled wind speed is unlikely to be accounted for by differences in measurement height alone. General agreement in wind speed magnitude between COAMPS-TC and

SFMR (Figure 4.13) suggests NDBC Station 42036 is potentially unrepresentative of true 10-m wind speed during Idalia's passing. Some of this difference may be from measurement bias within the wave boundary layer (Buckley and Veron, 2016). NDBC-reported significant wave heights exceed the 3.8 m anemometer height during Idalia's entire passing (the maximum significant wave height is 6.3 m). Previous work has reported low wind measurement bias due to flow distortion over waves below 18 m s^{-1} (Wright et al., 2021), however large differences observed here warrant investigation into sheltering effects on measured winds within hurricanes. COAMPS-TC also predicts an earlier arrival of the storm, though errors due to phase shift and storm structure should be well-captured by the SFMR wind speed error analysis.

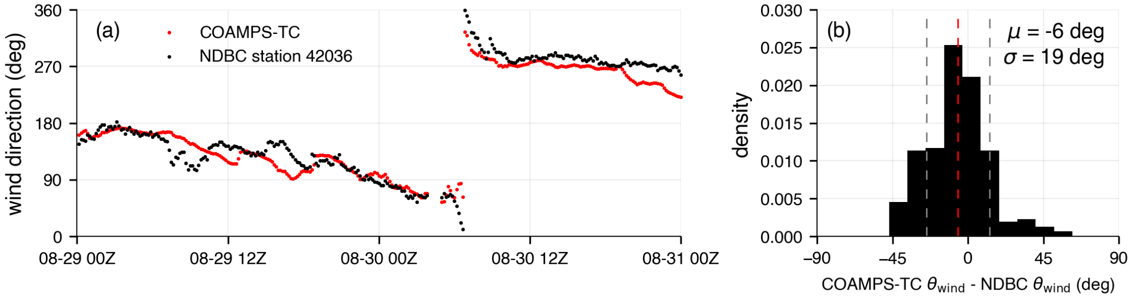

Figure 4.15: (a) Time series of COAMPS-TC and NDBC wind direction. (b) Histogram of COAMPS-TC wind direction error relative to NDBC wind direction. Dashed lines represent the mean (red) and mean ± 1 standard deviation (gray).

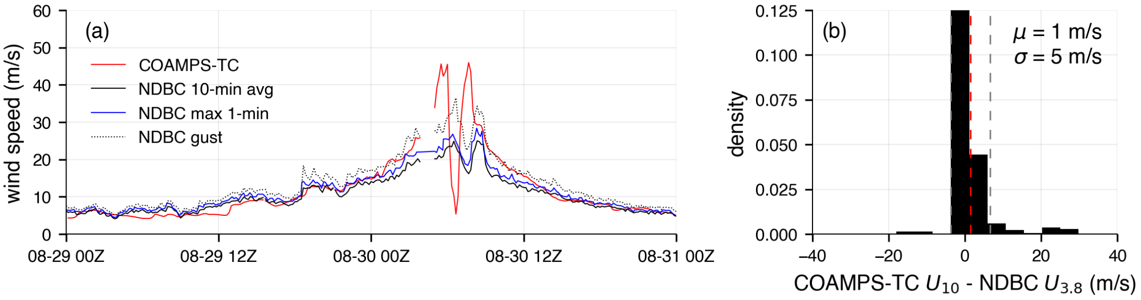

Figure 4.16: (a) Time series of COAMPS-TC 10-m wind speed and NDBC 3.8-m wind speed. (b) Histogram of COAMPS-TC wind speed error relative to NDBC wind speed. Dashed lines represent the mean (red) and mean ± 1 standard deviation (gray).

Chapter 5

DATA-DRIVEN METHODS FOR OCEAN SURFACE WAVE MEASUREMENT USING A SUBMARINE FIBER-OPTIC CABLE

Abstract: *Two new data-driven models for estimating ocean surface waves from distributed acoustic sensing (DAS) submarine cable strain rate are developed using supervised machine learning on a 10-day dataset collected offshore of Oliktok Point, Alaska. The new models were trained on target data from pressure moorings at three sites along 27.1 km of cable and were benchmarked against an empirical transfer function method previously used to estimate waves from DAS. A model which uses convolutional neural networks to transform frequency-wavenumber spectra to seafloor pressure spectra outperforms the benchmark in wave height prediction (RMSE of 0.15 m versus 0.41 m) and period prediction (0.29 s versus 0.37 s) when evaluated on the Oliktok cable. A two-layer, fully-connected neural network is only marginally more skillful than the benchmark when trained on target data from several along-cable sites, but is capable of accurate significant wave height prediction when trained at a single location. Regression-based machine learning is useful for estimating waves from DAS data when the pressure-strain relationship varies temporally and spatially across different wave conditions.*

5.1 Introduction

Seafloor distributed acoustic sensing (DAS) measures submarine fiber optic cable strain in response to external signals in the water column and seafloor sediments. Strain, or strain rate, can be used to infer information about external loads, including ocean surface gravity waves, seismic waves, and acoustic sources (Xenaki et al., 2025). Measurements can be collected on both preexisting telecommunication cables or custom-installed cables, providing many kilometers of fiber suitable for DAS interrogation. Strain is returned at channels spaced every several meters along the cable, enabling highly spatially- and temporally-resolved geophysical observations. Previous work has demonstrated the ability for DAS to measure oceanographic processes, including ocean seismology (Williams et al., 2019), ocean currents (Williams et al., 2022), sea-ice processes and wave interactions (Baker and Abbott, 2022; Smith et al., 2023), and nearshore hydrodynamics

(Glover et al., 2024b).

This work focuses on the measurement of ocean surface gravity waves via DAS, as inferred from along-cable strain (or strain rate) records. Wave-induced cable strain is caused by dynamic pressure fluctuations from waves in shallow and intermediate relative water depths (Glover et al., 2024b). Wave signals are evident in DAS spectral content in intrinsic strain units, typically nanometers per meter, notably through dispersion relationship signatures in frequency-wavenumber (f-k) spectra (Lindsey et al., 2019; Williams et al., 2019, 2022). Phase information is sufficient for observing many wave processes, avoiding the need to convert strain amplitude to the amplitude of target measurement. For example, current-induced Doppler shift in the measured dispersion relationship from strain f-k spectra can be used to infer depth-averaged currents (Williams et al., 2022; Lin et al., 2024). Recent work has also explored the use of DAS for resolving infragravity waves from f-k spectra, which has potential to compliment Tsunami early warning systems (Xiao et al., 2024). Fewer studies use DAS to measure ocean waves in units of pressure head or surface elevation (e.g., meters). A key challenge is determination of the amplitude relationship between strain and pressure, which minimally depends on gauge length, incident wavelength, seafloor compliance, cable properties, temperature, and interrogator setup (Glover et al., 2024b). Many of these properties are often unknown or difficult to characterize over the entire length of cable used for DAS.

Smith et al. (2023) use an empirical, frequency-domain transfer function for transforming strain to pressure. The transfer function is defined as the median of the ratio of many known pressure spectra to measured strain spectra collected over time. They applied this method to a 6-day DAS dataset from a telecom cable offshore of Oliktok Point, AK (the cable used in this work) using depth-attenuated spectra from a surface wave buoy moored above the cable as ground truth. Pressure spectra estimated from DAS were converted to surface elevation spectra and used to calculate significant wave height (H_s) and energy period (T_e) over the analysis period. In relatively calm conditions ($H_s \leq 0.4$ m and $T_e < 3.5$ s), DAS-estimated wave heights and periods compared well relative to the buoy (RMSE of 0.10 m and 0.65 s, respectively). The estimated spectra were sufficient to determine sea-ice attenuation rates during the autumn freeze-up. Glover et al. (2024b) applied this method to several weeks of data from a field-deployed cable in Duck, NC, using three Nortek Acoustic Wave and Current profilers as ground truth. Over a wider range of conditions, up to 4-m H_s and 18-s T_e, the median transfer function produced excellent wave estimates with a typical height and period RMSE of 0.2 m and 1 s, respectively. Meulé et al. (2024) derive both emprical and semi-analytical transfer functions from DAS and seafloor pressure data (RBR virtuoso) on a cable in the South of France in moderate conditions (H_s between ~0.1 and 2.5 m). Their empirical method achieves good total energy level prediction performance when applied in 10- to 60-minute windows (coefficient of determination, R^2, of 0.95), but it depends on a highly linear relationship between band-passed strain and pressure spectral variances. Their linear wave theory-based, semi-analytical method has more scatter, but is more interpretable than empirical methods.

Here we explore the use of supervised machine learning for transforming DAS-measured strain rate to seafloor pressure (and thus surface elevation) in the frequency domain. Machine learning-based models may be appropriate, or even necessary, for cables and conditions where the pressure-strain relationship is nonlinear (e.g., the cable's stress response to small pressures is different from the response to large pressures). The flexibility of these models enables the use of metadata which are known to be important to the problem—such as water depth, cable burial depth, along-cable distance, or wave direction—but for which precise relationships are not well-constrained in a particular setting. DAS also produces large volumes of data, making it a good candidate for data-driven methods. Machine learning has previously been combined with DAS, for example to track sea ice extent via unsupervised learning (Peña Castro et al., 2023), map strain to microseism location and velocity using a residual neural network (Wamriew et al., 2021), predict glacier discharge with a Long Short-Term Memory model (Manos et al., 2024), and separate ocean gravity and seismic waves using the SHallow REcurrent Decoder (SHRED) model (Ni et al., 2024).

The new methods are developed and tested on a DAS dataset collected in the coastal Arctic. Wave measurements from DAS can enable the study of wave-ice attenuation and related mechanisms, such as scattering, with far finer resolution than point measurements (e.g., buoy or mooring arrays) (Smith et al., 2023). Long-term cable interrogation can provide insight into seasonal trends in wave action in this region, including periods with residual spring landfast ice and newly-formed autumn sea ice (Hošeková et al., 2020, 2021).

Section 5.2 describes three data-driven models for mapping strain rate spectra to seafloor pressure spectra. These include the previously-developed median transfer function method (Smith et al., 2023; Glover et al., 2024b), and two new, machine learning-based alternatives. In Section 5.3, models are evaluated on their spectral and bulk parameter prediction skill at three sites along the cable using an independent test dataset. Spatial and temporal variations in the pressure-strain relationship, model generalization to all sites along the cable, and adaptation of the architectures to other settings are discussed in Section 5.4. Section 5.5 concludes.

5.2 Methods

5.2.1 Strain rate and seafloor pressure measurements

Distributed acoustic sensing strain rate measurements are from a Quintillion-owned submarine fiber-optic cable that runs offshore of Oliktok Point, Alaska. A dark fiber in the cable was interrogated by researchers from Sandia National Laboratories with a Silixa iDAS interrogator. Previous DAS data from this experiment have been used to map sea ice coverage (Baker and Abbott, 2022), track ice edges (Peña Castro et al., 2023), characterize submarine permafrost (Stanciu et al., 2023), and observe wave-ice interactions (Smith et al., 2023). Data used here are from 27.1 km of cable extending northward across the Beaufort shelf along the 150W meridian (Figure 5.1, left). Water depths along this portion of the cable range from 3 m to 19 m. The cable is trenched approximately 2 m into the seabed up to an along-cable distance of 16.1 km, and it is buried approximately 4 m for the remainder of the usable distance offshore. Raw data were collected at a sample rate of 100 Hz with a channel spacing of 8 m and a gauge length of 10-m. These data were concatenated into 1-hr records of along-fiber strain rate (with units of nm/m/s, or nanometer per meter per second) and downsampled to 2 Hz at channels spaced every 16-m along the cable. Downsampling was performed by first filtering the data with a zero-phase low-pass fi-

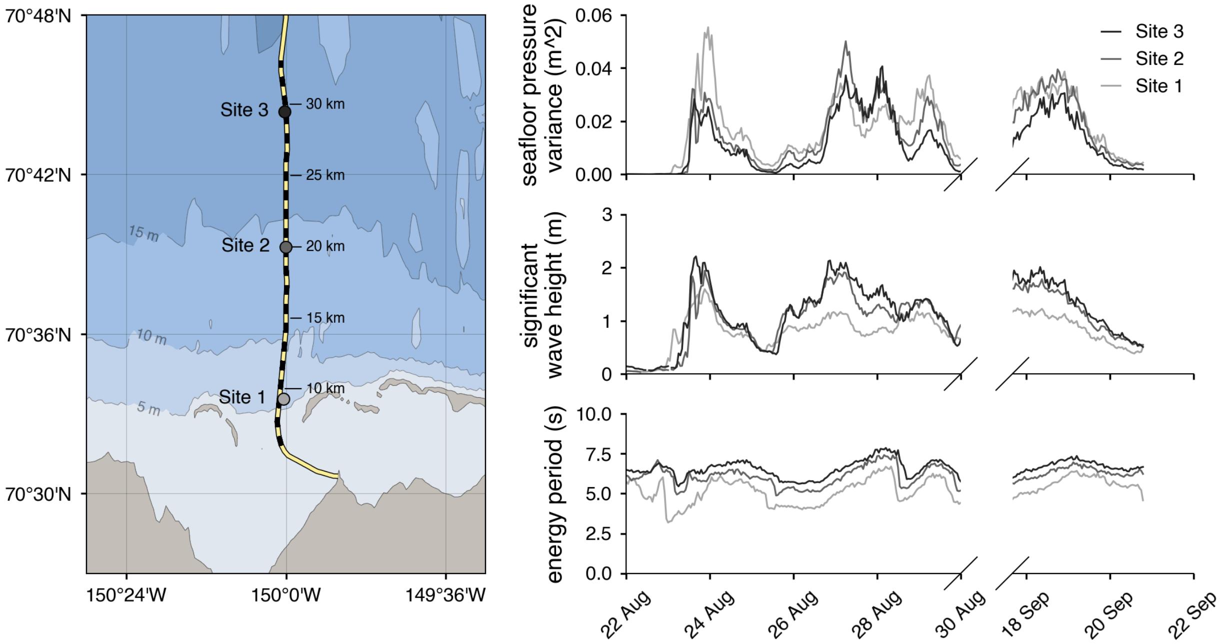

Figure 5.1: (Left) Map of the cable (yellow line) and mooring sites (markers) offshore of Oliktok Point, Alaska. The dashed portion of the cable represents the 27.1 km of channels used in the analysis. Along-cable distance from shore is indicated to the right of the cable, and contours represent bathymetry from NOAA navigation maps (Baker and Abbott, 2022). (Right) Seafloor pressure variance, significant wave height, and energy period measured by bottom pressure moorings deployed at sites 1, 2, and 3. Breaks in the axes correspond to the period when the DAS interrogator was disconnected while the cable was being repaired from ice scour damage.

nite impulse response filter (cutoff frequency of 1 Hz) and then extracting every 500th sample. This temporal and spatial resolution is sufficient to capture ocean surface gravity waves (Figure 5.2a–b).

Three RBR Duo moorings were deployed along the cable, from April to September 2023, to record seafloor pressure and water temperature (Thomson and Smith, 2024). The mooring sites, referred to as Sites 1, 2, and 3 with increasing distance from shore, are spaced roughly 10 km apart along the cable in mean water depths of 5.5 m, 14 m, and 19.5 m, respectively (Figure 5.1, left). Site 1 is located between two barrier islands, and Sites 2 and 3 are located in open water (during ice-free periods). Pressure and temperature data were collected at 2 Hz (Figure 5.2c).

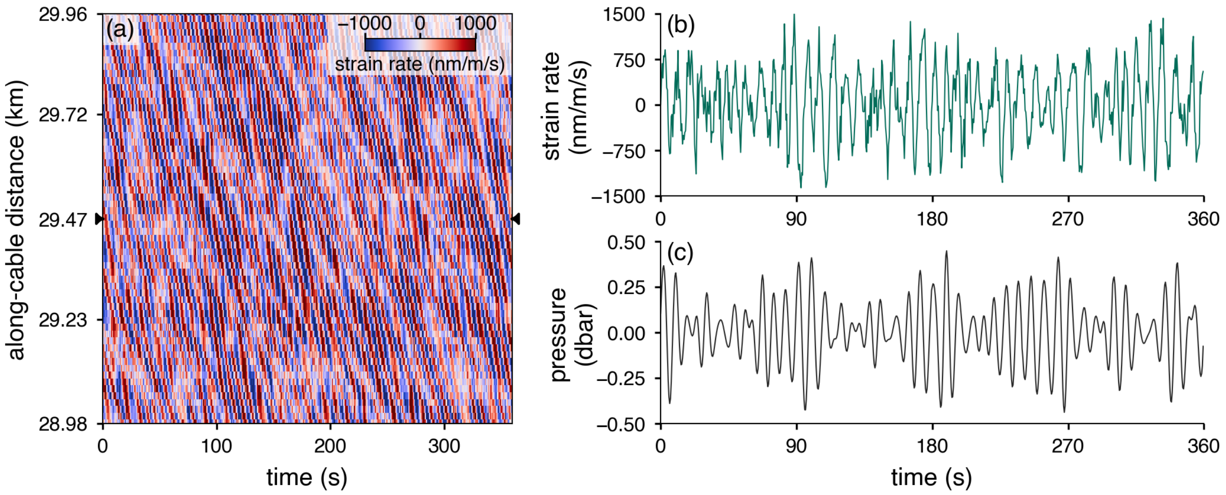

Figure 5.2: (a) Strain rate Hovmöller diagram created from the first 6 minutes of 28 August 00Z and 1 km of DAS channels centered on Site 3 (approximate along-cable distance of 29.47 km, as indicated by opposing arrows); and (b) strain rate and (c) seafloor pressure time series at Site 3 over the same time period.

Analysis focuses on a predominantly ice-free period from 22 August 2023 to 22 September 2023. This period was chosen to remove any gradients due wave-ice interactions. Wave conditions measured by the pressure moorings over this period include significant wave heights, H_s, from tens of centimeters to 2 m and energy-weighted (centroid) periods, T_e, between 3 s and 8 s (Figure 5.1, right). During this period, DAS measurements were paused for repairs on the submarine fiber-optic cable that had been damaged by ice scour earlier in the season. As a result, there is a data gap between 30 August and 18 September 2023. All subsequent time series contain a break in the x-axis during this gap.

5.2.2 *Data preparation*

Hourly strain rate and pressure spectral density estimates were computed from demeaned DAS and mooring records, respectively. Spectra were estimated using Welch's method with 512-point (256-s) Hann-windowed segments and 50% overlap. Frequencies above 0.5 Hz were trimmed to remove much of the noise floor, and every 4 adjacent frequencies were averaged to increase the spectral degrees of freedom (reduce noise). The resulting spectra span 0.0078 Hz to 0.49 Hz in 32 frequency bins (Figure 5.3).

Within the analysis period (Figure 5.1) there were 657 hourly pressure spectra (3 sites × 219 spectra) during which DAS was also recording. Each pressure spectrum represents an independent realization of the sea surface elevations within that hour. Since ocean wave statistics are expected to be stationary for several kilometers in moderate and ice-free conditions, DAS strain rate spectra from 1 km of channels centered on each site were calibrated to the measured pressure spectrum within each hour. Each channel makes an independent strain rate measurement, and water depth, burial depth, and seabed characteristics may vary across channels at a given site. A total of 40,077 strain rate spectra (61 channels × 3 sites × 219 spectra) were used in the analysis.

The hourly DAS and mooring observation pairs form a dataset of features and targets used to develop a model for converting DAS-measured strain spectra (features) to seafloor pressure spectra (targets). The dataset was partitioned into disjoint train and test subsets using the data gap as a natural split point. Data prior to the data gap, from 24 August 04:00Z to 30 August 00:00Z,

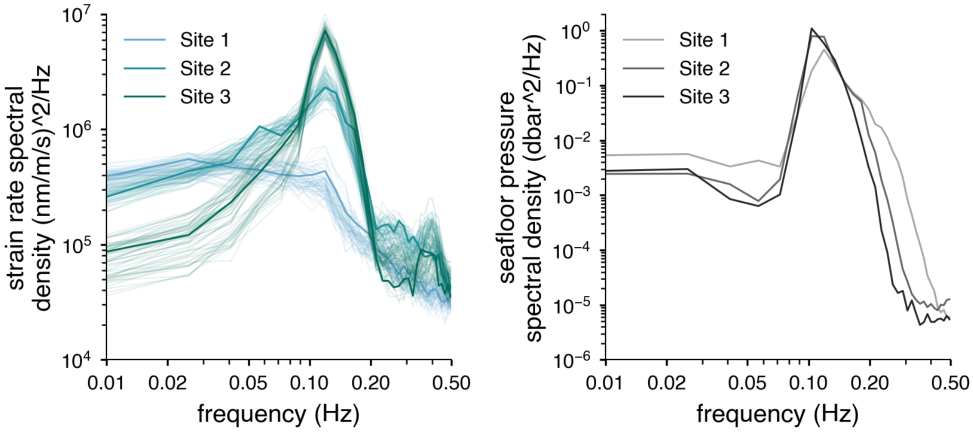

Figure 5.3: (Left) Strain rate spectra and (right) seafloor pressure spectra at all three sites on 28 August 00Z. In the left panel, lighter traces are individual strain rate spectra from 1 km of DAS channels centered on each site, and bold traces are strain rate spectra at the channel nearest to each mooring site (approximate along-cable distances of 9.28 km, 20.00 km, and 29.47 km).

were designated for training at all three sites. Data past the gap, from 17 September 17:00Z to 20 September 19:00Z, were used for testing. The resulting train-test split is approximately 65-35%. Both subsets contain comparable ranges of wave heights and periods (Figure 5.1). The test subset was withheld throughout the entire model training and selection process to provide an unbiased estimate of the best-performing model's performance on unseen data.

5.2.3 Median transfer function

Previous work has demonstrated the effectiveness of an empirically-derived transfer function for estimating surface wave properties from DAS-measured strain or strain rate (Smith et al., 2023; Glover et al., 2024b). Ground-truth measurements of colocated seafloor pressure were used to estimate a transfer function, H, between strain rate spectra and seafloor pressure spectra:

$$H(t,f) = \frac{P(t,f)}{S(t,f)} \tag{5.1}$$

Where $P(t,f)$ and $S(t,f)$ are seafloor pressure and strain rate observations, respectively, collected over time, t, at a single location (channel). Transfer function estimates from many observations over time were reduced to a single, frequency-dependent function using a temporal median, $\widehat{H}(f) = \underset{t}{\operatorname{med}}\,[H(t,f)]$. Subsequent estimates of P were calculated as the product of $\widehat{H}(f)$ and newly-observed S.

Site-specific transfer functions were calculated from 1-km of DAS data centered on each site (61 channels per site) over the entire train period (Figure 5.4). The median of these transfer functions represent the $\widehat{H}(f)$ estimate for each site. Pressure spectra were then computed from S at each channel and averaged over all 61 channels to obtain time series predictions at each site. We found this was equivalent to computing the temporal median at each channel, and then averaging predictions over channels. Over the 5.8-day period, individual transfer functions span approximately two decades of spectral density, which is consistent with prior estimates (Glover et al., 2024b). For instance, at Site 1, peak transfer function values range from $1.2 \cdot 10^{-7}$ to $1.1 \cdot 10^{-5}$ and have a standard deviation of $1.5 \cdot 10^{-6}$. Median transfer functions have similar shapes across sites, however site 1 has the largest dynamic range (Figure 5.4A).

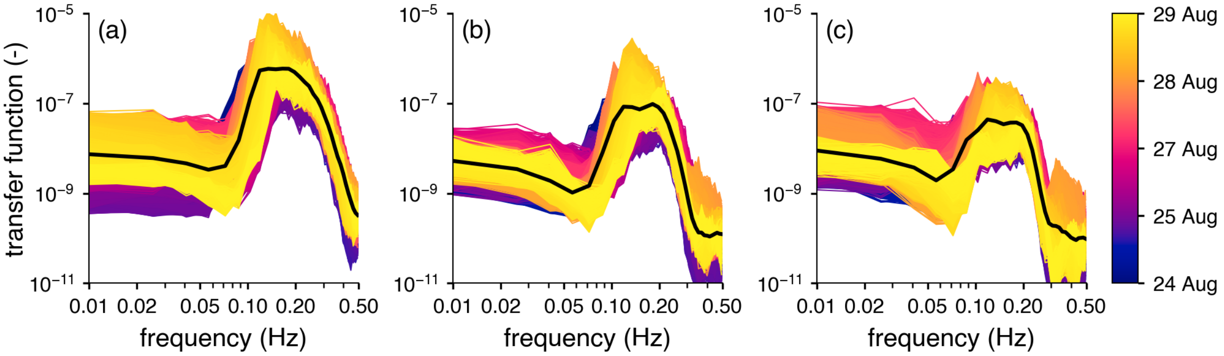

Figure 5.4: Spectral transfer functions (ratio of pressure to strain rate spectral density, Equation 5.1) calculated from 1-km of channels centered on Sites 1, 2, and 3 (a, b, and c). Black lines represent the median transfer function, $\widehat{H}(f)$. Transfer functions were calculated using spectral pairs only from the training period.

5.2.4 *Spectral neural network*

Variations in pressure-to-strain transfer functions over time suggest a potentially nonlinear relationship between strain rate spectra and seafloor pressure spectra. Here we explore the use of a fully connected neural network to map $S(f)$ to $P(f)$. Inputs to the network include strain rate spectral densities at 32 frequencies, water depth, and approximate cable burial depth (34 total features). The network contains two hidden layers of independent size. Each hidden layer is followed by a rectified linear unit (ReLU) activation function, which introduces nonlinearity into the network (Agarap, 2019). Dropout is applied after each layer as regularization mechanism, which helps to avoid overfitting to the training dataset. The outputs of the network are pressure spectral density predictions at 32 frequencies.

Both input and target spectra, S and P, were log-transformed to compress their dynamic range. We also find that a log-transformation prevents the network from predicting negative values when pressure spectral densities are small (e.g., on $O(10^{-5})$ as in Figure 5.3). Log-transformed input and target spectral densities were normalized per-frequency using the minimum and maximum values at each frequency (min-max scaling) such that inputs were mapped to the domain $[0, 1]$. Water depth and cable burial depth were also normalized using their respective ranges. Per-feature minima and maxima were determined strictly from the training subset to prevent information leakage to the validation and test subsets.

A per-frequency, mean squared error-based (MSE) loss function was used for model training. To avoid an over-weighting of the highest frequency, but lowest energy, portions of the spectra (due to the log transform), the total loss was computed as the weighted sum of log-transformed and linear (non-transformed) errors:

$$\begin{aligned} L_{\log}\left(\widehat{P}, P\right) &= \mathrm{MSE}\left(\log \widehat{P},\ \log P\right) \\ L_{\text{linear}}\left(\widehat{P}, P\right) &= \mathrm{MSE}\left(\widehat{P}, P\right) \\ L_{\text{total}}\left(\widehat{P}, P\right) &= \alpha\, L_{\log} + (1-\alpha)\, L_{\text{linear}} \end{aligned} \tag{5.2}$$

Where $\widehat{P}$ are the predicted pressure spectra and α is a hyperparameter used to balance the two loss components. A non-transformed normalization was computed and applied such that inputs to both $L_{\log}$ and L_{linear} were normalized using min-max scaling.

The spectral neural network was trained in epochs using the AdamW optimizer with nonzero weight decay (L_2 regularization) (Loshchilov and Hutter, 2019). Bayesian hyperparameter optimization (Optuna) was used to determine the hidden layer sizes (8, 16, 32, or 64), dropout probability (capped at 30%), α in Equation 5.2, batch size, and AdamW parameters (Akiba et al., 2019). Training data from 28 August 18:00Z to 30 August 00:00Z were used for validation. Since the magnitude of the loss varies with α, a per-frequency MSE calculated using linear $\widehat{P}$ and P was used as an evaluation metric for model selection.

The selected model has hidden layer sizes of 16 and 32 (first and second layer) and a dropout probability of 8%. It was trained for up to 200 epochs with a 32-sample batch size and $\alpha = 0.46$.

5.2.5 Frequency-wavenumber convolutional neural network

The median transfer function and spectral neural network models operate on spectra from individual channels. Neither model leverages the spatial resolution of DAS, in particular signals from incident waves as they are measured across neighboring channels (e.g., Figure 5.2a). The use of this information may help to distinguish ocean waves from other noise common to DAS data. We introduce a final model that maps frequency-wavenumber (f-k) strain rate spectra to pressure spectra using a convolutional neural network (CNN). The model's architecture is adapted from *im2spec*, a convolutional encoder-decoder network developed in the materials science domain (Kalinin et al., 2021; Roccapriore et al., 2021). For instance, Roccapriore et al. (2021) used this architecture to predict electron energy loss spectra from scanning transmission electron microscope images of fluorine and tin-doped indium oxide nanocrystal arrays.

Encoder-decoder models learn a low-dimensional vector, or "latent" space, between inputs and outputs. Inputs are processed into the latent space via the encoder, and outputs are generated from the latent space by the decoder. The goal is to learn a latent space that contains meaningful information connecting the inputs and outputs while rejecting irrelevant information, such as noise. Latent space components are similar to principle components (or empirical orthogonal functions), except that the former are the result of a nonlinear transformation and are not orthogonal nor ordered by contribution (Ladjal et al., 2019). (Here, the decoding of the latent space also does not reproduce the inputs, as would an autoencoder or reconstruction from principle components.)

Inputs to the model are 32×32 images of strain rate f-k spectra. Outputs are 1D pressure spectra at 32 frequencies, which is the same as the previous two models (pressure f-k spectra cannot be generated from a point-measurement for use as targets). The encoder contains a series of 2D convolutional layers which operate on successive forms of the input images. Output from the encoder is compressed into a latent vector via a fully connected layer, where each entry of the latent vector is a latent dimension. The decoder contains a series of dilated 1D convolutional layers which expand the latent space vector into a pressure spectral density prediction.

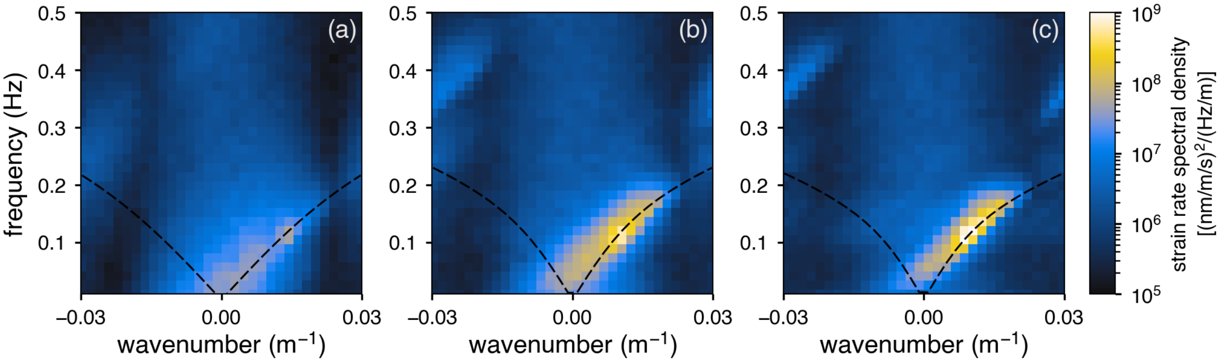

Figure 5.5: Strain rate f-k spectra centered on Sites 1, 2, and 3 (a, b, and c) on 24 August 16Z. Energy in the $(f, +k)$ plane is directed onshore, and energy in the $(f, -k)$ plane is directed offshore. Black dashed lines show the dispersion relationship (Equation 5.3) for estimated wave directions $|\theta| = 33^\circ$, 29°, and 16° at Sites 1, 2, and 3, respectively.

Strain rate f-k spectra were estimated using two-dimensional arrays of raw strain rate from 2 km of DAS channels collected over 30-min (Figure 5.5). The temporal duration was reduced from the prior two models (60-min), since f-k spectra also include spatial statistics. Data were segmented along the time axis into 600-point (300-s) segments with 50% overlap and were tapered with a 2D Hann window function prior to computing 2D Fourier transforms and averaging. Frequencies above 0.5 Hz were trimmed, and every four frequencies and three wavenumbers were merged. Final strain rate f-k spectra were interpolated onto a 32×32 grid of frequencies from 0.01 to 0.50 Hz and wavenumbers from $\pm$ 0.00096 to 0.03 m^{-1}, where negative wavenumbers indicate offshore wave propagation (Figure 5.5). Note that strain rate frequency spectra are recoverable from f-k spectra via integration along the wavenumber axis.

The strain rate f-k spectra show signatures of the ocean surface gravity wave dispersion relationship:

$$\omega^2 = g\left(\frac{k_x}{\cos\theta}\right)\tanh\left(\frac{k_x h}{\cos\theta}\right) \tag{5.3}$$

where $\omega = 2\pi f$ is angular frequency, g is the acceleration of gravity, h is water depth (positive-down), and k_x is the along-cable component of the wavenumber vector for waves traveling at an oblique angle θ relative to the cable ($k_x = |\mathbf{k}| \cos\theta$, where $\mathbf{k}$ is the 2D wavenumber vector). The f-k spectra also reveal signatures off of the ocean wave dispersion curve. Thus, a motivation for using an encoder-decoder architecture is that the latent space might isolate energy along the dispersion curve from background noise or other signals not directly related to ocean surface waves. While f-k spectra could be pre-filtered to exclude energy that does not follow the dispersion relationship, these extrinsic signatures may still be useful for the model, e.g., variations in energy may correspond to changes in burial depth or seafloor coupling across channels.

The f-k CNN model was trained on 837 pairs of half-hourly f-k spectrum images and pressure spectra at all three sites from 24 August 04:00Z to 30 August 00:00Z (the same time period used to train the spectral neural network). Both images and spectra were provided to the model in linear space (no transformation). Input images were normalized by the min and max energy density at any frequency-wavenumber pair across all images, and pressure spectra were normalized by the per frequency min and max across all spectra. Unlike the spectral neural network, neither water depth nor approximate cable burial depth were provided as inputs. Model weights were optimized using AdamW and a per-frequency MSE loss calculated from predicted and observed pressure spectra (equivalent to L_{linear} in Equation 5.2). The quantity and output size of the encoder's 2D convolution layers, the output size of decoder's 1D convolution layers, the number of latent dimensions, batch size, and optimizer parameters were determined via a hyperparameter search using training data from the same 28 August 18:00Z to 30 August 00:00Z period as validation. This model was evaluated on the remaining 477 of the 1,314 total image-spectra pairs. Model specifications included in the hyperparameter search space were intentionally kept small to limit the total number of model parameters (e.g., number of encoder and decoder filters ≤ 32 and number of latent dimensions between 1 and 6). The use of a smaller model was an effort to prevent overfitting to the relatively small dataset of image and spectrum pairs.

The selected model has an encoder with three 2D convolution layers, where each layer has 4 filters, a 3×3 kernel, and subsequent ReLU activation and batch normalization (Figure 5.6). A fully connected layer reduces the encoder output to a 4-dimensional latent space. The decoder consists of four 1D convolutional layers, each with 16 filters, a kernel size of 3, and subsequent ReLU

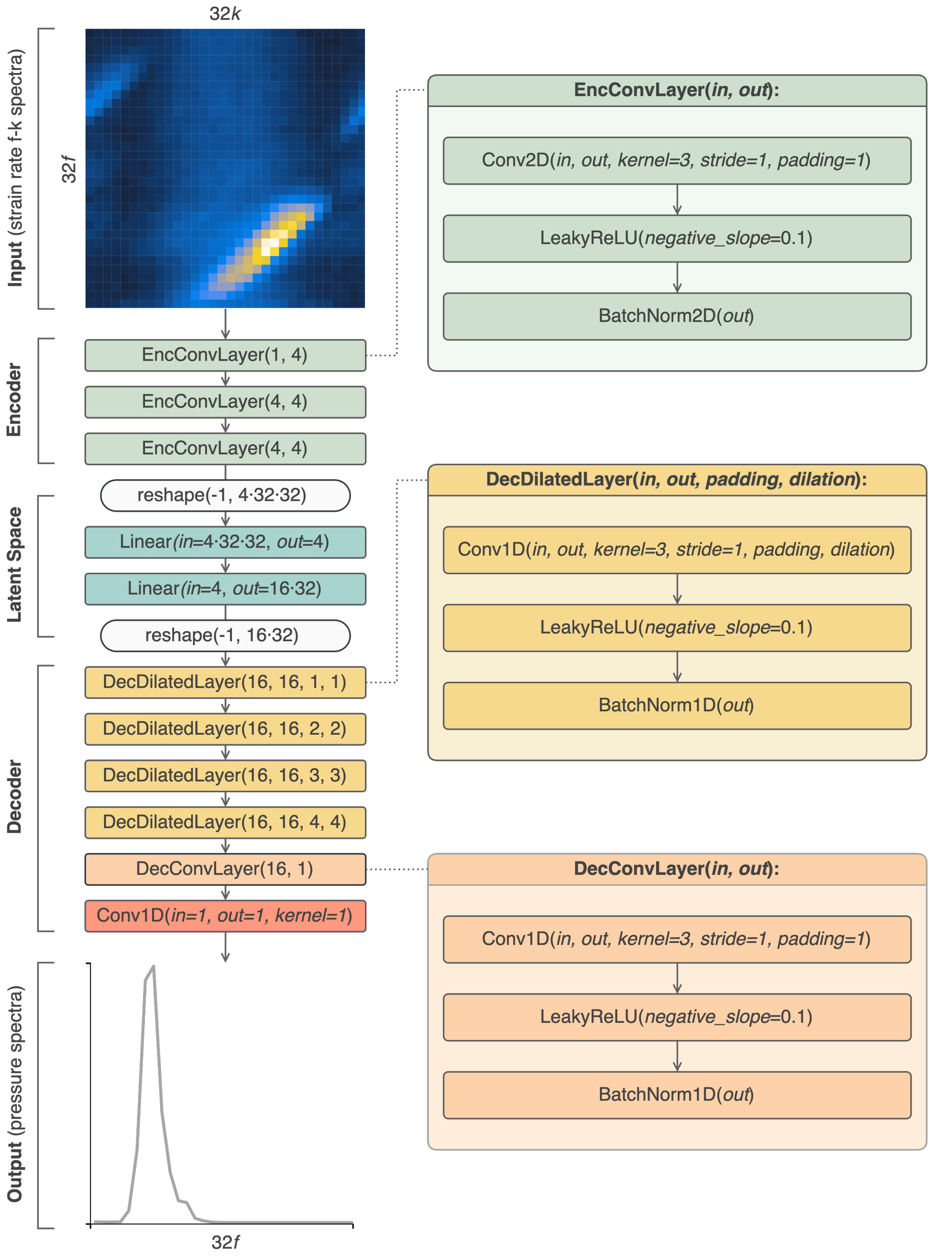

Figure 5.6: Schematic of the f-k CNN model. Layer names and argument orders follow PyTorch 2.7.1 conventions. Custom layer groups are defined in panels on the right. Model architecture is adapted from the *im2spec* network described in Kalinin et al. (2021) and Roccapriore et al. (2021).

activation and batch normalization. Each of the four 1D convolutional layers have increasing amounts of dilation and padding, from 1 (closest to latent vector) to 4 (furthest from latent vector). The dilated convolution layers are followed by a final 1D convolutional layer which reduces the 16 filters to a single output filter.

5.3 Results

Here we compare the skill of the three data-driven models for estimating seafloor pressure spectra and bulk wave parameters from DAS-measured strain rate. Site-specific median transfer functions (Median TF) are used as a benchmark from which the spectral neural network (Spectral NN) and f-k spectra convolutional encoder-decoder neural network (f-k CNN) are evaluated. Unlike the median TF, the Spectral NN and f-k CNN models were trained on all three sites simultaneously (i.e., they are not site-specific).

5.3.1 Predictions at each site

Seafloor pressure spectral densities were predicted at all three sites over the entire analysis period (inclusive of the train and test subsets). Example spectra at two timestamps, drawn from energetic periods within the train and test subsets, demonstrate that each model generally captures the shape of the target mooring spectra, including the location of the peak (Figure 5.7). In all cases, Median TF predictions have lower energy levels near the centroid of the spectrum, but capture the spectral tail (frequencies past the peak) exceptionally well (e.g., Figure 5.7f). Spectral NN pressure spectra contain more energy and generally have accurate shapes, but occasionally miss peaks or under estimate total energy (e.g., Figure 5.7e). Predictions from the f-k CNN model capture energy levels and shape near the spectral peak well, but tend to overestimate energy within the tail (e.g., Figure 5.7e and f).

Seafloor pressure variance was calculated from each spectral prediction to provide a measure of total energy (Figure 5.8). Variance was calculated as the zeroth spectral moment integrated over frequencies from 0.05 Hz to 0.5 Hz to isolate contributions from surface gravity waves. Median TF predictions capture low energy trends at some sites (e.g., Site 3), but have a tendency to

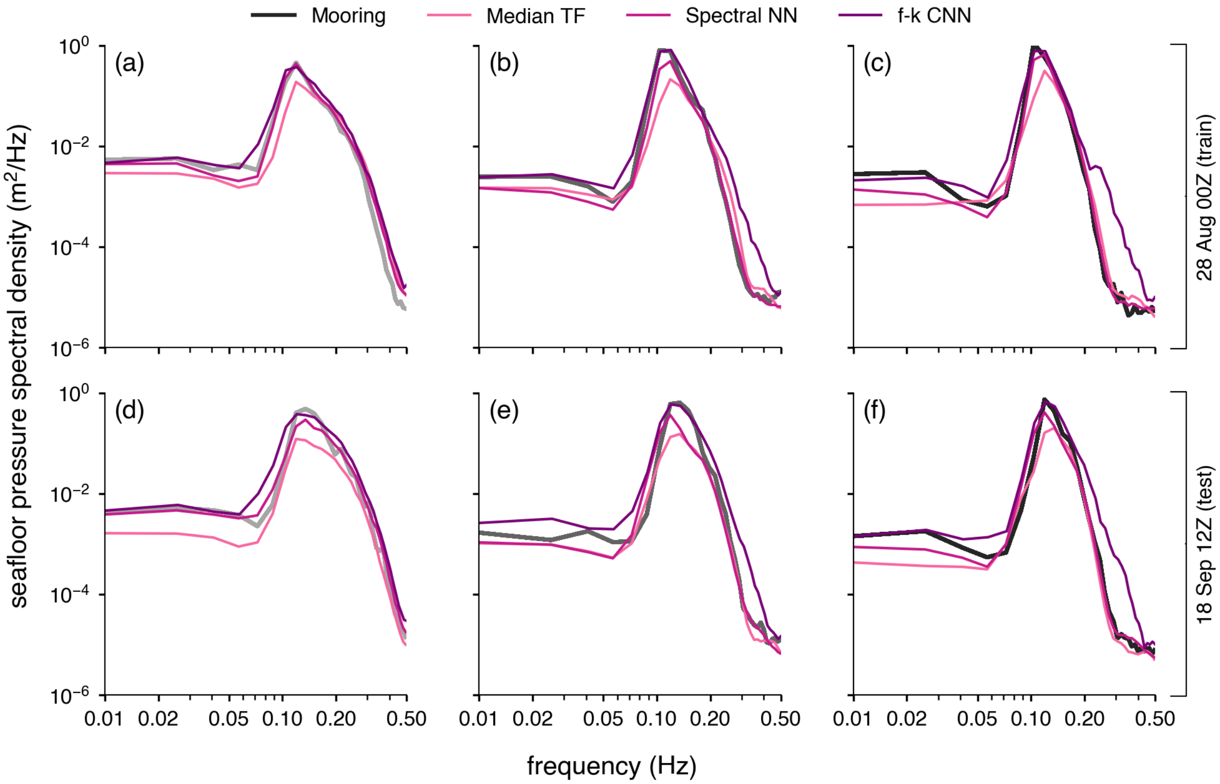

Figure 5.7: Seafloor pressure spectral density predictions at an example train timestamp (28 August 00Z) at Sites 1, 2, and 3 (a, b, and c) and at an example test timestamp (28 August 00Z) at Sites 1, 2, and 3 (d, e, and f). Heavy lines represent mooring observations (targets) at each site.

saturate at pressure variances around 0.01 to 0.2 m^2. Notably, the Median TF performs poorest at the shallowest site, Site 1 (Figure 5.8a). Spectral NN predictions are better, but this model still misses peaks in variance during energetic periods. The f-k CNN captures trends well during both low and high energy periods, but is occasionally biased high relative to the target mooring observations (e.g., the test period of Figure 5.8b).

Pressure spectra were corrected to surface elevation spectra, $E(f)$, using linear wave theory (e.g., Bishop and Donelan, 1987):

$$E(f) = P(f)\left(\frac{\cosh(kh)}{\cosh(kz_s)}\right)^2 \tag{5.4}$$

where k is wavenumber estimated from Equation 5.3 with $\theta = 0$, and z_s is the height of the pressure sensor above the bottom (here, we assume $z_s \approx 0$). Depth corrections are largest at high frequencies, which are attenuated most rapidly. Values of the pressure-to-surface transfer function (cosh ratio term) were cut off above 25 $\mathrm{m}^2/\mathrm{m}^2$ to prevent the introduction of erroneous spectral tail shapes at deeper sites. At site 3, this constraint truncates spectra above frequencies of 0.2 Hz. In practice, an equilibrium tail, $E(f) \sim f^4$, can be appended to the spectra to extrapolate beyond the cutoff frequencies (e.g., as done by Smith et al. (2023)).

Significant wave heights were calculated from estimated surface elevation spectra as $4\sqrt{m_0}$, where m_0 is the zeroth moment of $E(f)$ integrated from 0.05 Hz to 0.5 Hz. Trends in model-predicted significant wave height are similar to pressure variance (Figure 5.9). Significant wave height errors are compressed relative to variances, since significant wave height is proportional

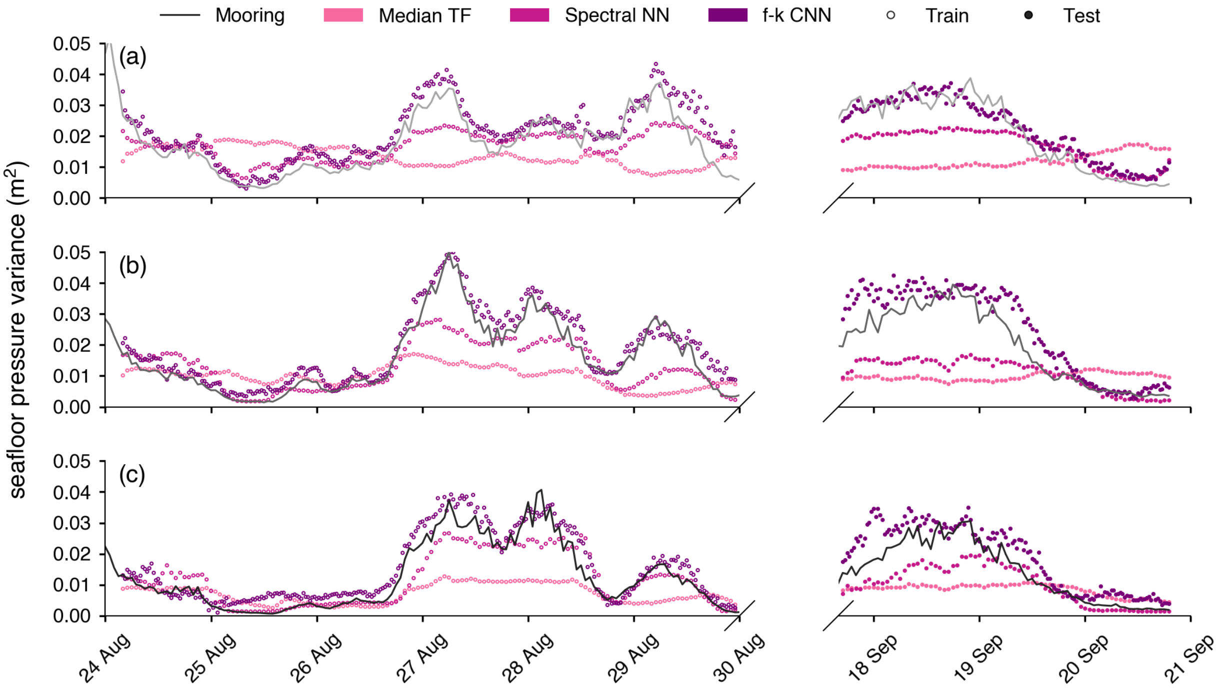

Figure 5.8: Seafloor pressure variance predictions at Sites 1, 2, and 3 (a, b, and c). Solid lines represent mooring observations (targets) at each site. In each plot, open circles indicate train data, and filled circles indicate test data.

to the square root of variance.

Energy periods were calculated from pressure spectra as m_0/m_1, where m_0 and m_1 are the zeroth and first moments of $P(f)$ integrated from 0.05 Hz to 0.5 Hz. Period prediction skill is evaluated on energy periods derived from pressure spectra, rather than surface elevation spectra, since the former do not have to be truncated at high frequencies in large relative depths. (Though energy periods derived from pressure spectra will be longer, since short period waves are attenuated at depth.) In contrast to pressure variance and significant wave height, all models produce similar energy period predictions that agree well with mooring observations. Two exceptions are Median TF-predicted energy periods at Site 1, which lack shape despite variation in mooring-measured periods (Figure 5.10a), and larger errors in f-k CNN-predicted periods at

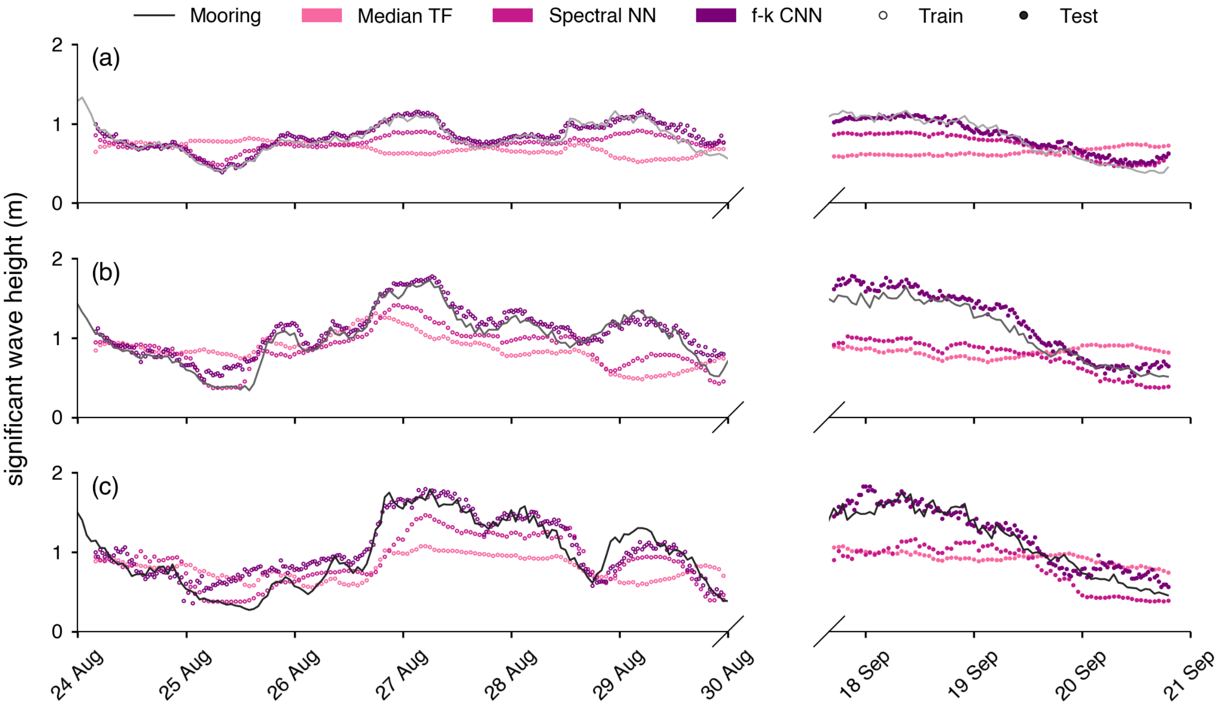

Figure 5.9: Significant wave height predictions at Sites 1, 2, and 3 (a, b, and c). Solid lines represent mooring observations (targets) at each site. In each plot, open circles indicate train data, and filled circles indicate test data.

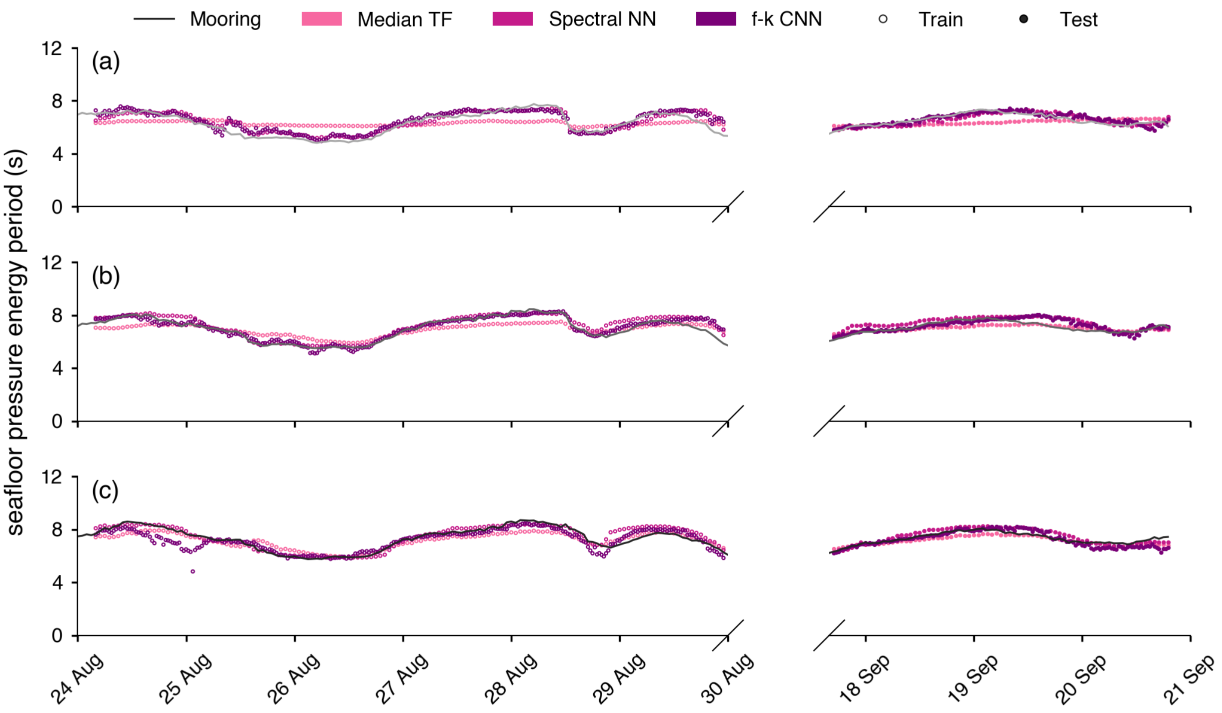

Figure 5.10: Seafloor pressure energy period predictions at Sites 1, 2, and 3 (a, b, and c). Solid lines represent mooring observations (targets) at each site. In each plot, open circles indicate train data, and filled circles indicate test data.

Site 3 around 24-25 August (Figure 5.10c). The latter is likely due to f-k CNN tail artifacts, shown in Figure 5.7, which have a larger impact on energy period in low energy conditions.

Predicted versus observed spectral and bulk variables at all three sites are compared directly in Figure 5.11 and Table 5.1. Both machine learning-based models perform better than the Median TF benchmark in significant wave height prediction skill: root mean squared errors (RMSE) for the Spectral NN (0.3 m) and f-k CNN (0.15 m) models decreased 27% and 63% relative to the Median TF (0.41 m), respectively. Median TF and Spectral NN models generally underestimate wave heights, with mean bias errors (MBE) of -0.18 m and -0.2 m. This low bias predominantly occurs in energetic conditions (Figure 5.11b). In contrast, f-k CNN significant wave height predictions are biased high (MBE = 0.008 m). Pressure spectral density predictions from the Median

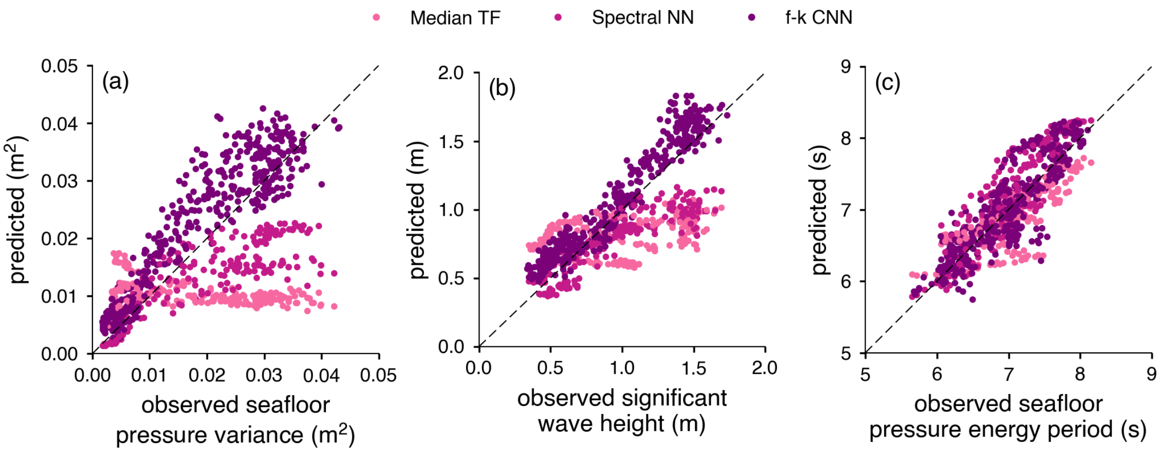

Figure 5.11: Predicted versus observed (a) seafloor pressure variance, (b) significant wave height, and (c) seafloor pressure energy period at all three sites. Data are from the test subset only.

Table 5.1: Comparison of model performance at all three sites. Errors are calculated using predictions from the test subset only. Pressure spectral density regression metrics (MBE, RMSE, and MAE) are averaged over frequency, and the similarity metric (Cos Sim.) is averaged over time.

		Median TF	Spectral NN	f-k CNN
pressure spectral density	MBE (m^2/Hz)	-0.017	-0.012	0.008
	RMSE (m^2/Hz)	0.095	0.078	0.047
	MAE (m^2/Hz)	0.027	0.022	0.016
	Cos Sim. (–)	0.92	0.86	0.89
pressure variance	MBE (m^2)	-0.008	-0.006	0.004
	RMSE (m^2)	0.015	0.01	0.006
	MAE (m^2)	0.012	0.007	0.005
significant wave height	MBE (m)	-0.18	-0.2	0.11
	RMSE (m)	0.41	0.3	0.15
	MAE (m)	0.36	0.24	0.12
	MAPE (–)	39%	23%	15%
energy period	MBE (s)	-0.14	0.16	0.04
	RMSE (s)	0.37	0.43	0.29
	MAE (s)	0.29	0.35	0.21
	MAPE (–)	4%	5%	3%

MBE = mean bias error; RMSE = root mean squared error; MAE = mean absolute error;
MAPE = mean absolute percentage error; Cos Sim. = cosine similarity

TF model achieve the highest cosine similarity, a unitless measure of spectral shape similarity, at 0.92, as compared to the Spectral NN (0.86) and f-k CNN (0.89) models. This suggests the Median TF is generally best at capturing the correct spectral shape, but misses overall energy levels (as evidenced by its comparatively poor significant wave height performance). Spectral NN energy period RMSE increased 16% relative to the Median TF (RMSE of 0.43 s compared to 0.37 s), but f-k CNN errors decreased 22% (0.29 s compared to 0.37 s). The f-k CNN has the best performance across all of the considered regression evaluation metrics. This model's latent space is explored in the Appendix.

5.4 Discussion

5.4.1 Temporally- and spatially-varying pressure-strain relationship

Frequency-dependent strain-rate-to-pressure transfer functions vary in time (Figure 5.4), consistent with previous results (Glover et al., 2024b; Smith et al., 2023). The Oliktok point cable is trenched approximately 2-4 m, and the full mooring record does not indicate any exceptional wave events occurred over the analysis period, suggesting temporal variations are not due to drastic changes in burial depth. Fiber strain has also been shown to have a linear dependence on temperature (Sidenko et al., 2022), but we do not observe a consistent dependence of transfer function magnitude on near-bottom water temperatures; water temperatures recorded by the moorings range from -0.5 to 4 C and change near-monotonically in time, with the warmest temperatures observed at Site 1 early in the analysis period. Another possibility is that DAS strain is induced by along-cable pressure gradients (i.e., $\partial P/\partial x$), such that variations in wave direction yield different strain responses. Since f-k spectra (Figure 5.5) encode directional information through Equation 5.3, this could explain why the f-k CNN outperforms the other models (which have no directional information).

The bulk strain rate and pressure relationship is also significantly different along-cable (Figure 5.12). At Sites 2 and 3, band-passed strain rate and seafloor pressure variances (0.05 Hz to 0.5 Hz) have a positive linear dependence when pressure variance is low, but appear to saturate at higher pressures (Figure 5.12b–c). At Site 1, the strain rate variance and pressure variance relationship is linear but inversely proportional (Figure 5.12a). That is, larger variations in pressure correspond to smaller variations in strain. Changes in the strain-pressure relationship correlate well with wave direction at Sites 2 and 3. Saturation at these sites tends to occur when waves travel at an oblique angle relative to the cable axis (Figure 5.12c). Wave direction is approximated by fitting dispersion curves (Equation 5.3) to observed f-k strain rate spectra. Drastic differences in cable response across the three sites may be due to differences in burial depth (approximately 2 m at Site 1 versus 4 m at Sites 2 and 3), along-cable differences in cable-to-seabed coupling, and differences in sediment composition. Strain-pressure relationships observed on the Oliktok cable are in stark contrast to studies that report a highly linear relationship in cables elsewhere across a wide range of conditions (e.g., Meulé et al., 2024).

These factors—variations in the pressure-strain relationship over time and space—help explain why the Median TF struggles to predict accurate significant wave heights (Figure 5.9). This model's skill is weakest in high energy conditions, where the slope of the strain-pressure relationship abruptly flattens (Figure 5.12c), and at Site 1, where strain rate variance is inversely proportional to pressure variance (Figure 5.12a). When empirically mapping strain rate spectra

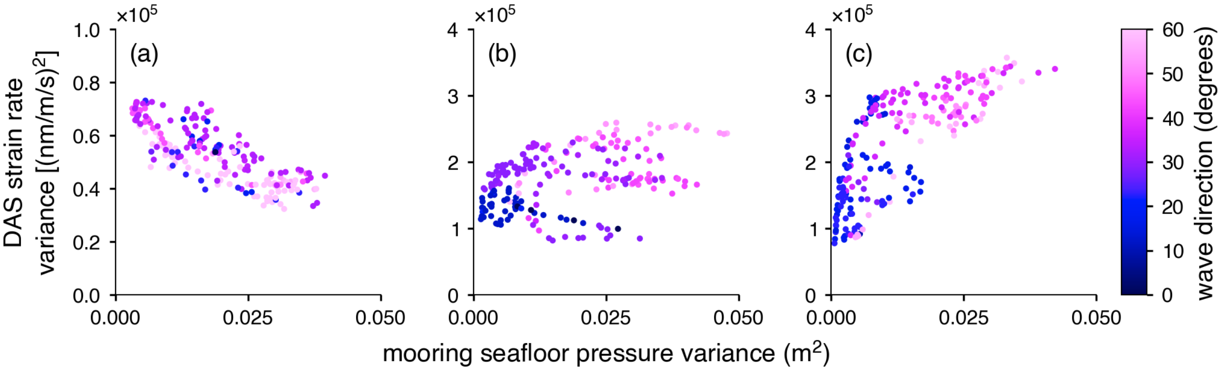

Figure 5.12: Strain rate variance versus observed pressure variance, colored by wave direction, at Sites 1, 2, and 3 (a, b, and c). Wave directions have a left-right ambiguity relative to the cable axis. Note offset multipliers on each y-axis.

to pressure spectra, these complex relationships necessitate the use of a model that can capture nonlinear relationships (such as the Spectral NN or f-k CNN models). We note that the 5.8 days used to estimate the Median TF is shorter than the optimal 10–15 day calibration period suggested by Glover et al. (2024b) based on data from Duck, NC, though this duration is comparable with the 5-day period used by Smith et al. (2023) on the Oliktok cable, albeit over a smaller dynamic range (H_s of 0–0.5 m compared to 0–2 m here). A longer dataset collected on the Oliktok cable is needed to evaluate whether a larger training dataset improves Median TF performance, though this may suggest machine learning methods are able learn the dependence with a shorter training window than previous empirical methods.

5.4.2 Along-cable predictions

Predictions evaluated at Sites 1, 2, and 3 test each model's interpolation skill, since the train and test subsets contain similar distributions of pressure and wave parameters (assuming external factors such as water depth and burial depth do not change drastically between train and test periods). A different, and much harder problem, is application of the models to channels between sites. This tests each model's ability to extrapolate outside of the conditions used to train the models, since these channels may have different stress responses due to varying seabed composition, burial depths, and cable coupling.

All models were used to estimate $P(f)$ at all 1,656 channels along the 27.1 km of cable used in the analysis. Since the f-k CNN model processes channels in 2-km segments, along-cable spectra were calculated in sliding windows along the cable with 50% overlap. The Median TF and Spectral NN models were applied to the average strain spectra in each window. This produces much smoother predictions than if the these models had been applied to spectra at individual channels, but at the cost of smearing out signals over the 2-km window.

Wave heights predicted by the f-k CNN match observed wave heights at each site, but fluctuate considerably between sites (Figure 5.13). Median TF and Spectral NN predictions are predominantly low relative to the mooring sites and have less variation with distance than f-k CNN predictions. Exceptions are the Median TF predictions near Site 1, where this model predicts a

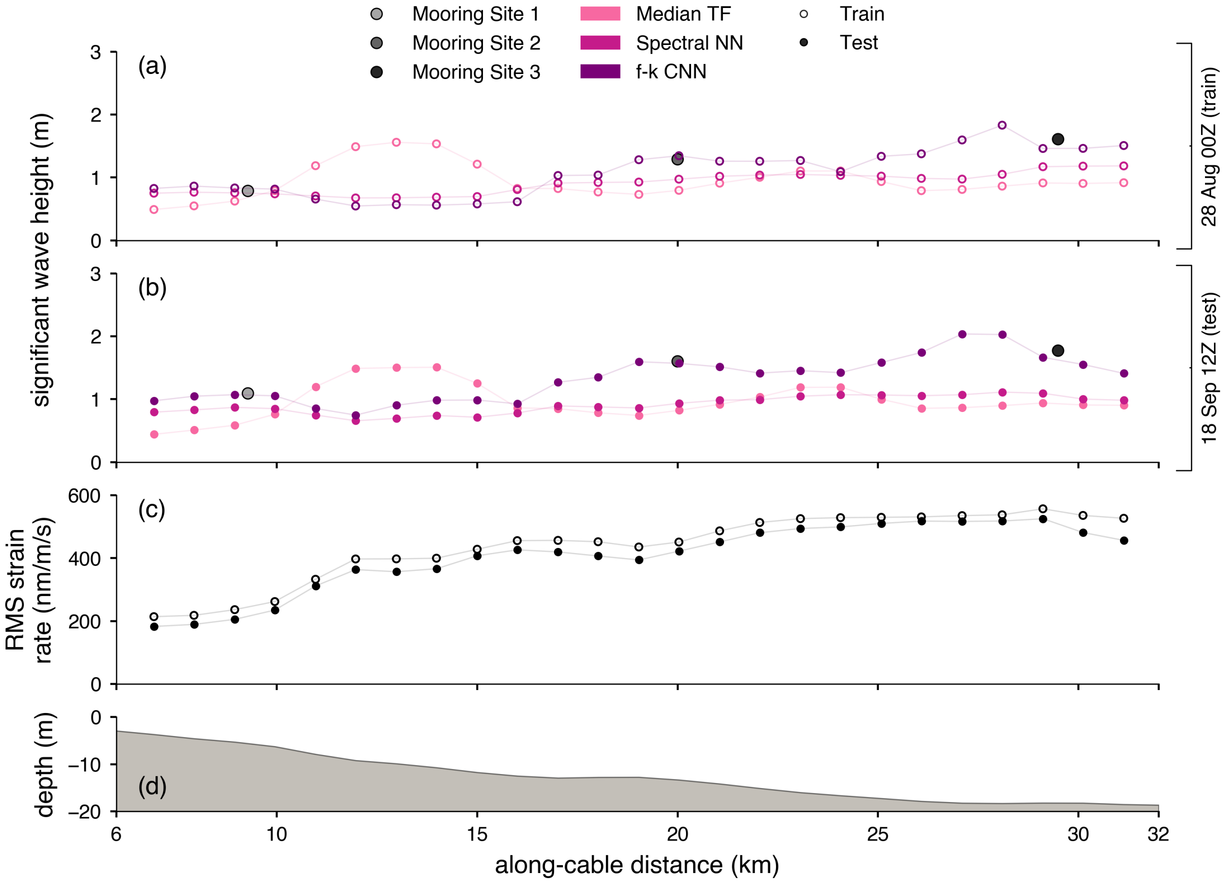

Figure 5.13: Along-cable significant wave height predictions at (a) an example train timestamp (28 August 00Z), and (b) an example test timestamp (18 September 12Z). Root mean square strain rate at each timestamp is shown for reference in (c). In each plot, open circles indicate train data, and filled circles indicate test data.

jump in wave height between along-cable distances 10 and 15 m. In all cases, predicted wave heights deviate from the null assumption that wave heights between channels are a linear interpolation of sites 1, 2, and 3. Observed root mean square (RMS) strain rates also show variation with distance (Figure 5.13c), however it is difficult to infer wave height from strain rate response since there is a nonlinear, and sometimes inverse, relationship between the two variables (Figure 5.12). Additional mooring sites, or other wave height estimates (e.g., from a regional wave model), are required to quantify along-cable prediction skill.

5.4.3 *Spectral neural network trained on individual sites*

A Spectral NN model trained on all three sites simultaneously is only marginally better at spectral and bulk variable prediction than the Median TF. When the Spectral NN model is instead trained on individual sites, significant wave height prediction skill is improved (Figure 5.14). This is likely because adjacent clusters of channels have similar, but potentially still nonlinear, pressure-strain relationships that can be captured by medium-complexity models. Thus, fully-connected neural networks can be a sufficient tool if only regional estimates are needed along a DAS cable. However, it is less likely that the individually-trained models will generalize well over the rest of the cable, which is required to produce along-cable predictions (as in Figure 5.13).

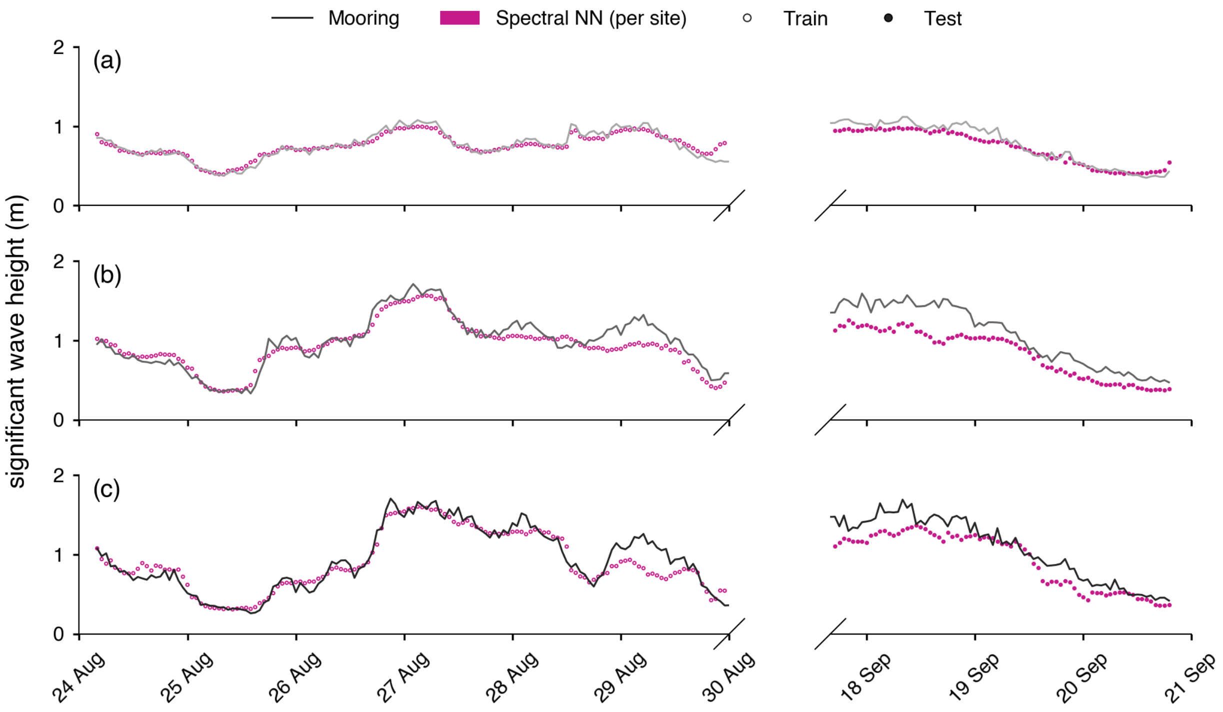

Figure 5.14: Significant wave height predictions from Spectral NN models individually trained at Sites 1, 2, and 3 (a, b, and c).

5.4.4 Generalization to other cables

A drawback of a machine learning-based calibration is that the trained model weights are unlikely to transfer to other cables. Cables with different properties, including cable composition, burial depth, and coupling, will have distinct energy levels and transfer functions (Glover et al., 2024a). The model architecture can be easily adapted to other cables used for DAS, provided sufficient ground truth pressure spectra are available for use as training data. The f-k CNN does not require any additional inputs aside from f-k strain rate spectra, which can be readily computed from most DAS datasets. Both training and inference can be performed in reasonable time (e.g., hours) and without GPUs. The f-k CNN and spectral NN models were kept small (< 25k parameters), though complexity could be added if needed and if more training data is available.

Training a global model (i.e., a model that can be applied to many channels along a cable) will likely require more than one site to use as a target. Multiple sites distributed along a cable are necessary for capturing variations in along-cable response (Section 5.4.1). Other estimates of seafloor pressure, such as pressure spectra inferred from surface elevation spectra (wave spectra), can be used as targets. For instance, Smith et al. (2023) use a moored wave buoy as ground truth by converting surface elevation spectra to seafloor pressure spectra by applying the inverse of Equation 5.4. Alternatively, a model might be trained to predict surface elevation spectra directly (i.e., the relationship in Equation 5.4 can be learned implicitly). If spectral information is not required, it may also be possible to estimate bulk parameters, such as significant wave height and energy period, directly.

5.5 Conclusions

A 10-day dataset of submarine fiber-optic cable strain rate and ground truth seafloor pressure collected offshore of Oliktok Point, AK, demonstrates machine learning-based models can be adept at estimating pressure spectra via DAS when simpler methods (e.g., a median transfer function) are insufficient. Settings where the median transfer function method underperform are characterized by dynamic wave conditions at DAS sites with a varying pressure-strain relationship along the cable. The choice of architecture, features, and outputs chosen here are by no means exhaustive, and future work should pursue continued model exploration and improvement with an emphasis on along-cable prediction skill.

Acknowledgments

This material is also based upon work supported by the Link Ocean Engineering and Instrumentation Ph.D. Fellowship Program. DAS data collection was made possible by collaborations with Quintillion, Sandia National Laboratories (SNL), Robert E. Abbott (SNL), Christian Stanciu (SNL), and Michael G. Baker (SNL). SNL is a multimission laboratory managed and operated by NTESS under DOE NNSA contract DE-NA0003525. Mooring deployment was supported by NSF grant OPP 2214651.

Appendix

5.5.1 Frequency-wavenumber CNN latent space

The four dimensions of the trained f-k CNN model latent space are plotted against each other in Figure 5.15. Points in the latent feature space, which represent the f-k spectra used for training, were clustered using a Gaussian mixture model. Clusters generally correspond to distinct groups of points.

The mean of 80 f-k spectra nearest to the centroid of each cluster are compared to mean f-k spectra at the three sites in Figure 5.16. Given the visual similarities between mean f-k spectra from the three clusters and the three sites, a plausible interpretation is that the f-k CNN model's latent space contains an encoding of the individual sites. Under this interpretation, predictions at channels between training sites (e.g., along-cable predictions in Figure 5.13) are ideally an interpolation of sites 1, 2, and 3. We stress that no information identifying the site were provided to the model.

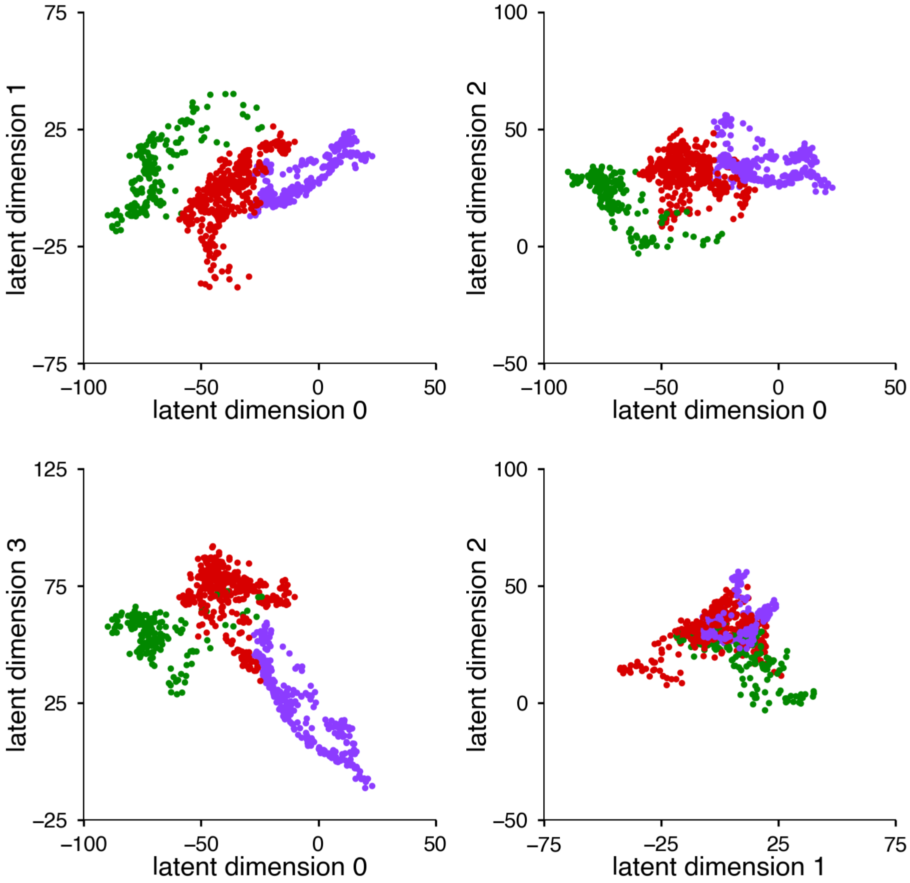

Figure 5.15: Clustered f-k CNN latent space.

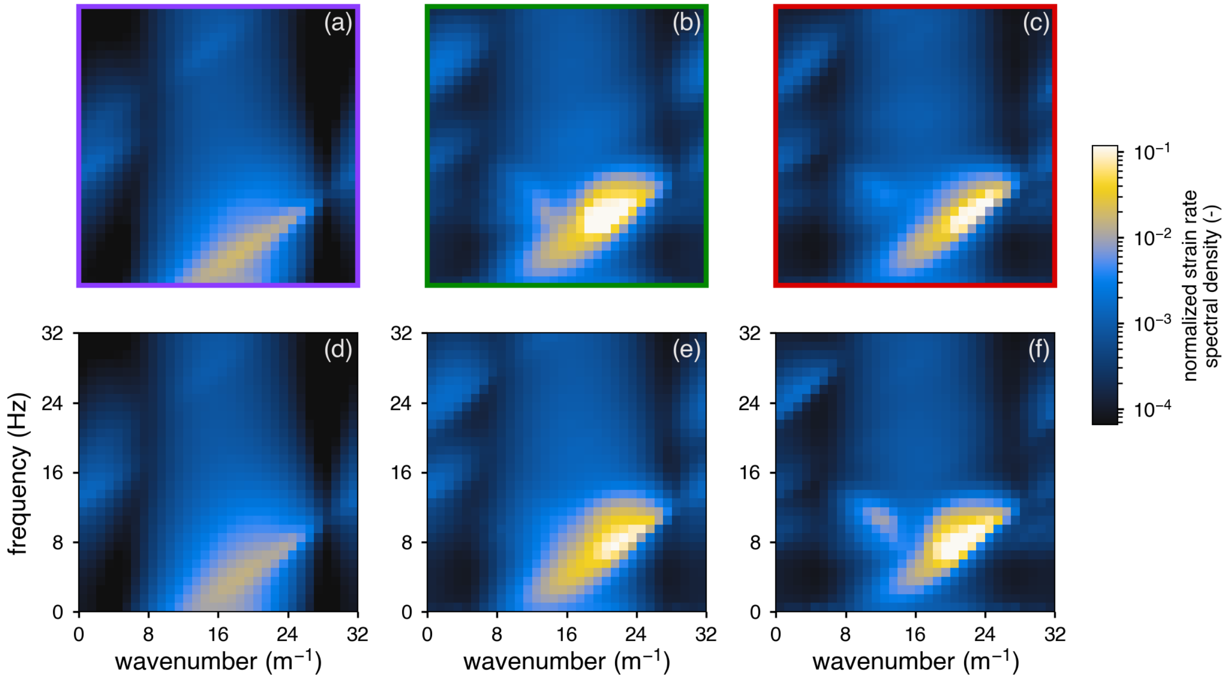

Figure 5.16: Mean of the 80 normalized f-k spectra nearest to the centroids of the three clusters (a, b, and c) and mean normalized f-k spectra at sites 1, 2, and 3 (d, e, and f). Border colors in the top row correspond to the clusters in Figure 5.15.

Chapter 6

CONCLUSIONS

6.1 Summary

Chapter 2, published as Davis et al. (2023b), uses drifting wave buoy data from hurricanes Ian (2022) and Fiona (2022) to characterize the evolution of the spectral tail and mean square slope (mss) of waves longer than 6 m. This chapter establishes the primary dependence of mss on wind speed in hurricanes, which is in agreement with the pioneering work of Cox and Munk (1954), and efforts that have followed, in moderate wind conditions (≤ 15 m s^{-1}).

Buoy observations show the dependence of mss on wind speed changes above 15 m s^{-1}. In high winds, increases in mss with wind speed are drastically reduced relative to moderate conditions (i.e., the wind speed dependence saturates). This trend persists through the highest wind speeds in the dataset, up to 54 m s^{-1}. The weakening of the primary mss dependence is coincident with changes in the measured wave spectra and underlying wavefield. At lower wind speeds, the spectral tail (energy at frequencies past the peak) follows the canonical "equilibrium" range form, whereby energy decays as frequency f^{-4} and energy input by the wind is balanced by nonlinear transfers and dissipation from breaking. Above 25 m s^{-1}, the equilibrium range is progressively narrowed, until the spectra are dominated by the "saturation" range (energy decays as f^{-5}). In this regime, wind input is balanced only by dissipation, suggesting wave breaking is ubiquitous and thereby limits wave slope.

Based on the theoretical connection between slope spectra and wind stress (e.g., Plant, 1982), the saturation of mss at high wind speeds is plausibly related to the qualitatively-similar drag coefficient saturation. A limitation on wave slope is indicative of increased wave breaking probability, which is one of the several proposed mechanisms for drag coefficient saturation (Takagaki et al., 2016). Mean square slope saturation may also be related to wave tearing, another dissipation mechanism theorized to reduce wave steepness at high winds (Troitskaya et al., 2012). Both mechanisms are consistent with the reduced growth in surface roughness with increasing wind speed implied by mean square slope saturation.

Chapter 3 (Davis et al., 2024a) uses data from the airborne Wide Swath Radar Altimeter (WSRA) inside several hurricanes to investigate the mss of waves as short as 0.2 m. The radar-derived, quasi-specular mean square slope measurements saturate at wind speeds above 25 m s^{-1}, consistent with buoy observations in Chapter 2. The difference of colocated buoy mss and WSRA mss are used to estimate the mss of waves between 0.2 m and 6 m. These mss estimates also saturate at high wind speeds, which suggest it is not just longer waves that reach a limiting steepness above 25 m s^{-1}, but also the short waves hypothesized to contribute significantly to wave-induced wind stress. A simple model for estimating the frequency dependence of the high frequency tail from colocated radar and buoy data is proposed. Estimates of the spectral tail shape derived from colocated buoy and radar measurements are close to the canonical saturation range tail observed with buoys (Chapter 2).

Chapter 4 (Davis et al., 2025) builds on Chapters 2 and 3 by exploring the spatial distribution of mean square slope in Hurricane Idalia (2023). Observations from a dense array of drifting buoys show mss has a secondary dependence (variation at a given wind speed) on the alignment of the wind and waves, or wind-wave alignment. Wind-wave alignment is predictive of mss deviations as large as 15% to 20% relative to a mean, primary dependence on wind speed. In a storm-following reference frame, wind and waves are aligned (small wind-wave alignment) to the right and rear of the storm and are crossing (moderate wind-wave alignment) in all other regions of the storm. The secondary dependence of mss on wind-wave alignment suggests a similar spatial distribution of mss, and thus surface roughness, within a storm. This dependence is consistent with prior work demonstrating an increase in drag coefficient in aligned wind and waves using observations (Zhou et al., 2022) and modeling (Manzella et al., 2024).

Chapter 5 explores the use of Distributed Acoustic Sensing to measure waves from a submarine fiber-optic cable offshore of Oliktok Point, Alaska. Two new machine learning models that estimate waves from along-cable strain were benchmarked against an empirical transfer function method previously used to estimate waves. The best-performing model uses machine learning to predict seafloor pressure spectra from frequency-wavenumber strain rate spectra. This model outperforms the empirical transfer function and a simpler neural network (both of which operate only on scalar, frequency spectra) in spectral and bulk wave parameter prediction across all considered regression metrics. Machine learning is effective even when the pressure-strain relationship varies temporally and spatially along a cable. Subsequent applications for machine learning-calibrated DAS in the Arctic include the study of wave-ice interactions and seasonal variation in wave action at the coast. This chapter will be submitted for journal publication.

6.2 Future Directions

Mean square slope has been, and should continue to be, explored in connection to wind stress and other important air-sea interaction processes. The arguments relating mean square slope to air-sea drag presented in Chapters 2–4 are only qualitative. A clear direction for future work is the pursuit of a quantitative relationship between mean square slope and wind stress, particularly at high wind speeds. There is mounting evidence that traditional parameterizations based on Monin–Obukhov similarity theory, which neglect surface waves, currents, and sea spray, are not applicable in hurricanes (e.g., Smith and Montgomery, 2014; Richter et al., 2016, 2021). As such, a connection between mean square slope and wind stress may instead take the form of a parameterization based on computational fluid dynamics modeling (e.g., large eddy simulation), controlled experimentation, or even data-driven methods. We should continue to pursue observational methods capable of measuring fluxes and sea spray coincident with waves inside hurricanes.

In Chapter 4, mean square slope is found to decrease with increasing wind-wave alignment. While this trend is qualitatively consistent with the dependence of drag coefficient on wind-wave alignment by some authors, including the indirect observations of Zhou et al. (2022) and monochromatic wave simulations of Manzella et al. (2024), it is opposite the trend observed in other studies. For instance, Holthuijsen et al. (2012) find a rapid increase in drag coefficient in cross-swell conditions, relative to aligned wind and swell conditions, using drag coefficients inferred from dropsonde wind profiles and the assumption of constant-stress region within the boundary layer (a basis of Monin–Obukhov similarity theory). Sauvage et al. (2024) find a 20% increase in drag coefficient in misaligned wind and waves generated by passing cold fronts using direct covariance momentum flux and wave observations. Disagreement in the sign of the dependence of drag coefficient and related proxies (e.g., mean square slope) on wind-wave alignment motivate further investigation across diverse conditions. In hurricanes, rapidly-evolving wind and wave directions may require a more nuanced definition of wind-wave alignment, including consideration for the direction of individually-partitioned wave components (as opposed to the bulk wave direction used in Chapter 4). Additional hurricane wave datasets collected during the NOPP Hurricane Coastal Impacts project (Section 1.3.1) and future field campaigns will be useful for exploring variations in mean square slope and wind-wave alignment with storm size, strength, and translation speed.

* * *

Chapter 5 identifies an effective machine learning-based model for predicting pressure spectra from submarine fiber-optic cable strain, yet this effort only scratches the surface of the possibilities for combining these two powerful technologies to measure waves. Sequential machine learning models, namely recurrent neural networks, should be explored for transforming strain to seafloor pressure in the time domain (i.e., phase-resolved wave predictions).

Future developments related to the f-k CNN model should focus on the validation of along-cable predictions. The incorporation of physics-informed constraints (e.g., in the loss function) may help to reduce uncertainty when these models are applied to unseen data outside the wave and ice conditions in the training dataset. Rigorous evaluation of performance in partially ice-covered periods, which are sharply heterogenous relative to the homogenous, open-water conditions used to develop the f-k CNN model, is needed. Validation during ice cover could use pressure mooring data from the early-summer period of the 2023 Oliktok mooring-DAS dataset (highly-attenuated, low-energy waves) or future mooring deployments during fall freeze-up (partially-attenuated, but moderate-energy waves). Additional comparisons with satellite observations, such as ICESat-2 or SWOT, provide opportunity for synoptic, full-cable comparisons. The 2-km of channels used to estimate the model's input f-k spectra are likely to smear-out gradients across ice, thus fine-tuning of this spatial extent is needed to determine the trade-off between accuracy and resolution. The success of a model based on f-k spectra may suggest wave direction is important for estimating pressure spectra from strain rate spectra. A hybrid approach, whereby wave direction is first determined from f-k spectra and then used as input to the spectral neural network model, should be explored for estimating pressure spectra at individual channels. Explainable AI techniques can also be used to determine the relative importance of input features, such that future deployments can focus on obtaining high quality measurements of the most important features.

A particularly exciting future application, which unifies the two themes explored in this dissertation, is the use of distributed acoustic sensing to monitor waves and water levels during hurricanes. There is one existing and three planned (for 2026–2028) telecommunication cables that transect the Gulf of Mexico, including cables which run offshore of Louisiana, the Big Bend of Florida, and Southwest Florida—all of which have historically high hurricane activity. These cables span a broad, shallow continental shelf, making them suitable for wave measurement from the seafloor (e.g., the 20-m depth contour often lies as far as 50–70 m offshore in these regions).

A hypothetical field campaign would include the lease of one or more of these cables during hurricane season (June to November) for continuous DAS measurement. Three or more seafloor moorings deployed over the cable during the same period would provide ground truth wave and water level measurements (similar to the Oliktok Point mooring-DAS dataset). Existing NDBC wave buoys, several of which are mooring nearby to the cables, and SWOT overpasses would provide additional training data and contextual meteorological measurements. An ideal dataset would include multiple periods with a wide range of wave conditions for model training, validation, and testing. While direct landfall near the cable would provide the largest dynamic range, any intense tropical cyclone that passes through the Gulf of Mexico should generate waves measurable by the cable due to the relatively small basin size. Strain-to-pressure models could be extended to lower frequencies to capture infragravity waves, which contribute to coastal flooding (e.g., Stockdon et al., 2007; Olabarrieta et al., 2023), but are not typically measurable by moored surface buoys. Machine learning models specific to the cable would be developed during an initial, intense observing period, and would then be used for subsequent wave measurement during future seasons (NDBC buoys could be used as a reference for when recalibration or additional training is needed).

Another novel application of DAS in hurricanes is the measurement of total water level using a cable extending onto land. A cross-shore fiber-optic cable could be laid across the beach near a hurricane's forecasted landfall location several days prior its arrival. Colocated cameras and gauges (such as custom-deployed or existing systems operated by the USGS) would then be used to derive methods for determining the wetted length of the cable, and thus local water levels, during a storm's passing. The estimation of shoreline position from DAS has been previously explored by Glover et al. (2024b) using a cable installed in Duck, NC. Similar proof-of-concept measurements could be made during winter storms on either Pacific or Atlantic coasts, where a cable could be installed and interrogated for several months without the need for time-sensitive deployment. This new, high-fidelity approach would add to the existing suite of water level measurement methods used to quantify and understand coastal impacts.

BIBLIOGRAPHY

Agarap, A. F. Deep Learning using Rectified Linear Units (ReLU), February 2019.

Akiba, T., Sano, S., Yanase, T., Ohta, T., and Koyama, M. Optuna: A next-generation hyperparameter optimization framework. In *The 25th ACM SIGKDD International Conference on Knowledge Discovery & Data Mining*, pages 2623–2631, 2019.

Amador, A., Merrifield, S. T., and Terrill, E. J. Assessment of Atmospheric and Oceanographic Measurements from an Autonomous Surface Vehicle. *Journal of Atmospheric and Oceanic Technology*, 40(3):305–326, 2023. ISSN 0739-0572, 1520-0426. doi: 10.1175/JTECH-D-22-0060.1.

Anctil, F. and Donelan, M. A. Air–Water Momentum Flux Observations over Shoaling waves. *Journal of Physical Oceanography*, 26(7):1344 – 1353, 1996. doi: 10.1175/1520-0485(1996)026<1344:AMFOOS>2.0.CO;2.

Arakawa, H. On the Pyramidal, Mountainous, and Confused Sea in the Right or Dangerous Semi-circle of Typhoon. *Meteorology and Geophysics Papers*, 1954.

Baker, M. G. and Abbott, R. E. Rapid Refreezing of a Marginal Ice Zone Across a Seafloor Distributed Acoustic Sensor. *Geophysical Research Letters*, 49(24), December 2022. ISSN 0094-8276, 1944-8007. doi: 10.1029/2022GL099880.

Banner, M. L. Equilibrium spectra of wind waves. *Journal of Physical Oceanography*, 20:966–984, 1990.

Banner, M. L., Gemmrich, J. R., and Farmer, D. M. Multiscale Measurements of Ocean Wave Breaking Probability. *Journal of Physical Oceanography*, 32(12):3364–3375, 2002. ISSN 0022-3670, 1520-0485. doi: 10.1175/1520-0485(2002)032<3364:MMOOWB>2.0.CO;2.

Barr, B. W., Chen, S. S., and Fairall, C. W. Sea-State-Dependent Sea Spray and Air–Sea Heat Fluxes in Tropical Cyclones: A New Parameterization for Fully Coupled Atmosphere–Wave–Ocean Models. *Journal of the Atmospheric Sciences*, 80(4):933–960, April 2023. ISSN 0022-4928, 1520-0469. doi: 10.1175/JAS-D-22-0126.1.

Barrick, D. Relationship between slope probability density function and the physical optics integral in rough surface scattering. *Proceedings of the IEEE*, 56(10):1728–1729, 1968. ISSN 0018-9219. doi: 10.1109/PROC.1968.6718.

Barstow, S. F., Bidlot, J.-R., Caires, S., Donelan, M. A., Drennan, W. M., Dupuis, H., Graber, H. C., Green, J., Gronlie, O., and Guérin, C. *Measuring and analysing the directional spectra of ocean waves*. COST Office, 2005.

Bishop, C. T. and Donelan, M. A. Measuring waves with pressure transducers. *Coastal Engineering*, 11(4):309–328, November 1987. ISSN 03783839. doi: 10.1016/0378-3839(87)90031-7.

Black, P. G., D'Asaro, E. A., Drennan, W. M., French, J. R., Niiler, P. P., Sanford, T. B., Terrill, E. J., Walsh, E. J., and Zhang, J. A. Air–Sea Exchange in Hurricanes: Synthesis of Observations from the Coupled Boundary Layer Air–Sea Transfer Experiment. *Bulletin of the American Meteorological Society*, 88(3):357–374, March 2007. ISSN 0003-0007, 1520-0477. doi: 10.1175/BAMS-88-3-357.

Boisot, O., Pioch, S., Fatras, C., Caulliez, G., Bringer, A., Borderies, P., Lalaurie, J., and Guérin, C. Ka-band backscattering from water surface at small incidence: A wind-wave tank study. *Journal of Geophysical Research: Oceans*, 120(5):3261–3285, May 2015. ISSN 2169-9275, 2169-9291. doi: 10.1002/2014JC010338.

Bruciaferri, D., Tonani, M., Lewis, H. W., Siddorn, J. R., Saulter, A., Castillo, J. M., Valiente, N. G., Conley, D., Sykes, P., Ascione, I., and McConnell, N. The impact of ocean-wave coupling on the upper ocean circulation during storm events. *Journal of Geophysical Research: Oceans*, 126 (6), 2021. doi: 10.1029/2021JC017343.

Bréon, F. M. and Henriot, N. Spaceborne observations of ocean glint reflectance and modeling of wave slope distributions. *Journal of Geophysical Research*, 111(C6):C06005, 2006. ISSN 0148-0227. doi: 10.1029/2005JC003343.

Buckley, M. P. and Veron, F. Structure of the Airflow above Surface Waves. *Journal of Physical Oceanography*, 46(5):1377–1397, May 2016. ISSN 0022-3670, 1520-0485. doi: 10.1175/JPO-D-15-0135.1.

Cangialosi, J. P. and Alaka, L. Hurricane Idalia (AL102023). National Hurricane Center Tropical Cyclone Report, National Hurricane Center, February 2024.

Carreno-Luengo, H., Crespo, J. A., Akbar, R., Bringer, A., Warnock, A., Morris, M., and Ruf, C. The CYGNSS Mission: On-Going Science Team Investigations. *Remote Sensing*, 13(9):1814, May 2021. ISSN 2072-4292. doi: 10.3390/rs13091814.

Charnock, H. Wind stress on a water surface. *Quarterly Journal of the Royal Meteorological Society*, 81(350):639–640, October 1955. ISSN 00359009, 1477870X. doi: 10.1002/qj.49708135027.

Chen, D. D., Ruf, C. S., and Gleason, S. T. Response time of mean square slope to wind forcing: An empirical investigation. *Journal of Geophysical Research: Oceans*, 121(4):2809–2823, April 2016. ISSN 2169-9275, 2169-9291. doi: 10.1002/2016JC011661.

Chen, P., Zheng, G., Hauser, D., and Xu, F. Quasi-Gaussian probability density function of sea wave slopes from near nadir Ku-band radar observations. *Remote Sensing of Environment*, 217: 86–100, November 2018. ISSN 00344257. doi: 10.1016/j.rse.2018.07.027.

Chen, S., Qiao, F., Zhang, J. A., Xue, Y., Ma, H., and Chen, S. Observed Drag Coefficient Asymmetry in a Tropical Cyclone. *Journal of Geophysical Research: Oceans*, 127(9):e2021JC018360, 2022. ISSN 2169-9275, 2169-9291. doi: 10.1029/2021JC018360.

Chen, X., Ginis, I., and Hara, T. Impact of Shoaling Ocean Surface Waves on Wind Stress and Drag Coefficient in Coastal Waters: 2. Tropical Cyclones. *Journal of Geophysical Research: Oceans*, 2020a. ISSN 2169-9275, 2169-9291. doi: 10.1029/2020JC016223.

Chen, X., Hara, T., and Ginis, I. Impact of Shoaling Ocean Surface Waves on Wind Stress and Drag Coefficient in Coastal Waters: 1. Uniform Wind. *Journal of Geophysical Research: Oceans*, 2020b. doi: 10.1029/2020JC016222.

Christie, D. C. Efficient estimation of directional wave buoy spectra using a reformulated Maximum Shannon Entropy Method: Analysis and comparisons for coastal wave datasets. *Applied Ocean Research*, 2024. doi: 10.1016/j.apor.2023.103830.

Clarizia, M. P. and Ruf, C. S. Wind Speed Retrieval Algorithm for the Cyclone Global Navigation Satellite System (CYGNSS) Mission. *IEEE Transactions on Geoscience and Remote Sensing*, 54 (8):4419–4432, August 2016. ISSN 0196-2892, 1558-0644. doi: 10.1109/TGRS.2016.2541343.

Cline, I. M. Relation of changes in storm tides on the coast of the gulf of mexico to the center and movement of hurricanes. *Monthly Weather Review*, 48:127–146, 1920.

Collins, C. O., Blomquist, B., Persson, O., Lund, B., Rogers, W. E., Thomson, J., Wang, D., Smith, M., Doble, M., Wadhams, P., Kohout, A., Fairall, C., and Graber, H. C. Doppler Correction of Wave Frequency Spectra Measured by Underway Vessels. *Journal of Atmospheric and Oceanic Technology*, 34(2):429–436, February 2017. ISSN 0739-0572, 1520-0426. doi: 10.1175/JTECH-D-16-0138.1.

Collins, C. O., Potter, H., Lund, B., Tamura, H., and Graber, H. C. Directional wave spectra observed during intense tropical cyclones. *Journal of Geophysical Research: Oceans*, 2018a. ISSN 2169-9291. doi: 10.1002/2017JC012943.

Collins, C. O., Potter, H., Lund, B., Tamura, H., and Graber, H. C. Directional Wave Spectra Observed During Intense Tropical Cyclones. *Journal of Geophysical Research: Oceans*, 123(2): 773–793, 2018b. ISSN 2169-9275, 2169-9291. doi: 10.1002/2017JC012943.

Colosi, L., Pizzo, N., Grare, L., Statom, N., and Lenain, L. Observations of Surface Gravity Wave Spectra from Moving Platforms. *Journal of Atmospheric and Oceanic Technology*, 40(10):1153–1169, October 2023. ISSN 0739-0572, 1520-0426. doi: 10.1175/JTECH-D-23-0022.1.

Cox, C. and Munk, W. Measurement of the Roughness of the Sea Surface from Photographs of the Sun's Glitter. *Journal of the Optical Society of America*, 44(11):838, November 1954. ISSN 0030-3941. doi: 10.1364/JOSA.44.000838.

Curcic, M. and Haus, B. K. Revised Estimates of Ocean Surface Drag in Strong Winds. *Geophysical Research Letters*, 47(10):e2020GL087647, May 2020. ISSN 0094-8276, 1944-8007. doi: 10.1029/2020GL087647.

Davis, C., Wang, W., Chen, S. S., Chen, Y., Corbosiero, K., DeMaria, M., Dudhia, J., Holland, G., Klemp, J., Michalakes, J., Reeves, H., Rotunno, R., Snyder, C., and Xiao, Q. Prediction of Landfalling Hurricanes with the Advanced Hurricane WRF Model. *Monthly Weather Review*, 136(6):1990–2005, June 2008. ISSN 1520-0493, 0027-0644. doi: 10.1175/2007MWR2085.1.

Davis, J., Thomson, J., Houghton, I., Doyle, J. D., Komaromi, W., Moskaitis, J., Fairall, C. W., and Thompson, E. J. Data to accompany the article "saturation of ocean surface wave slopes observed during hurricanes", September 2023a.

Davis, J. R. Code for: Ocean surface wave slopes and wind-wave alignment observed in Hurricane Idalia, 2024.

Davis, J. R., Thomson, J., Houghton, I. A., Doyle, J. D., Komaromi, W. A., Fairall, C. W., Thompson, E. J., and Moskaitis, J. R. Saturation of Ocean Surface Wave Slopes Observed During Hurricanes. *Geophysical Research Letters*, 50(16), August 2023b. doi: 10.1029/2023GL104139.

Davis, J. R., Thomson, J., Butterworth, B. J., Houghton, I. A., Fairall, C., Thompson, E. J., and De Boer, G. Multiscale measurements of hurricane waves using buoys and airborne radar. In *2024 IEEE/OES Thirteenth Current, Waves and Turbulence Measurement (CWTM)*, Wanchese, NC, USA, March 2024a. IEEE. doi: 10.1109/CWTM61020.2024.10526332.

Davis, J. R., Thomson, J., Houghton, I. A., Fairall, C. W., Butterworth, B. J., Thompson, E. J., De Boer, G., Doyle, J. D., and Moskaitis, J. R. Data for: Ocean surface wave slopes and wind-wave alignment observed in Hurricane Idalia, 2024b.

Davis, J. R., Thomson, J., Houghton, I. A., Fairall, C. W., Butterworth, B. J., Thompson, E. J., De Boer, G., Doyle, J. D., and Moskaitis, J. R. Ocean Surface Wave Slopes and Wind-Wave Alignment Observed in Hurricane Idalia. *Journal of Geophysical Research: Oceans*, 130(2), February 2025. doi: 10.1029/2024JC021814.

Dietrich, J. C., Westerink, J. J., Kennedy, A. B., Smith, J. M., Jensen, R. E., Zijlema, M., Holthuijsen, L. H., Dawson, C., Luettich, R. A., Powell, M. D., Cardone, V. J., Cox, A. T., Stone, G. W., Pourtaheri, H., Hope, M. E., Tanaka, S., Westerink, L. G., Westerink, H. J., and Cobell, Z. Hurricane Gustav (2008) Waves and Storm Surge: Hindcast, Synoptic Analysis, and Validation in Southern Louisiana. *Monthly Weather Review*, 139(8):2488–2522, August 2011. ISSN 0027-0644, 1520-0493. doi: 10.1175/2011MWR3611.1.

Donelan, M. A. On the limiting aerodynamic roughness of the ocean in very strong winds. *Geophysical Research Letters*, 31(18), 2004. doi: 10.1029/2004GL019460.

Donelan, M. A., Curcic, M., Chen, S. S., and Magnusson, A. K. Modeling waves and wind stress. *Journal of Geophysical Research: Oceans*, 117, November 2012. ISSN 0148-0227. doi: 10.1029/2011JC007787.

Donelan, M. A. On the Decrease of the Oceanic Drag Coefficient in High Winds. *Journal of Geophysical Research: Oceans*, 2018. ISSN 2169-9291. doi: 10.1002/2017JC013394.

Dorsay, C., Egan, G., Houghton, I., Hegermiller, C., and Smit, P. B. Proxy Observations of Surface Wind from a Globally Distributed Network of Wave Buoys. *Journal of Atmospheric and Oceanic Technology*, 40(12):1591–1603, December 2023a. ISSN 0739-0572, 1520-0426. doi: 10.1175/JTECH-D-23-0044.1.

Dorsay, C., Houghton, I., Davis, J., Thomson, J., Smit, P., and Stackpole, E. Aerial Deployment of Spotter Wave Buoys During Hurricane Ian. In *OCEANS 2023 - MTS/IEEE U.S. Gulf Coast*, pages 1–5, Biloxi, MS, USA, September 2023b. IEEE. ISBN 9798218142186. doi: 10.23919/OCEANS52994.2023.10337056.

Doyle, J., Jin, Y., Hodur, R. M., Chen, S., Jin, H., Moskaitis, J., Reinecke, A., Black, P., Cummings, J., Hendricks, E., Holt, T., Liou, C.-S., Peng, M., Reynolds, C., Sashegyi, K., Schmidt, J., and Wang, S. Real-time tropical cyclone prediction using COAMPS-TC. pages 15–28. October 2012. doi: 10.1142/9789814405683_0002.

Doyle, J., Hodur, R., Chen, S., Jin, Y., Msokaitis, J., Wang, S., Hendricks, E., Jin, J., and Smith, T. Tropical Cyclone Prediction Using COAMPS-TC. *Oceanography*, 27(3):104–115, September 2014. ISSN 10428275. doi: 10.5670/oceanog.2014.72.

Doyle, J. D. Coupled Atmosphere–Ocean Wave Simulations under High Wind Conditions. *Monthly Weather Review*, 130(12):3087–3099, 2002. ISSN 0027-0644, 1520-0493. doi: 10.1175/1520-0493(2002)130<3087:CAOWSU>2.0.CO;2.

Drazen, D. A., Melville, W. K., and Lenain, L. Inertial scaling of dissipation in unsteady breaking waves. *Journal of Fluid Mechanics*, 611:307–332, September 2008. ISSN 0022-1120, 1469-7645. doi: 10.1017/S0022112008002826.

Drennan, W. M., Graber, H. C., Hauser, D., and Quentin, C. On the wave age dependence of wind stress over pure wind seas. *Journal of Geophysical Research*, 108:8062, 2003. doi: 10.1029/2000JC000715.

Duncan, J. H. An experimental investigation of breaking waves produced by a towed hydrofoil. *Proceedings of the Royal Society of London. A. Mathematical and Physical Sciences*, 377(1770): 331–348, July 1981. ISSN 0080-4630. doi: 10.1098/rspa.1981.0127.

Duncan, S., Cox, D., Barbosa, A. R., Lomónaco, P., Park, H., Alam, M. S., and Yu, C. Physical modeling of progressive damage and failure of wood-frame coastal residential structures due to surge and wave forces. *Coastal Engineering*, 169:103959, October 2021. ISSN 03783839. doi: 10.1016/j.coastaleng.2021.103959.

Edson, J. B., Jampana, V., Weller, R. A., Bigorre, S. P., Plueddemann, A. J., Fairall, C. W., Miller, S. D., Mahrt, L., Vickers, D., and Hersbach, H. On the Exchange of Momentum over the Open

Ocean. *Journal of Physical Oceanography*, 43(8):1589–1610, 2013. ISSN 0022-3670, 1520-0485. doi: 10.1175/JPO-D-12-0173.1.

Elfouhaily, T., Chapron, B., Katsaros, K., and Vandemark, D. A unified directional spectrum for long and short wind-driven waves. *Journal of Geophysical Research: Oceans*, 102(C7):15781–15796, July 1997. ISSN 01480227. doi: 10.1029/97JC00467.

Emanuel, K. A Similarity Hypothesis for Air–Sea Exchange at Extreme Wind Speeds. *Journal of the Atmospheric Sciences*, 60(11):1420–1428, June 2003. ISSN 0022-4928, 1520-0469. doi: 10.1175/1520-0469(2003)060<1420:ASHFAE>2.0.CO;2.

Esquivel-Trava, B., Ocampo-Torres, F. J., and Osuna, P. Spatial structure of directional wave spectra in hurricanes. *Ocean Dynamics*, 65(1):65–76, 2015. ISSN 1616-7341, 1616-7228. doi: 10.1007/s10236-014-0791-9.

Forristall, G. Z. Measurements of a saturated range in ocean wave spectra. *Journal of Geophysical Research*, 86(C9):8075, 1981. ISSN 0148-0227. doi: 10.1029/JC086iC09p08075.

Gahtan, J., Knapp, K. R., Schreck, C. J. I., Diamond, H. J., Kossin, J. P., and Kruk, M. C. International Best Track Archive for Climate Stewardship (IBTrACS) Project v4.01 (last 3 years), 2024.

GEBCO Bathymetric Compilation Group. The GEBCO_2023 Grid - a continuous terrain model of the global oceans and land., April 2023.

Gemmrich, J., Mudge, T., and Polonichko, V. On the energy input from wind to surface waves. *J. Phys. Oceanogr.*, 24:2413–2417, 1994.

Gibbs, A. E. and Richmond, B. M. National assessment of shoreline change—Summary statistics for updated vector shorelines and associated shoreline change data for the north coast of Alaska, U.S.-Canadian Border to Icy Cape. Report 2017-1107, Reston, VA, 2017.

Gleason, S., Zavorotny, V. U., Akos, D. M., Hrbek, S., PopStefanija, I., Walsh, E. J., Masters, D., and Grant, M. S. Study of Surface Wind and Mean Square Slope Correlation in Hurricane Ike With Multiple Sensors. *IEEE Journal of Selected Topics in Applied Earth Observations and Remote Sensing*, 11(6):1975–1988, June 2018. ISSN 1939-1404, 2151-1535. doi: 10.1109/JSTARS.2018.2827045.

Glover, H., Smith, M., Thomson, J., Williams, E., Wengrove, M., Ifju, M., and Lipovsky, B. Comparisons of Seafloor Distributed Fiber-optic Sensing Datasets and Empirical Calibrations for Inferring Ocean Surface Gravity Waves, November 2024a.

Glover, H., Wengrove, M., and Holman, R. Measuring hydrodynamics and exploring nearshore processes using distributed sensing of fiber-optic cable strain. *Coastal Engineering*, 190:104487, June 2024b. ISSN 03783839. doi: 10.1016/j.coastaleng.2024.104487.

Gonzalez, F. I., Thompson, T. W., Brown, W. E., and Weissman, D. E. SEASAT wind and wave observations of northeast Pacific hurricane Iva, August 13, 1978. *Journal of Geophysical Research: Oceans*, 87(C5):3431–3438, 1982. ISSN 0148-0227. doi: 10.1029/JC087iC05p03431.

Guérin, C.-A., Capelle, V., and Hartmann, J.-M. Revisiting the Cox and Munk wave-slope statistics using IASI observations of the sea surface. *Remote Sensing of the Environment*, October 2022.

Hauser, D., Caudal, G., Guimbard, S., and Mouche, A. A. A study of the slope probability density function of the ocean waves from radar observations. *Journal of Geophysical Research: Oceans*, 113(C2):2007JC004264, February 2008. ISSN 0148-0227. doi: 10.1029/2007JC004264.

Hauser, D., Tison, C., Amiot, T., Delaye, L., Corcoral, N., and Castillan, P. SWIM: The First Spaceborne Wave Scatterometer. *IEEE Transactions on Geoscience and Remote Sensing*, 55(5): 3000–3014, May 2017. ISSN 0196-2892, 1558-0644. doi: 10.1109/TGRS.2017.2658672.

Hegermiller, C. A., Warner, J. C., Olabarrieta, M., and Sherwood, C. R. Wave–current interaction between hurricane matthew wave fields and the gulf stream. *Journal of Physical Oceanography*, 49(11):2883–2900, 2019. doi: 10.1175/JPO-D-19-0124.1.

Hell, M. C., Ayet, A., and Chapron, B. Swell generation under extra-tropical storms. *Journal of Geophysical Research: Oceans*, 2021. doi: 10.1029/2021JC017637.

Hell, M. C. and Horvat, C. A method for constructing directional surface wave spectra from ICESat-2 altimetry. *The Cryosphere*, 18(1):341–361, 2024. ISSN 1994-0424. doi: 10.5194/tc-18-341-2024.

Herbers, T. H. C., Jessen, P. F., Janssen, T. T., Colbert, D. B., and MacMahan, J. H. Observing Ocean Surface Waves with GPS-Tracked Buoys. *Journal of Atmospheric and Oceanic Technology*, 29(7):944–959, 2012. ISSN 0739-0572, 1520-0426. doi: 10.1175/JTECH-D-11-00128.1.

Holthuijsen, L. H. *Waves in Oceanic and Coastal Waters*. Cambridge University Press, Cambridge, 2007. ISBN 978-0-521-12995-4. doi: 10.1017/CBO9780511618536.

Holthuijsen, L. H., Powell, M. D., and Pietrzak, J. D. Wind and waves in extreme hurricanes. *Journal of Geophysical Research: Oceans*, 117(C9), September 2012. ISSN 01480227. doi: 10.1029/2012JC007983.

Houghton, I., Smit, P., Clark, D., Dunning, C., Fisher, A., Nidzieko, N., Chamberlain, P., and Janssen, T. Performance statistics of a real-time Pacific Ocean weather sensor network. *Journal of Atmospheric and Oceanic Technology*, April 2021. ISSN 0739-0572, 1520-0426. doi: 10.1175/JTECH-D-20-0187.1.

Houghton, I. et al. Predicting Coastal Impacts of Hurricanes. *Bulletin of the American Meteorological Society*, 2025. (In review).

Hošeková, L., Malila, M. P., Rogers, W. E., Roach, L. A., Eidam, E., Rainville, L., Kumar, N., and Thomson, J. Attenuation of Ocean Surface Waves in Pancake and Frazil Sea Ice Along the Coast of the Chukchi Sea. *Journal of Geophysical Research: Oceans*, 125(12):e2020JC016746, 2020. ISSN 2169-9275, 2169-9291. doi: 10.1029/2020JC016746.

Hošeková, L., Eidam, E., Panteleev, G., Rainville, L., Rogers, W. E., and Thomson, J. Landfast Ice and Coastal Wave Exposure in Northern Alaska. *Geophysical Research Letters*, 48(22), November 2021. ISSN 0094-8276, 1944-8007. doi: 10.1029/2021GL095103.

Hsu, J.-Y. Observing surface wave directional spectra under typhoon megi (2010) using subsurface em-apex floats. *Journal of Atmospheric and Oceanic Technology*, 38(11):1949–1966, 2021a. doi: 10.1175/JTECH-D-20-0210.1.

Hsu, J.-Y. Observing Surface Wave Directional Spectra under Typhoon Megi (2010) Using Subsurface EM-APEX Floats. *Journal of Atmospheric and Oceanic Technology*, 38(11):1949–1966, November 2021b. ISSN 0739-0572, 1520-0426. doi: 10.1175/JTECH-D-20-0210.1.

Hsu, J.-Y., Lien, R.-C., D'Asaro, E. A., and Sanford, T. B. Scaling of drag coefficients under five tropical cyclones. *Geophysical Research Letters*, 46(6):3349–3358, 2019. doi: 10.1029/2018GL081574.

Hsu, S. A., Yijun, H., and Shen, H. Buoy measurements of wind–wave relations during hurricane matthew in 2016. *Journal of Physical Oceanography*, 47(10):2603–2609, 2017. doi: 10.1175/JPO-D-16-0280.1.

Hu, K. and Chen, Q. Directional spectra of hurricane-generated waves in the Gulf of Mexico. *Geophysical Research Letters*, 38(19):n/a–n/a, October 2011. ISSN 00948276. doi: 10.1029/2011GL049145.

Husain, N. T., Hara, T., and Sullivan, P. P. Wind Turbulence over Misaligned Surface Waves and Air–Sea Momentum Flux. Part II: Waves in Oblique Wind. *Journal of Physical Oceanography*, 52(1):141–159, 2022. ISSN 0022-3670, 1520-0485. doi: 10.1175/JPO-D-21-0044.1.

Hwang, P. A. Wave number spectrum and mean square slope of intermediate-scale ocean surface waves. *Journal of Geophysical Research: Oceans*, 110, 2005. doi: 10.1029/2005JC003002.

Hwang, P. A. Fetch- and duration-limited nature of surface wave growth inside tropical cyclones: With applications to air–sea exchange and remote sensing. *Journal of Physical Oceanography*, 46:41–56, 2016. doi: 10.1175/JPO-D-15-0173.1.

Hwang, P. A. High-wind drag coefficient and whitecap coverage derived from microwave radiometer observations in tropical cyclones. *Journal of Physical Oceanography*, 48(10):2221–2232, 2018. doi: 10.1175/JPO-D-18-0107.1.

Hwang, P. A. and Fan, Y. Effective fetch and duration of tropical cyclone wind fields estimated from simultaneous wind and wave measurements: Surface wave and air–sea exchange computation. *Journal of Physical Oceanography*, 47(2):447–470, 2017. doi: 10.1175/JPO-D-16-0180.1.

Hwang, P. A. and Fan, Y. Low-Frequency Mean Square Slopes and Dominant Wave Spectral Properties: Toward Tropical Cyclone Remote Sensing. *IEEE Transactions on Geoscience and Remote Sensing*, (12), 2018. ISSN 0196-2892, 1558-0644. doi: 10.1109/TGRS.2018.2850969.

Hwang, P. A. and Shemdin, O. H. The Dependence of Sea Surface Slope on Atmospheric Stability and Swell Conditions. *Journal of Geophysical Research*, 1988.

Hwang, P. A. and Walsh, E. J. Propagation directions of ocean surface waves inside tropical cyclones. *Journal of Physical Oceanography*, 48(7):1495–1511, 2018. doi: 10.1175/JPO-D-18-0015.1.

Hwang, P. A., Fan, Y., Ocampo-Torres, F. J., and García-Nava, H. Ocean Surface Wave Spectra inside Tropical Cyclones. *Journal of Physical Oceanography*, 47(10):2393–2417, 2017. doi: 10.1175/JPO-D-17-0066.1.

Hwang, P. A., Ainsworth, T. L., and Ouellette, J. D. Microwave Specular Measurements and Ocean Surface Wave Properties. *Sensors*, 21(4):1486, February 2021. ISSN 1424-8220. doi: 10.3390/s21041486.

Iyer, S., Thomson, J., Thompson, E., and Drushka, K. Variations in Wave Slope and Momentum Flux From Wave-Current Interactions in the Tropical Trade Winds. *Journal of Geophysical Research: Oceans*, 127(3), March 2022. ISSN 2169-9275, 2169-9291. doi: 10.1029/2021JC018003.

Jackson, F. C., Walton, W. T., Hines, D. E., Walter, B. A., and Peng, C. Y. Sea surface mean square slope from K_u -band backscatter data. *Journal of Geophysical Research: Oceans*, 97:11411–11427, July 1992. ISSN 0148-0227. doi: 10.1029/92JC00766.

Janssen, P. A. E. M. Wave-Induced Stress and the Drag of Air Flow over Sea Waves. *Journal of Physical Oceanography*, 19(6):745 – 754, 1989. doi: 10.1175/1520-0485(1989)019<0745:WISATD>2.0.CO;2.

Janssen, P. A. E. M. and Bidlot, J.-R. Wind–wave interaction for strong winds. *Journal of Physical Oceanography*, 53(3):779 – 804, 2023. doi: 10.1175/JPO-D-21-0293.1.

Jensen, R. E., Swail, V., and Bouchard, R. H. Quantifying wave measurement differences in historical and present wave buoy systems. *Ocean Dynamics*, 71(6-7):731–755, July 2021. ISSN 1616-7341, 1616-7228. doi: 10.1007/s10236-021-01461-0.

Jiménez, P. A. and Dudhia, J. On the Need to Modify the Sea Surface Roughness Formulation over Shallow Waters. *Journal of Applied Meteorology and Climatology*, 57(5), 2018. ISSN 1558-8424, 1558-8432. doi: 10.1175/JAMC-D-17-0137.1.

Kalinin, S. V., Kelley, K., Vasudevan, R. K., and Ziatdinov, M. Toward Decoding the Relationship between Domain Structure and Functionality in Ferroelectrics via Hidden Latent Variables. *ACS Applied Materials & Interfaces*, 13(1):1693–1703, January 2021. ISSN 1944-8244. doi: 10.1021/acsami.0c15085.

Katzberg, S. J., Dunion, J., and Ganoe, G. G. The use of reflected GPS signals to retrieve ocean surface wind speeds in tropical cyclones. *Radio Science*, 48(4):371–387, July 2013. ISSN 0048-6604, 1944-799X. doi: 10.1002/rds.20042.

Kennedy, A., Rogers, S., Sallenger, A., Gravois, U., Zachry, B., Dosa, M., and Zarama, F. Building Destruction from Waves and Surge on the Bolivar Peninsula during Hurricane Ike. *Journal of Waterway, Port, Coastal, and Ocean Engineering*, 137(3):132–141, 2011. ISSN 0733-950X, 1943-5460. doi: 10.1061/(ASCE)WW.1943-5460.0000061.

King, D. B. and Shemdin, O. H. Radar Observation of Hurricane Wave Directions. In *Coastal Engineering 1978*, pages 209–226, Hamburg, Germany, August 1978. American Society of Civil Engineers. ISBN 978-0-87262-190-9 978-0-7844-7960-5. doi: 10.1061/9780872621909.012.

Kita, Y. and Waseda, T. Ocean surface wave effects on development of explosive cyclone. *Earth and Space Science Open Archive*, page 35, 2022. doi: 10.1002/essoar.10510382.1.

Klotz, B. W. and Uhlhorn, E. W. Improved Stepped Frequency Microwave Radiometer Tropical Cyclone Surface Winds in Heavy Precipitation. *Journal of Atmospheric and Oceanic Technology*, 31(11):2392–2408, 2014. doi: 10.1175/JTECH-D-14-00028.1.

Knapp, K. R., Kruk, M. C., Levinson, D. H., Diamond, H. J., and Neumann, C. J. The International Best Track Archive for Climate Stewardship, (IBTrACS): Unifying tropical cyclone best track data. *Bulletin of the American Meteorological Society*, 91:363–376, 2010a. doi: 10.1175/2009BAMS2755.1.

Knapp, K. R., Diamond, H. J., Kossin, J. P., Kruk, M. C., and Schreck, C. J. International Best Track Archive for Climate Stewardship (IBTrACS) Project, version 04r00, 2018.

Knapp, K. R., Kruk, M. C., Levinson, D. H., Diamond, H. J., and Neumann, C. J. The International Best Track Archive for Climate Stewardship (IBTrACS): Unifying Tropical Cyclone Data. *Bulletin of the American Meteorological Society*, 91(3):363–376, March 2010b. ISSN 0003-0007, 1520-0477. doi: 10.1175/2009BAMS2755.1.

Kobune, K. and Hashimoto, N. Estimation of directional spectra from the maximum entropy principle. pages 80–85, Tokyo, 1986.

Kovesi, P. Good Colour Maps: How to Design Them, 2015.

Kudryavtsev, V. and Makin, V. Aerodynamic roughness of the sea surface at high winds. *Boundary-Layer Meteorology*, 125(2):289–303, September 2007. ISSN 0006-8314, 1573-1472. doi: 10.1007/s10546-007-9184-7.

Kudryavtsev, V., Golubkin, P., and Chapron, B. A simplified wave enhancement criterion for moving extreme events. *Journal of Geophysical Research: Oceans*, 2015. ISSN 2169-9291. doi: 10.1002/2015JC011284.

Kudryavtsev, V., Yurovskaya, M., and Chapron, B. Self-Similarity of Surface Wave Developments Under Tropical Cyclones. *Journal of Geophysical Research: Oceans*, 126(4):e2020JC016916, 2021. ISSN 2169-9275, 2169-9291. doi: 10.1029/2020JC016916.

Kuik, A. J., van Vledder, G. P., and Holthuijsen, L. H. A Method for the Routine Analysis of Pitch-and-Roll Buoy Wave Data. *Journal of Physical Oceanography*, 18(7):1020–1034, 1988. ISSN 0022-3670, 1520-0485. doi: 10.1175/1520-0485(1988)018<1020:AMFTRA>2.0.CO;2.

Ladjal, S., Newson, A., and Pham, C.-H. A PCA-like Autoencoder. *CoRR*, abs/1904.01277, 2019. doi: 10.48550/arXiv.1904.01277.

Lan, Y., Sun, D., Leng, H., Song, J., Cao, X., and Dong, R. A New Sea Surface Roughness Parameterization and Its Application in Tropical Cyclone Modeling. *Journal of Geophysical Research: Atmospheres*, 127(24), 2022. ISSN 2169-897X, 2169-8996. doi: 10.1029/2022JD037159.

Laxague, N. J. M., Zappa, C. J., LeBel, D. A., and Banner, M. L. Spectral Characteristics of Gravity-Capillary Waves, With Connections to Wave Growth and Microbreaking. *Journal of Geophysical Research: Oceans*, 123(7):4576–4592, July 2018. ISSN 2169-9275, 2169-9291. doi: 10.1029/2018JC013859.

Lenain, L. and Melville, W. K. Measurements of the Directional Spectrum across the Equilibrium Saturation Ranges of Wind-Generated Surface Waves. *Journal of Physical Oceanography*, 47 (8):2123–2138, August 2017. ISSN 0022-3670, 1520-0485. doi: 10.1175/JPO-D-17-0017.1.

Lenain, L. and Pizzo, N. The Contribution of High-Frequency Wind-Generated Surface Waves to the Stokes Drift. *Journal of Physical Oceanography*, 50(12):3455–3465, December 2020. ISSN 0022-3670, 1520-0485. doi: 10.1175/JPO-D-20-0116.1.

Lenain, L., Statom, N. M., and Melville, W. K. Airborne Measurements of Surface Wind and Slope Statistics over the Ocean. *Journal of Physical Oceanography*, 49(11):2799–2814, November 2019. ISSN 0022-3670, 1520-0485. doi: 10.1175/JPO-D-19-0098.1.

Li, X., Karaev, V., Panfilova, M., Liu, B., Wang, Z., Xu, Y., Liu, J., and He, Y. Measurements of total sea surface mean square slope field based on SWIM data. *IEEE Transactions on Geoscience and Remote Sensing*, 2022. ISSN 0196-2892, 1558-0644. doi: 10.1109/TGRS.2022.3174392.

Lin, J., Fang, S., He, R., Tang, Q., Qu, F., Wang, B., and Xu, W. Monitoring ocean currents during the passage of Typhoon Muifa using optical-fiber distributed acoustic sensing. *Nature Communications*, 15(1):1111, February 2024. ISSN 2041-1723. doi: 10.1038/s41467-024-45412-x.

Lindsey, N. J., Dawe, T. C., and Ajo-Franklin, J. B. Illuminating seafloor faults and ocean dynamics with dark fiber distributed acoustic sensing. *Science*, 366(6469):1103–1107, November 2019. ISSN 0036-8075, 1095-9203. doi: 10.1126/science.aay5881.

Liu, Y., Su, M.-Y., Yan, X.-H., and Liu, W. T. The Mean-Square Slope of Ocean Surface Waves and Its Effects on Radar Backscatter. *Journal of Atmospheric and Oceanic Technology*, 17(8): 1092–1105, August 2000. ISSN 0739-0572, 1520-0426. doi: 10.1175/1520-0426(2000)017<1092:TMSSOO>2.0.CO;2.

Longuet-Higgins, M. S. Eulerian and Lagrangian aspects of surface waves. *Journal of Fluid Mechanics*, 173:683–707, December 1986. ISSN 0022-1120, 1469-7645. doi: 10.1017/S0022112086001325.

Loshchilov, I. and Hutter, F. Decoupled Weight Decay Regularization, January 2019.

Mahoney, A. R., Eicken, H., Gaylord, A. G., and Gens, R. Landfast sea ice extent in the Chukchi and Beaufort Seas: The annual cycle and decadal variability. *Cold Regions Science and Technology*, 103:41–56, July 2014. ISSN 0165232X. doi: 10.1016/j.coldregions.2014.03.003.

Manos, J.-M., Gräff, D., Martin, E., Paitz, P., Walter, F., Fichtner, A., and Lipovsky, B. DAS to Discharge: Using Distributed Acoustic Sensing (DAS) to infer glacier runoff. preprint, Earth Sciences, February 2024.

Manzella, E., Hara, T., and Sullivan, P. P. Reduction of Drag Coefficient Due To Misaligned Wind-Waves. *Journal of Geophysical Research: Oceans*, 129(5):e2023JC020593, 2024. ISSN 2169-9275, 2169-9291. doi: 10.1029/2023JC020593.

Melville, W. K. Energy Dissipation by Breaking Waves. *Journal of Physical Oceanography*, 1994.

Meulé, S., Pelaez-Quiñones, J., Bouchette, F., Sladen, A., Ponte, A., Maier, A., Lior, I., and Coyle, P. Reconstruction of Nearshore Surface Gravity Wave Heights From Distributed Acoustic Sensing Data. *Earth and Space Science*, 11(11):e2024EA003589, November 2024. ISSN 2333-5084, 2333-5084. doi: 10.1029/2024EA003589.

Mudd, K. C., Ho, A., Amador, A., Lodise, J., Behrens, J., and Merrifield, S. T. Wind velocity estimates from wave observing platforms. *Coastal Engineering Journal*, 66(3):479–491, July 2024. ISSN 2166-4250, 1793-6292. doi: 10.1080/21664250.2024.2321660.

Ni, Y., Denolle, M. A., Shi, Q., Lipovsky, B. P., Pan, S., and Kutz, J. N. Wavefield Reconstruction of Distributed Acoustic Sensing: Lossy Compression, Wavefield Separation, and Edge Computing. *Journal of Geophysical Research: Machine Learning and Computation*, 1(3):e2024JH000247, September 2024. ISSN 2993-5210, 2993-5210. doi: 10.1029/2024JH000247.

NOAA National Data Buoy Center. Meteorological and oceanographic data collected from the National Data Buoy Center Coastal-Marine Automated Network (C-MAN) and moored (weather) buoys. Station 42036 (LLNR 855) - WEST TAMPA, 1971.

Olabarrieta, M., Warner, J. C., and Hegermiller, C. A. Development and Application of an Infragravity Wave (InWave) Driver to Simulate Nearshore Processes. *Journal of Advances in Modeling Earth Systems*, 15(6):e2022MS003205, 2023. ISSN 1942-2466, 1942-2466. doi: 10.1029/2022MS003205.

Patterson, M. M. Oceanographic Data from Hurricane Camille. In *Offshore Technology Conference*, Houston, Texas, 1974. doi: 10.4043/2109-MS.

Peña Castro, A. F., Schmandt, B., Baker, M. G., and Abbott, R. E. Tracking Local Sea Ice Extent in the Beaufort Sea Using Distributed Acoustic Sensing and Machine Learning. *The Seismic Record*, 3(3):200–209, July 2023. ISSN 2694-4006. doi: 10.1785/0320230019.

Phillips, O. M. Spectral and statistical properties of the equilibrium range in wind-generated gravity waves. *Journal of Fluid Mechanics*, 156:505, July 1985. ISSN 0022-1120, 1469-7645. doi: 10.1017/S0022112085002221.

Pincus, R., Fairall, C. W., Bailey, A., Chen, H., Chuang, P. Y., De Boer, G., Feingold, G., Henze, D., Kalen, Q. T., Kazil, J., Leandro, M., Lundry, A., Moran, K., Naeher, D. A., Noone, D., Patel, A. J., Pezoa, S., PopStefanija, I., Thompson, E. J., Warnecke, J., and Zuidema, P. Observations from the NOAA P-3 aircraft during ATOMIC. *Earth System Science Data*, (7):3281–3296, July 2021. doi: 10.5194/essd-13-3281-2021.

Plant, W. J. A relationship between wind stress and wave slope. *Journal of Geophysical Research*, 87(C3), 1982. ISSN 0148-0227. doi: 10.1029/JC087iC03p01961.

PopStefanija, I., Fairall, C. W., and Walsh, E. J. Mapping of Directional Ocean Wave Spectra in Hurricanes and Other Environments. *IEEE Transactions on Geoscience and Remote Sensing*, 59 (11):9007–9020, November 2021. ISSN 0196-2892, 1558-0644. doi: 10.1109/TGRS.2020.3042904.

Porchetta, S., Temel, O., Muñoz-Esparza, D., Reuder, J., Monbaliu, J., Van Beeck, J., and Van Lipzig, N. A new roughness length parameterization accounting for wind–wave (mis)alignment.

Atmospheric Chemistry and Physics, 19(10):6681–6700, May 2019. ISSN 1680-7324. doi: 10.5194/acp-19-6681-2019.

Potter, H., Collins, C. O., and Ortiz-Suslow, D. G. Pier-Based Measurements of Air-Sea Momentum Fluxes Over Shoaling Waves During DUNEX. *Journal of Geophysical Research: Oceans*, 127(11), November 2022. ISSN 2169-9275, 2169-9291. doi: 10.1029/2022JC018801.

Powell, M. D., Vickery, P. J., and Reinhold, T. A. Reduced drag coefficient for high wind speeds in tropical cyclones. *Nature*, 422(6929):279–283, March 2003. ISSN 0028-0836, 1476-4687. doi: 10.1038/nature01481.

Quinn, P. K., Thompson, E., Coffman, D. J., Baidar, S., Bariteau, L., Bates, T. S., Bigorre, S., Brewer, A., De Boer, G., De Szoeke, S. P., Drushka, K., Foltz, G. R., Intrieri, J., Iyer, S., Fairall, C. W., Gaston, C. J., Jansen, F., Johnson, J. E., Krüger, O. O., Marchbanks, R. D., Moran, K. P., Noone, D., Pezoa, S., Pincus, R., Plueddemann, A. J., Pöhlker, M. L., Pöschl, U., Quinones Melendez, E., Royer, H. M., Szczodrak, M., Thomson, J., Upchurch, L. M., Zhang, C., Zhang, D., and Zuidema, P. Measurements from the RV Ronald H. Brown and related platforms as part of the Atlantic Tradewind Ocean-Atmosphere Mesoscale Interaction Campaign (ATOMIC). Technical report, 2020.

Raghukumar, K., Chang, G., Spada, F., Jones, C., Janssen, T., and Gans, A. Performance Characteristics of "Spotter," a Newly Developed Real-Time Wave Measurement Buoy. *Journal of Atmospheric and Oceanic Technology*, 36(6):1127–1141, June 2019. ISSN 0739-0572, 1520-0426. doi: 10.1175/JTECH-D-18-0151.1.

Reichl, B. G., Hara, T., and Ginis, I. Sea state dependence of the wind stress over the ocean under hurricane winds. *Journal of Geophysical Research: Oceans*, 119(1):30–51, 2014. ISSN 2169-9275, 2169-9291. doi: 10.1002/2013JC009289.

Richter, D. H., Bohac, R., and Stern, D. P. An Assessment of the Flux Profile Method for Determining Air–Sea Momentum and Enthalpy Fluxes from Dropsonde Data in Tropical Cyclones.

Journal of the Atmospheric Sciences, 73(7):2665–2682, July 2016. ISSN 0022-4928, 1520-0469. doi: 10.1175/JAS-D-15-0331.1.

Richter, D. H., Wainwright, C., Stern, D. P., Bryan, G. H., and Chavas, D. Potential low bias in high-wind drag coefficient inferred from dropsonde data in hurricanes. *Journal of the Atmospheric Sciences*, May 2021. ISSN 0022-4928, 1520-0469. doi: 10.1175/JAS-D-20-0390.1.

Roccapriore, K. M., Ziatdinov, M., Cho, S. H., Hachtel, J. A., and Kalinin, S. V. Predictability of Localized Plasmonic Responses in Nanoparticle Assemblies. *Small*, 17(21):2100181, 2021. doi: 10.1002/smll.202100181.

Romeiser, R., Graber, H. C., Caruso, M. J., Jensen, R. E., Walker, D. T., and Cox, A. T. A New Approach to Ocean Wave Parameter Estimates From C-Band ScanSAR Images. *IEEE Transactions on Geoscience and Remote Sensing*, 53(3):1320–1345, 2015. ISSN 0196-2892, 1558-0644. doi: 10.1109/TGRS.2014.2337663.

Romero, L. and Lubana, K. On the Bimodality of the Wind-Wave Spectrum: Mean-Squared-Slopes and Azimuthal Overlap Integral. *Journal of Physical Oceanography*, April 2022. ISSN 0022-3670, 1520-0485. doi: 10.1175/JPO-D-21-0299.1.

Romero, L. and Melville, W. K. Airborne Observations of Fetch-Limited Waves in the Gulf of Tehuantepec. *Journal of Physical Oceanography*, 40(3):441–465, March 2010. ISSN 1520-0485, 0022-3670. doi: 10.1175/2009JPO4127.1.

Romero, L., Melville, W. K., and Kleiss, J. M. Spectral Energy Dissipation due to Surface Wave Breaking. *Journal of Physical Oceanography*, 42(9):1421–1444, September 2012. ISSN 0022-3670, 1520-0485. doi: 10.1175/JPO-D-11-072.1.

Ross, V. and Dion, D. Sea surface slope statistics derived from Sun glint radiance measurements and their apparent dependence on sensor elevation. *Journal of Geophysical Research*, 112(C9): C09015, September 2007. ISSN 0148-0227. doi: 10.1029/2007JC004137.

Samelson, R. M. Wind Drift in a Homogeneous Equilibrium Sea. *Journal of Physical Oceanography*, 52(9):1945–1967, September 2022. ISSN 0022-3670, 1520-0485. doi: 10.1175/JPO-D-22-0017.1.

Sapp, J., Alsweiss, S., Jelenak, Z., Chang, P., and Carswell, J. Stepped Frequency Microwave Radiometer Wind-Speed Retrieval Improvements. *Remote Sensing*, 11(3):214, January 2019. ISSN 2072-4292. doi: 10.3390/rs11030214.

Sapp, J., Jelenak, Z., Chang, P., Carswell, J. R., Pollard, B., and Theg, A. Near-Real-Time Significant Wave Heights in Hurricanes from a New Airborne KA-Band Interferometric Altimeter. In *2021 IEEE International Geoscience and Remote Sensing Symposium IGARSS*, pages 7426–7429, Brussels, Belgium, July 2021. IEEE. ISBN 978-1-66540-369-6. doi: 10.1109/IGARSS47720.2021.9554385.

Sauvage, C., Seo, H., Barr, B. W., Edson, J. B., and Clayson, C. A. Misaligned Wind-Waves Behind Atmospheric Cold Fronts. *Journal of Geophysical Research: Oceans*, 129(9):e2024JC021162, September 2024. ISSN 2169-9275, 2169-9291. doi: 10.1029/2024JC021162.

Schwendeman, M., Thomson, J., and Gemmrich, J. R. Wave Breaking Dissipation in a Young Wind Sea. *Journal of Physical Oceanography*, 44(1):104–127, January 2014. ISSN 0022-3670, 1520-0485. doi: 10.1175/JPO-D-12-0237.1.

Schwendeman, M. and Thomson, J. Sharp-crested breaking surface waves observed from a ship-based stereo video system. *Journal of Physical Oceanography*, 47(4):775–792, 2017. doi: 10.1175/JPO-D-16-0187.1.

Schönau, M. C., Paluszkiewicz, T., Centurioni, L. R., Komaromi, W. A., Jin, H., and Doyle, J. D. In Situ Observations at the Air-Sea Interface by Expendable Air-Deployed Drifters Under Hurricane Michael (2018). *Geophysical Research Letters*, 51(5):e2023GL105730, March 2024. ISSN 0094-8276, 1944-8007. doi: 10.1029/2023GL105730.

Shaw, J. A. and Churnside, J. H. Scanning-laser glint measurements of sea-surface slope statistics. *Appl. Opt.*, 36(18):4202–4213, June 1997. doi: 10.1364/AO.36.004202.

Shimura, T., Mori, N., Baba, Y., and Miyashita, T. Ocean Surface Wind Estimation From Waves Based on Small GPS Buoy Observations in a Bay and the Open Ocean. *Journal of Geophysical Research: Oceans*, 127(9):e2022JC018786, September 2022. ISSN 2169-9275, 2169-9291. doi: 10.1029/2022JC018786.

Shimura, T., Mori, N., and Miyashita, T. Footprint of the air-sea momentum transfer saturation observed by ocean wave buoy network in extreme tropical cyclones. *Coastal Engineering*, 191: 104537, August 2024. ISSN 03783839. doi: 10.1016/j.coastaleng.2024.104537.

Sidenko, E., Tertyshnikov, K., Lebedev, M., and Pevzner, R. Experimental study of temperature change effect on distributed acoustic sensing continuous measurements. *Geophysics*, 87(3): D111–D122, 2022. doi: 10.1190/geo2021-0524.1.

Smith, M. M., Thomson, J., Baker, M. G., Abbott, R. E., and Davis, J. Observations of Ocean Surface Wave Attenuation in Sea Ice Using Seafloor Cables. *Geophysical Research Letters*, 2023. doi: 10.1029/2023GL105243.

Smith, R. K. and Montgomery, M. T. On the existence of the logarithmic surface layer in the inner core of hurricanes. *Quarterly Journal of the Royal Meteorological Society*, 140(678):72–81, January 2014. ISSN 0035-9009, 1477-870X. doi: 10.1002/qj.2121.

Stanciu, A., Frederick, J., Baker, M., Abbott, R., Conley, E., Solomon, E., and Jones, K. Using Distributed Acoustic and Temperature Sensing to Characterize the Rapidly Changing Nearshore Arctic Ocean (PEMDATS), April 2023.

Stockdon, H. F., Sallenger, A. H., Holman, R. A., and Howd, P. A. A simple model for the spatially-variable coastal response to hurricanes. *Marine Geology*, 238(1-4):1–20, 2007. ISSN 00253227. doi: 10.1016/j.margeo.2006.11.004.

Sullivan, P. P., Banner, M. L., Morison, R. P., and Peirson, W. L. Turbulent Flow over Steep Steady and Unsteady Waves under Strong Wind Forcing. *Journal of Physical Oceanography*, 48(1): 3–27, January 2018. ISSN 0022-3670, 1520-0485. doi: 10.1175/JPO-D-17-0118.1.

Sun, J., Vandemark, D., Mahrt, L., Vickers, D., Crawford, T., and Vogel, C. Momentum transfer over the coastal zone. *Journal of Geophysical Research: Atmospheres*, 106(D12):12437–12448, June 2001. ISSN 0148-0227. doi: 10.1029/2000JD900696.

Sun, R., Villas Bôas, A. B., Subramanian, A. C., Cornuelle, B. D., Mazloff, M. R., Miller, A. J., Langodan, S., and Hoteit, I. Focusing and defocusing of tropical cyclone generated waves by ocean current refraction. *Journal of Geophysical Research: Oceans*, 127, 2022. doi: 10.1029/2021JC018112.

Sutherland, G. and Rabault, J. Observations of wave dispersion and attenuation in landfast ice. *Journal of Geophysical Research: Oceans*, 121(3):1984–1997, 2016. ISSN 2169-9275, 2169-9291. doi: 10.1002/2015JC011446.

Sutherland, P., Brozena, J., Rogers, W. E., Doble, M., and Wadhams, P. Airborne Remote Sensing of Wave Propagation in the Marginal Ice Zone. *Journal of Geophysical Research: Oceans*, 123 (6):4132–4152, 2018. ISSN 2169-9275, 2169-9291. doi: 10.1029/2018JC013785.

Takagaki, N., Komori, S., Suzuki, N., Iwano, K., Kuramoto, T., Shimada, S., Kurose, R., and Takahashi, K. Strong correlation between the drag coefficient and the shape of the wind sea spectrum over a broad range of wind speeds. *Geophysical Research Letters*, 39(23), December 2012. ISSN 00948276. doi: 10.1029/2012GL053988.

Takagaki, N., Komori, S., Suzuki, N., Iwano, K., and Kurose, R. Mechanism of drag coefficient saturation at strong wind speeds. *Geophysical Research Letters*, 2016. ISSN 1944-8007. doi: 10.1002/2016GL070666.

Tamizi, A. and Young, I. R. The Spatial Distribution of Ocean Waves in Tropical Cyclones. *Journal of Physical Oceanography*, 50(8):2123–2139, 2020. doi: 10.1175/JPO-D-20-0020.1.

Tannehill, I. R. Sea swells in relation to movement and intensity of tropical storms. *Monthly Weather Review*, 64(7):231–238, 1936. ISSN 0027-0644, 1520-0493. doi: 10.1175/1520-0493(1936)64<231b:SSIRTM>2.0.CO;2.

Taylor, P. K. and Yelland, M. J. The Dependence of Sea Surface Roughness on the Height and Steepness of the Waves. *Journal of Physical Oceanography*, 31(2):572–590, February 2001. ISSN 0022-3670, 1520-0485. doi: 10.1175/1520-0485(2001)031<0572:TDOSSR>2.0.CO;2.

Thompson, D., Elfouhaily, T., and Garrison, J. An improved geometrical optics model for bistatic GPS scattering from the ocean surface. *IEEE Transactions on Geoscience and Remote Sensing*, 43(12):2810–2821, December 2005. ISSN 0196-2892. doi: 10.1109/TGRS.2005.857895.

Thomson, J., D'Asaro, E. A., Cronin, M. F., Rogers, W. E., Harcourt, R. R., and Shcherbina, A. Waves and the equilibrium range at Ocean Weather Station P. *Journal of Geophysical Research: Oceans*, 118(11):5951–5962, November 2013. ISSN 21699275. doi: 10.1002/2013JC008837.

Thomson, J. Wave Breaking Dissipation Observed with "SWIFT" Drifters. *Journal of Atmospheric and Oceanic Technology*, 29(12):1866–1882, December 2012. ISSN 0739-0572, 1520-0426. doi: 10.1175/JTECH-D-12-00018.1.

Thomson, J. and Rogers, W. E. Swell and sea in the emerging Arctic Ocean. *Geophysical Research Letters*, 41(9):3136–3140, May 2014. ISSN 0094-8276, 1944-8007. doi: 10.1002/2014GL059983.

Thomson, J. and Smith, M. Moorings along the seafloor cable route extending offshore from Oliktok Point, Alaska, from April to September of 2023, 2024.

Thomson, J., Talbert, J., de Klerk, A., Brown, A., Schwendeman, M., Goldsmith, J., Thomas, J., Olfe, C., Cameron, G., and Meinig, C. Biofouling effects on the response of a wave measurement buoy in deep water. *Journal of Atmospheric and Oceanic Technology*, 32(6):1281–1286, 2015. doi: 10.1175/JTECH-D-15-0029.1.

Thomson, J., Girton, J. B., Jha, R., and Trapani, A. Measurements of Directional Wave Spectra and Wind Stress from a Wave Glider Autonomous Surface Vehicle. *Journal of Atmospheric and Oceanic Technology*, 35:17, 2018.

Thomson, J., Bush, P., Castillo Contreras, V., Clemett, N., Davis, J., De Klerk, A., Iseley, E., Rainville, E. J., Salmi, B., and Talbert, J. Development and testing of microSWIFT expendable wave buoys. *Coastal Engineering Journal*, pages 1–13, 2023. ISSN 2166-4250, 1793-6292. doi: 10.1080/21664250.2023.2283325.

Thyng, K., Greene, C., Hetland, R., Zimmerle, H., and DiMarco, S. True Colors of Oceanography: Guidelines for Effective and Accurate Colormap Selection. *Oceanography*, 29(3), September 2016. ISSN 10428275. doi: 10.5670/oceanog.2016.66.

Ticona Rollano, F., Brown, A., Ellenson, A., Özkan Haller, H. T., Thomson, J., and Haller, M. C. Breaking waves in deep water: measurements and modeling of energy dissipation. *Ocean Dynamics*, 69(10):1165–1179, October 2019. ISSN 1616-7341, 1616-7228. doi: 10.1007/s10236-019-01301-2.

Toba, Y. Local balance in the air-sea boundary processes. *Journal of the Oceanographical Society of Japan*, 29:209–220, 1973.

Toba, Y., Iida, N., Kawamura, H., Ebuchi, N., and Jones, I. S. F. Wave Dependence of Sea-Surface Wind Stress. *Journal of Physical Oceanography*, 20(5):705 – 721, 1990. doi: 10.1175/1520-0485(1990)020<0705:WDOSSW>2.0.CO;2.

Troitskaya, Y., Sergeev, D. A., Kandaurov, A. A., Baidakov, G. A., Vdovin, M. A., and Kazakov, V. I. Laboratory and theoretical modeling of air-sea momentum transfer under severe wind conditions. *Journal of Geophysical Research: Oceans*, 117(C11), November 2012. ISSN 01480227. doi: 10.1029/2011JC007778.

Troitskaya, Y., Sergeev, D., Kandaurov, A., Vdovin, M., and Zilitinkevich, S. The effect of foam on waves and the aerodynamic roughness of the water surface at high winds. *Journal of Physical Oceanography*, 49(4):959–981, 2019. doi: 10.1175/JPO-D-18-0168.1.

Troitskaya, Y., Ezhova, E., Soustova, I., and Zilitinkevich, S. On the effect of sea spray on the aerodynamic surface drag under severe winds. *Ocean Dynamics*, 66(5):659–669, 2016. ISSN 1616-7228. doi: 10.1007/s10236-016-0948-9.

Vandemark, D., Chapron, B., Sun, J., Crescenti, G. H., and Graber, H. C. Ocean Wave Slope Observations Using Radar Backscatter and Laser Altimeters. *Journal of Physical Oceanography*, 34(12):2825–2842, December 2004. ISSN 1520-0485, 0022-3670. doi: 10.1175/JPO2663.1.

Vincent, C. L., Thomson, J., Graber, H. C., and Collins, C. O. Impact of swell on the wind-sea and resulting modulation of stress. *Progress in Oceanography*, 178, November 2019. ISSN 00796611. doi: 10.1016/j.pocean.2019.102164.

Voermans, J. J., Smit, P. B., Janssen, T. T., and Babanin, A. V. Estimating wind speed and direction using wave spectra. *Journal of Geophysical Research: Oceans*, 125(2), 2020. doi: 10.1029/2019JC 015717.

Walsh, E. J., Wright, C. W., Vandemark, D., Krabill, W. B., Garcia, A. W., Houston, S. H., Murillo, S. T., Powell, M. D., Black, P. G., and Marks, F. D. Hurricane directional wave spectrum spatial variation at landfall. *Journal of Physical Oceanography*, 32(6):1667–1684, 2002. doi: 10.1175/15 20-0485(2002)032<1667:HDWSSV>2.0.CO;2.

Walsh, E. J., Vandemark, D. C., Friehe, C. A., Burns, S. P., Khelif, D., Swift, R. N., and Scott, J. F. Measuring sea surface mean square slope with a 36-GHz scanning radar altimeter. *Journal of Geophysical Research: Oceans*, 103(C6):12587–12601, June 1998. ISSN 0148-0227. doi: 10.1029/ 97JC02443.

Walsh, E. J., PopStefanija, I., Matrosov, S. Y., Zhang, J., Uhlhorn, E., and Klotz, B. Airborne Rain-Rate Measurement with a Wide-Swath Radar Altimeter. *Journal of Atmospheric and Oceanic*

Technology, 31(4):860–875, April 2014. ISSN 0739-0572, 1520-0426. doi: 10.1175/JTECH-D-13-00111.1.

Walsh, E. J., Fairall, C. W., and PopStefanija, I. In the eye of the storm. *Journal of Physical Oceanography*, 2021. doi: 10.1175/JPO-D-20-0219.1.

Wamriew, D., Pevzner, R., Maltsev, E., and Pissarenko, D. Deep Neural Networks for Detection and Location of Microseismic Events and Velocity Model Inversion from Microseismic Data Acquired by Distributed Acoustic Sensing Array. *Sensors*, 21(19):6627, October 2021. ISSN 1424-8220. doi: 10.3390/s21196627.

Wentz, F. J. A Two-Scale Scattering Model With Application to the JONSWAP '75 Aircraft Microwave Scatterometer Experiment. NASA Contractor Report, 1977.

Whalen, J. and Ochi, M. Variability Of Wave Spectral Shapes Associated With Hurricanes. In *OTC Offshore Technology Conference*, 1978.

Williams, E. F., Fernández-Ruiz, M. R., Magalhaes, R., Vanthillo, R., Zhan, Z., González-Herráez, M., and Martins, H. F. Distributed sensing of microseisms and teleseisms with submarine dark fibers. *Nature Communications*, 10(1):5778, December 2019. ISSN 2041-1723. doi: 10.1038/s41467-019-13262-7.

Williams, E. F., Zhan, Z., Martins, H. F., Fernández-Ruiz, M. R., Martín-López, S., González-Herráez, M., and Callies, J. Surface Gravity Wave Interferometry and Ocean Current Monitoring With Ocean-Bottom DAS. *Journal of Geophysical Research: Oceans*, 127(5):e2021JC018375, May 2022. ISSN 2169-9275, 2169-9291. doi: 10.1029/2021JC018375.

Wright, C. W., Walsh, E. J., Vandemark, D., Krabill, W. B., Garcia, A. W., Houston, S. H., Powell, M. D., Black, P. G., and Marks, F. D. Hurricane Directional Wave Spectrum Spatial Variation in the Open Ocean. *Journal of Physical Oceanography*, 31(8):2472–2488, 2001. ISSN 0022-3670, 1520-0485. doi: 10.1175/1520-0485(2001)031<2472:HDWSSV>2.0.CO;2.

Wright, E. E., Bourassa, M. A., Stoffelen, A., and Bidlot, J.-R. Characterizing Buoy Wind Speed Error in High Winds and Varying Sea State with ASCAT and ERA5. *Remote Sensing*, 13(22): 4558, November 2021. ISSN 2072-4292. doi: 10.3390/rs13224558.

Wu, J. Mean square slopes of the wind-disturbed water surface, their magnitude, directionality, and composition. *Radio Science*, 25(1):37–48, 1990. ISSN 0048-6604, 1944-799X. doi: 10.1029/RS025i001p00037.

Xenaki, A., Gerstoft, P., Williams, E., and Abadi, S. Distributed acoustic sensing for ocean applications, February 2025.

Xiao, H., Spica, Z. J., Li, J., and Zhan, Z. Detection of Earthquake Infragravity and Tsunami Waves With Underwater Distributed Acoustic Sensing. *Geophysical Research Letters*, 51(2): e2023GL106767, January 2024. ISSN 0094-8276, 1944-8007. doi: 10.1029/2023GL106767.

Young, I. R. A review of the sea state generated by hurricanes. *Marine Structures*, 16(3):201–218, May 2003. ISSN 09518339. doi: 10.1016/S0951-8339(02)00054-0.

Young, I. R. Directional spectra of hurricane wind waves. *Journal of Geophysical Research: Oceans*, 111, 2006. ISSN 2156-2202. doi: 10.1029/2006JC003540.

Yu, Y., Stern, H., Fowler, C., Fetterer, F., and Maslanik, J. Interannual Variability of Arctic Landfast Ice between 1976 and 2007. *Journal of Climate*, 27(1):227–243, January 2014. ISSN 0894-8755, 1520-0442. doi: 10.1175/JCLI-D-13-00178.1.

Yujuan, S., William, P., and Bechara, T. Simulation of wave-current interactions under hurricane conditions using an unstructured-grid model: Impacts on ocean waves. *Journal of Geophysical Research: Oceans*, 2018. doi: 10.1029/2017JC012939.

Zappa, C. J., Banner, M. L., Schultz, H., Corrada-Emmanuel, A., Wolff, L. B., and Yalcin, J. Retrieval of short ocean wave slope using polarimetric imaging. *Measurement Science and Technology*, 19(5), May 2008. ISSN 0957-0233, 1361-6501. doi: 10.1088/0957-0233/19/5/055503.

Zhong, Y.-Z., Chien, H., Chang, H.-M., and Cheng, H.-Y. Ocean Wind Observation Based on the Mean Square Slope Using a Self-Developed Miniature Wave Buoy. *Sensors*, 22(19):7210, September 2022. ISSN 1424-8220. doi: 10.3390/s22197210.

Zhou, X., Hara, T., Ginis, I., D'Asaro, E., Hsu, J.-Y., and Reichl, B. G. Drag coefficient and its sea state dependence under tropical cyclones. *Journal of Physical Oceanography*, May 2022. ISSN 0022-3670, 1520-0485. doi: 10.1175/JPO-D-21-0246.1.

Zippel, S. and Thomson, J. Surface wave breaking over sheared currents: Observations from the Mouth of the Columbia River. *Journal of Geophysical Research: Oceans*, 122(4):3311–3328, 2017. ISSN 2169-9275, 2169-9291. doi: 10.1002/2016JC012498.